Structures Research
Report 2010/83710

University of Florida
Civil and Coastal Engineering

UF

GATOR Engineering

University of Florida
Civil and Coastal Engineering

Final Report April 2010

Development and Support of Dynamic Numerical Modeling of Aberrant Rake Barges Impacting Hurricane Protection Structures Subjected to Forces from a Hurricane Environment

Principal investigator:
Gary R. Consolazio, Ph.D.

Doctoral research assistants:
Michael T. Davidson
Daniel J. Getter

Department of Civil and Coastal Engineering
University of Florida
P.O. Box 116580
Gainesville, Florida 32611

Sponsor:
Digital Engineering and Imaging, Inc.
U.S. Department of the Army
Point of Contact:
Robert C. Patev, Senior Risk Advisor, Risk Management Center, US Army Corps of Engineers

Contract:
UF Project No. 83710
Digital Engineering and Imaging, Inc. No. 674-01-0198-13
U.S. Dept. of the Army No. W912P8-07-D-0054

DISCLAIMER

The opinions, findings, and conclusions expressed in this publication are those of the authors and not necessarily those of the U.S. Army Corps of Engineers or Digital Engineering and Imaging, Inc.

ACKNOWLEDGEMENTS

The authors would like to thank the U.S. Army Corps of Engineers and Digital Engineering and Imaging, Inc. for providing the funding that made this research possible. The authors would specifically like to extend thanks to Mr. Robert Patev (U.S. Army Corp of Engineers), Dr. Patrick Hudson (Moment Engineering) and Dr. Michael McCormick (U.S. Naval Academy) for their critical contributions to the overall effort of which this work is only a part. The authors also thank Mr. Zachary Harper, Mr. Falak Shah, and Mr. Robert Hendrix for their invaluable support of modeling, data processing, and report production activities.

EXECUTIVE SUMMARY

During hurricane events, moored barges are at risk of being propelled by high winds and impacting flood protection walls in the vicinity. Cities like New Orleans, Louisiana are at particular risk for such hazards, due to the preponderance of canals and moored barges throughout the city combined with high hurricane risk. Unfortunately, limited information is available to estimate the magnitude of barge impact loads for the design of floodwalls. In this report, forces associated with hurricane wind-propelled barge impact on floodwalls are quantified using high-resolution dynamic finite element simulations. Such simulations account for highly nonlinear material deformation in the impacting barge, nonlinear soil deformation, and dynamic interaction between the barge, wall, and soil system. The representative presents force histories for a variety of representative impact scenarios which can be used directly in dynamic analysis of floodwalls. Additional guidance is provided for employing the force results in static design scenarios.

TABLE OF CONTENTS

LIST OF FIGURES

LIST OF TABLES

Table Page

CHAPTER 1
INTRODUCTION AND BACKGROUND

1.1 Introduction

The city of New Orleans, Louisiana, USA is located near the mouth of the Mississippi River on the coast of the Gulf of Mexico, and large portions of the city have been constructed at or below sea level. Consequently, New Orleans is at risk to significant water intrusions resulting from both seasonal river flooding and hurricane-induced storm surges. Thus, the city and many surrounding areas are protected with an extensive system of earthen levees and concrete floodwalls that are designed and maintained by the U.S. Army Corps of Engineers (USACE). During hurricanes, these floodwalls are subjected to loads from elevated storm surges, waves, wind, and wind-propelled debris. In fact, after Hurricane Katrina directly struck New Orleans in 2005, it was observed that numerous river barges, which had been moored throughout the city waterways, broke loose from their moorings and were propelled through the channels by hurricane winds. Thus, floodwalls throughout New Orleans—and any region where this scenario can occur—are at risk of being damaged by impact from aberrant, wind-propelled barges (Figure 1.1).

Figure 1.1 Aberrant barges that impacted New Orleans area floodwalls during Hurricane Katrina (Source: U.S. Army Corps of Engineers).

Due to the severe consequences associated with the barge impact hazard, the current study has been undertaken with the goal of quantifying barge impact loads on typical floodwalls using high-resolution dynamic finite element analysis. The study is focused on quantifying impact loads generated during collisions between barges and levee walls. Loads quantified by this study can be used to design new floodwalls and to assess the need for protecting or replacing existing infrastructure in flood-prone areas.

1.2 Background

Following a number of high-profile structural failures resulting from barge and ship collisions, significant research effort has been devoted to quantifying loads associated with barge impact with various waterway structures. For bridges, design codes in the U.S. (AASHTO 2009) and Europe (CEN 2007) prescribe barge impact loads and related design requirements. Ongoing research work is being carried out to further refine the U.S. code procedures by developing more

accurate predictions of impact loads (Yuan et al. 2008, Consolazio et al. 2009, Getter and Consolazio 2011) and improved analysis procedures (Conosolazio and Cowan 2005, Getter et al. 2011). However, these load prediction models and analysis procedures are not readily adapted to analyzing floodwalls subjected to wind-driven barge impact, primarily because the procedures were derived assuming that head-on impact will occur between the barge bow (front portion) and bridge pier. In contrast, during a hurricane, an unrestrained barge could impact floodwalls at any angle, permitting impact by the bow, stern (rear portion), or side of the barge.

Research focused on barge impact forces on other waterway structures has been conducted by the USACE. Specifically, studies were previously undertaken to quantify barge impact loads on rigid walls—such as those surrounding locks—including a series of full-scale barge flotilla impact experiments (Patev et al. 2003a, Patev et al. 2003b). This work ultimately culminated in design provisions and load prediction equations, referred to as ETL 1110-02-563 (USACE 2004), which pertain to collisions between barges and lock wall structures. However, impact loads predicted using the USACE ETL equations could be overly conservative when applied to barge impact with floodwalls, because floodwalls are much more flexible than the relatively rigid wall structures considered in the ETL provisions. Furthermore, like the bridge design procedures described above, impact from the barge stern or side is not considered in the ETL provisions. Given the limitations of applying existing analysis methods to the problem of hurricane wind-driven barge impact with floodwalls, the goal of this study is to quantify impact loads for a variety of feasible impact conditions using high-resolution finite element analysis.

1.3 Objective

The work described in this report focuses on quantifying barge impact loads on hurricane protection structures using high-resolution dynamic nonlinear finite element (FE) simulation techniques. These simulations provide valuable insight into the nature of barge collision loading on hurricane protection structures, as may be induced by a hurricane environment. Additionally, force-histories generated during the simulations can be used to quantify appropriate barge collision loads for use in the design of hurricane protection structures.

1.4 Scope

One type of barge and three types of hurricane protection structures are selected for simulation in this study. The barge modeled throughout this study is a jumbo hopper barge. Primary focus is given to simulating impacts involving empty barges (with minimal residual payload) striking various hurricane protection structures. Supplementary impact simulations are also carried out using a fully loaded barge. The three types of hurricane protection structures considered in this study include:

- HPO (USACE Hurricane Protection Office) wall located near St. Bernard Parish
- PRO (USACE Protection and Restoration Office) wall located near Algiers Canal
- PRO fronting protection (dolphin) system located near Hero Pumping Station

Quantifying barge impact loads on the wall and dolphin systems consists of carrying out the following tasks:

- Establish empty and loaded barge weights of interest and impact conditions (angles, speeds, drafts) of interest. Adapt jumbo hopper barge model to specific impact conditions of interest.

- Develop FE models of hurricane protection structures.

- Develop soil resistance models for each hurricane protection structure.

- Develop appropriate means of applying non-collision loads (e.g., buoyant forces, wave loads, gravity loads) to FE models.

- Using high-resolution dynamic nonlinear contact-impact FE simulations, quantify impact loads imparted to each type of protection structure for all conditions included in the baseline matrix of impact conditions.

- Filter the impact loads obtained from FE impact simulations and envelope the data in an appropriate manner (based on the dynamic characteristics of the protection structures).

CHAPTER 2
JUMBO HOPPER BARGE MODEL

2.1 Structural Configuration

Throughout this study, a jumbo hopper barge measuring 195 ft long and 35 ft wide is used for all impact simulations (Figure 2.1a). The barge is divided into three zones along the barge length: 27.5 ft bow, 162 ft hopper, and 5.5 ft stern (Figure 2.1b). Watertight bulkheads act to compartmentalize the barge and are spaced at 40.5 ft intervals throughout the hopper zone.

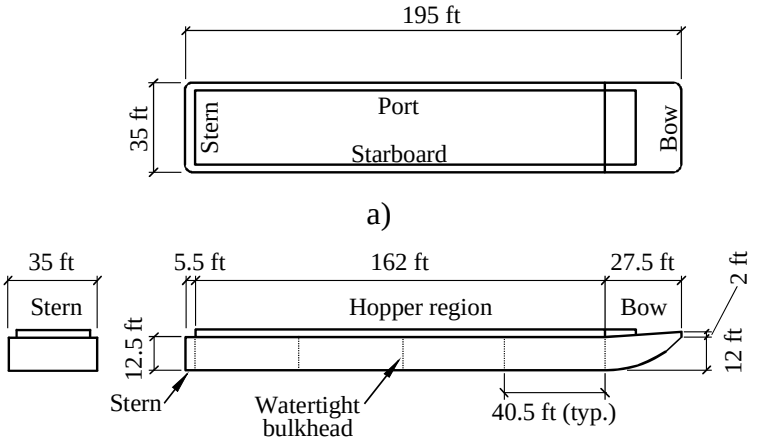

Figure 2.1 Jumbo hopper barge: a) Plan; b) Elevation

A high resolution mesh consisting of more than 900,000 nonlinear shell elements is used to model the barge in LS-DYNA (Figure 2.2). The barge structural configuration (as modeled) is consistent with available, detailed structural plans. For each of the three barge zones, external surfaces and internal structural members are discretely modeled (Figures 2.2 - 2.5). Throughout the three barge zones, internal and external plate thicknesses vary between 5/16 in. and 5/8 in. Internal stiffening members consist primarily of steel channel and single-angle members.

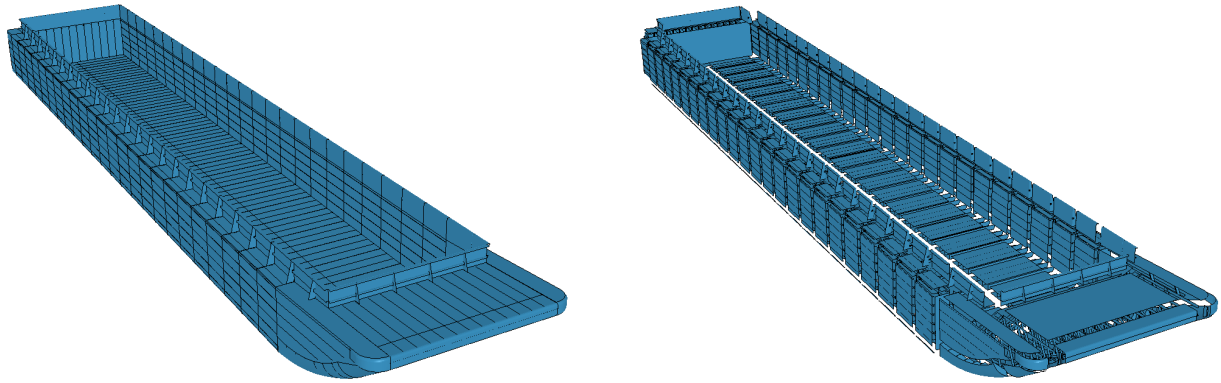

Figure 2.2 Jumbo hopper barge FE model (mesh not shown for clarity):
a) Perspective view; b) Exploded view

The barge bow zone is composed of fourteen internal rake trusses and frames; transverse stiffening members; and several external hull plates of varying thicknesses (Figure 2.3). The hopper zone consists of a barge bottom plate and hopper bottom plate that are connected by closely spaced transverse stiffener plates (Figure 2.4). Furthermore, the hopper zone contains 24 port and 24 starboard sidewall units (referred to as sidewall submodules). Each sidewall submodule is stiffened by closely (vertically) spaced longitudinal plates and angles. These longitudinal members terminate at watertight bulkheads that bound each group of six submodules. The short (in length) stern zone contains fourteen internal trusses and frames (Figure 2.5). Stiffening plates are closely spaced (vertically) at the port and starboard corners of the stern, where both transverse and longitudinal stiffening angles are attached to the corner stiffening plates.

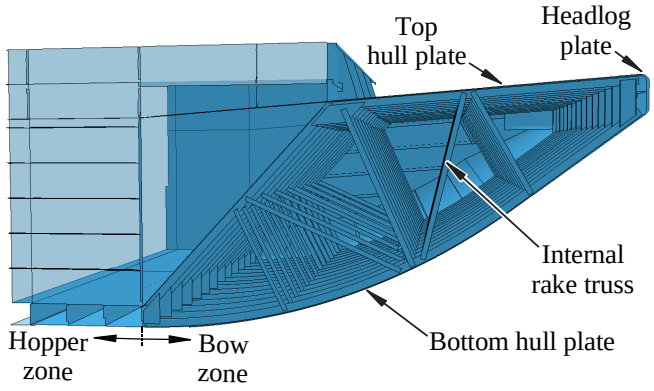

a)

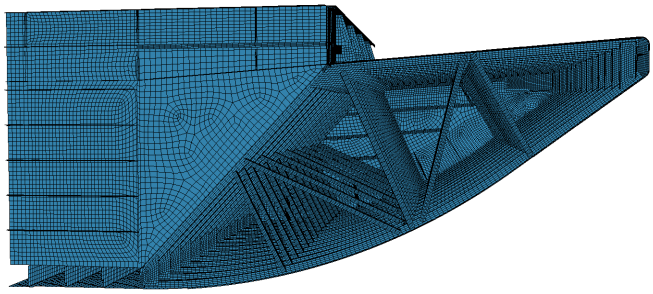

b)

Figure 2.3 Barge bow section: a) Structural configuration; b) FE mesh

Most barges fabricated in the U.S. are constructed from A36 structural steel. Hence, a nonlinear constitutive relationship (effective-true-stress vs. effective-plastic-strain) for A36 structural steel is employed for all shell elements in the barge model (Figure 2.6). The use of 4-node, fully integrated shell elements allows both plate and member buckling to occur as appropriate throughout the barge. Additionally, the use of shell elements to model internal structural members of the barge allows these components to undergo local material failure, which in LS-DYNA, results in element deletion. Angle and channel structural shapes are modeled with a sufficient number of elements so that reverse curvature can develop in the event of local member buckling (Figure 2.7). Steel components in barges are joined together by welds. In LS-DYNA, spotwelds are modeled by rigid beams that connect two nodes (from different

structural members) together. Weld failure is accounted for through element deletion upon failure of the joined shell elements (a shell element steel failure strain of 0.2 is enforced). Spotwelds are distributed at a sufficient density (e.g., those shown in Figure 2.7) to reasonably emulate welds present in the physical barge.

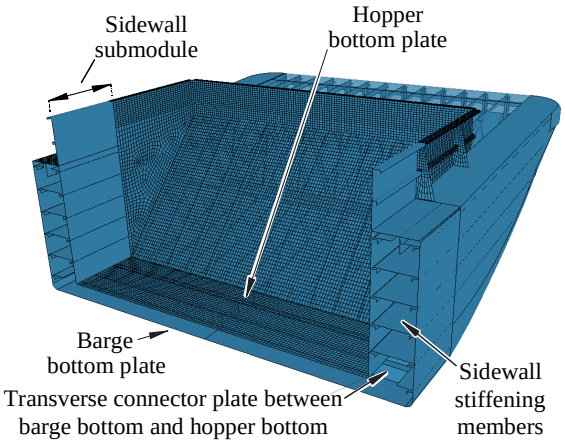

Figure 2.4 Barge bow-hopper zone interface (partial mesh shown for clarity)

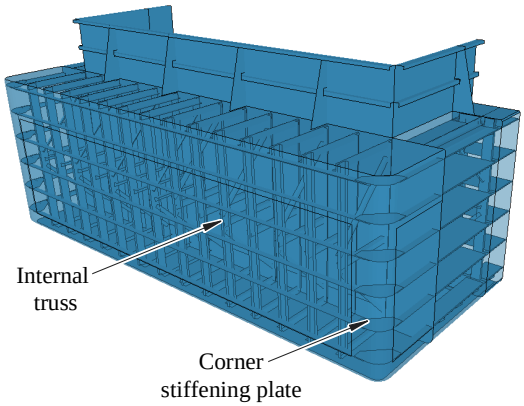

a)

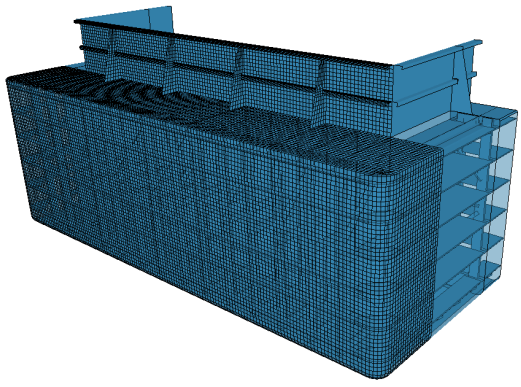

b)

Figure 2.5 Barge stern: a) Structural configuration; b) FE mesh (partial mesh shown for clarity)

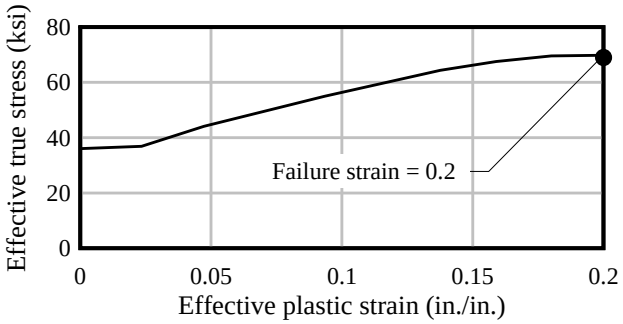

Figure 2.6 Barge structural steel material parameters

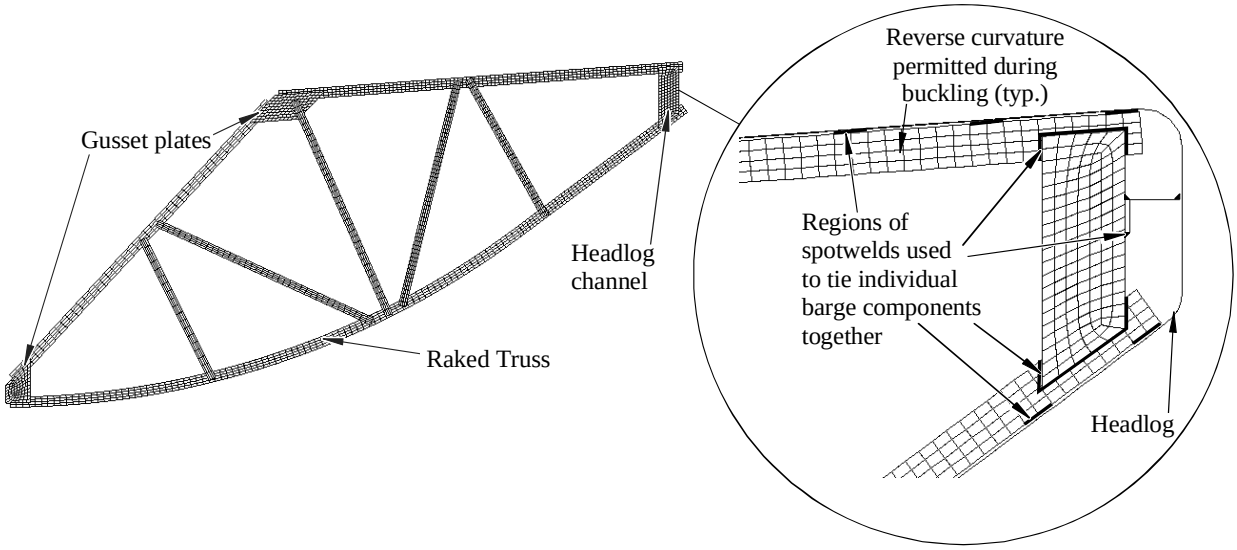

Figure 2.7 Barge internal member modeling (after Consolazio et al. 2009a)

2.2 Payload

The bare steel weight of the barge model is 285 tons (1 ton = 2000 lbs). However, once in service, "empty" barges commonly retain residual levels of transported material throughout the hopper zone. Hence, the following two barge weight conditions are used in this study:

- Empty barge: 362 tons (bare steel barge plus minimal residual payload)
- Loaded barge: 1645 tons (bare steel barge plus full payload)

Payload is modeled using a series of mass nodes that are distributed along the centerline of the hopper zone (Figure 2.8). Specifically, 27 payload mass nodes are placed at a height of $0.5h_{hop}$ (5.4 ft) above the hopper bottom plate (Figure 2.8a) and spaced uniformly at s_{cargo} (6 ft) intervals (Figure 2.8b). The total weights of the payload mass nodes are 77 tons and 1360 tons for the empty and loaded barge conditions, respectively.

A three-dimensional network of discrete springs acts to evenly transfer forces between payload mass nodes and the surrounding barge model (and between adjacent payload mass nodes). Additionally, a dashpot is modeled collinearly with each spring such that payload motion

is approximately critically damped. For each payload mass node, spring and dashpot elements are attached to the top, bottom, and mid-height of the barge sidewall. Furthermore, spring and dashpot elements span between each payload mass node and five locations across the hopper bottom plate (the attachment locations across the hopper bottom plate are spaced at $0.25w_{hop}$ = 7.13 ft). The barge and payload FE model is shown in Figure 2.9.

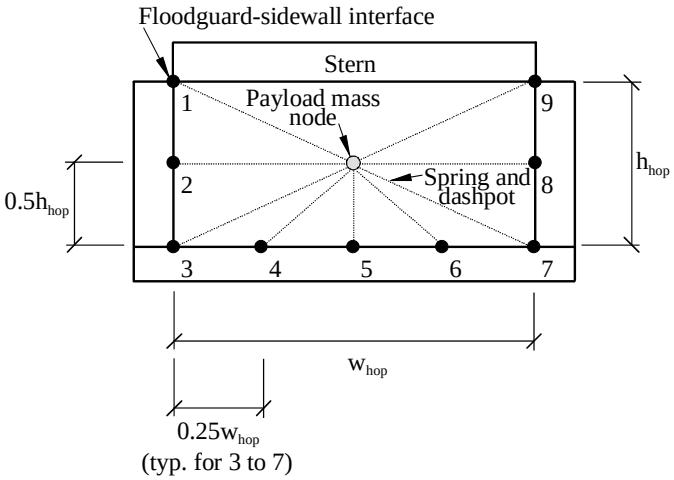

a)

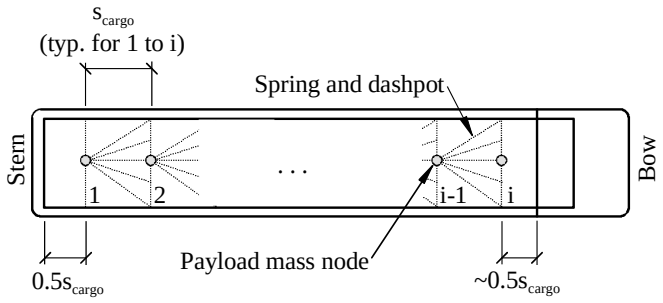

b)

Figure 2.8 Barge payload modeling schematic: a) Elevation view; b) Plan view

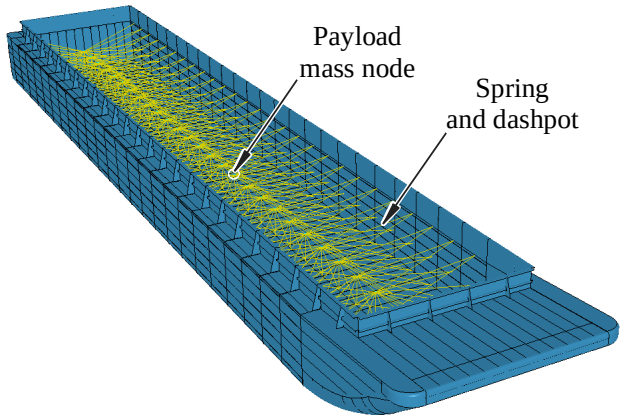

Figure 2.9 Barge and payload FE model

The barge weights, center of gravity (c.g.) locations, and corresponding mass moments of inertia for various weight conditions are given in Table 2.1. The $x_{c.g.}$, $y_{c.g}$, and $z_{c.g}$ coordinates are given in reference to the barge port side, rear of the barge stern, and bottom of the barge, respectively (Figure 2.10). Each moment of inertia value in Table 2.1 is given about the respective axis, where the axis passes through the c.g. of the barge.

Table 2.1 Barge mass-related quantities

	Bare steel	Empty	Loaded
Weight (ton)	285	362	1645
$x_{c.g.}$ (ft)	17.5	17.5	17.5
$y_{c.g.}$ (ft)	92.3	91	87.5
$z_{c.g.}$ (ft)	5.1	5.4	6.4
I_{xx}' (kip-in.-sec^2)	6.84E+05	8.11E+05	2.91E+06
I_{yy}' (kip-in.-sec^2)	4.06E+04	4.07E+04	4.10E+04
I_{zz}' (kip-in.-sec^2)	7.15E+05	8.42E+05	2.94E+06

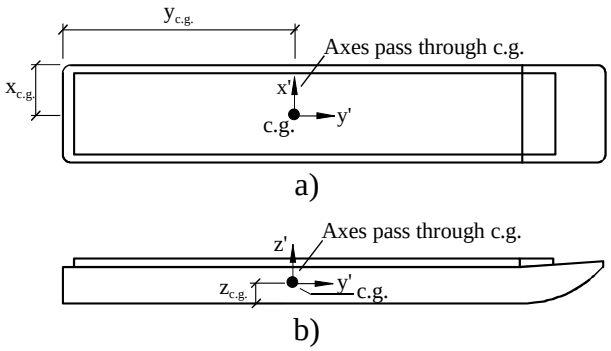

Figure 2.10 Orientation of barge mass-related quantities: a) Plan view; b) Elevation view

2.3 Buoyancy Effects

The buoyant effect of water surrounding the barge is accounted for through the incorporation of buoyancy springs connected to the barge bottom. Specifically, a set of more than 26,400 discrete springs are attached to barge bottom nodes throughout the bow, hopper, and stern zones (Figure 2.11). The springs additionally attach to nodes 1000 ft above the corresponding barge bottom nodes, where the spring top nodes are restrained from translation. Since the barge undergoes significant horizontal motion during the collision simulations, a large (1000 ft) vertical spring offset distance is necessary to maintain approximately vertical spring orientations (i.e., to maintain the integrity of the buoyancy spring forces generated).

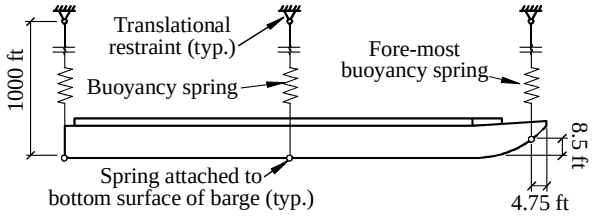

Figure 2.11 Barge buoyancy spring schematic

Regardless of the payload volume present, barge bottom portions in the hopper and stern zones that are fitted with buoyancy springs (a 34 ft wide by 167.5 ft long region, as shown in Figure 2.12a) remain submerged throughout the collision simulations. However, this is not the case for portions of the barge bottom in the bow zone (a 28.5 ft wide by 22.75 ft long region). Consequently, to ensure that nodal buoyancy forces are only generated during times in which the nodes are submerged, gaps are incorporated into the buoyancy spring force-deformation definitions for springs that attach to barge bottom nodes in the bow zone (Figure 2.12b). For a given buoyancy spring in the bow zone—with nodal height h_i relative to the barge bottom elevation—a gap of h_i is incorporated into the corresponding force-deformation relationship.

Buoyancy springs are defined as nonlinear elastic (tension-only) elements (Figure 2.12b). The stiffness of a given buoyancy spring, k_i, is determined by calculating the tributary area of barge supported by the spring and multiplying this value by the density of water. These stiffness values are small, ranging from 0.001 kip/in to 0.004 kip/in, and preclude unrealistically concentrated buoyant forces acting on the barge hull. Furthermore, the stiffness values vary in proportion to the (element mesh-based) surface area of barge supported by each spring.

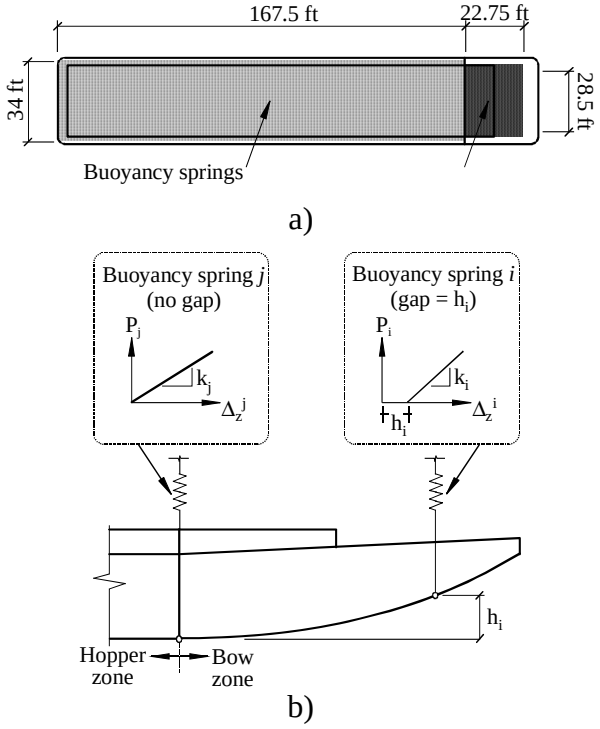

Figure 2.12 Barge buoyancy spring definitions:
a) Plan view of regions fitted with springs; b) Schematic

Gravitational forces are present in the barge FE model for all impact simulations conducted. In conjunction with the application of gravity loading, a buoyancy spring calibration scheme is employed to ensure that appropriate buoyant forces are generated (Figures 2.13 - 2.14). The use of buoyancy springs without calibration, in a gravity field, results in non-physical (unwarranted) dynamic oscillation.

The buoyancy spring calibration process for the empty barge weight condition is shown in Figure 2.13. First in this process, gravity loading $P_{body}(t)$ is applied to the empty barge FE model in a quasi-static manner (i.e., over a large time t_{ramp}, as shown in Figure 2.13b). The

quasi-statically applied gravity loads produce vertical steady-state displacements in the barge and buoyancy springs (Figure 2.13c). Note that, for an empty barge weighing 362 tons, a vertical steady-state displacement of 24.1 in. is reached at the c.g. of the barge. Subsequently, the steady-state displacement of each buoyancy spring (e.g., Δ_z^i for buoyancy spring *i*) is used to define, respectively, an initial offset in the same buoyancy spring. Then, for all collision simulations conducted, gravity is applied in an instantaneous and constant manner (Figure 2.13d). However, because the buoyancy springs now contain initial offsets corresponding to the steady-state displaced shape of the barge, the buoyancy spring forces and gravity loads are initialized in dynamic equilibrium. Hence, only nominal levels of artificial dynamic oscillation occur in the buoyancy springs during the collision simulations. Furthermore, by employing this calibration scheme, the profile of buoyancy spring forces throughout the barge length is consistent with the profile of forces supporting the barge in a steady-state displaced shape. An analogous calibration scheme is employed for the loaded barge weight condition (1645 tons), which reaches a vertical steady-state displacement of 102.1 in. at the barge c.g. (Figure 2.14).

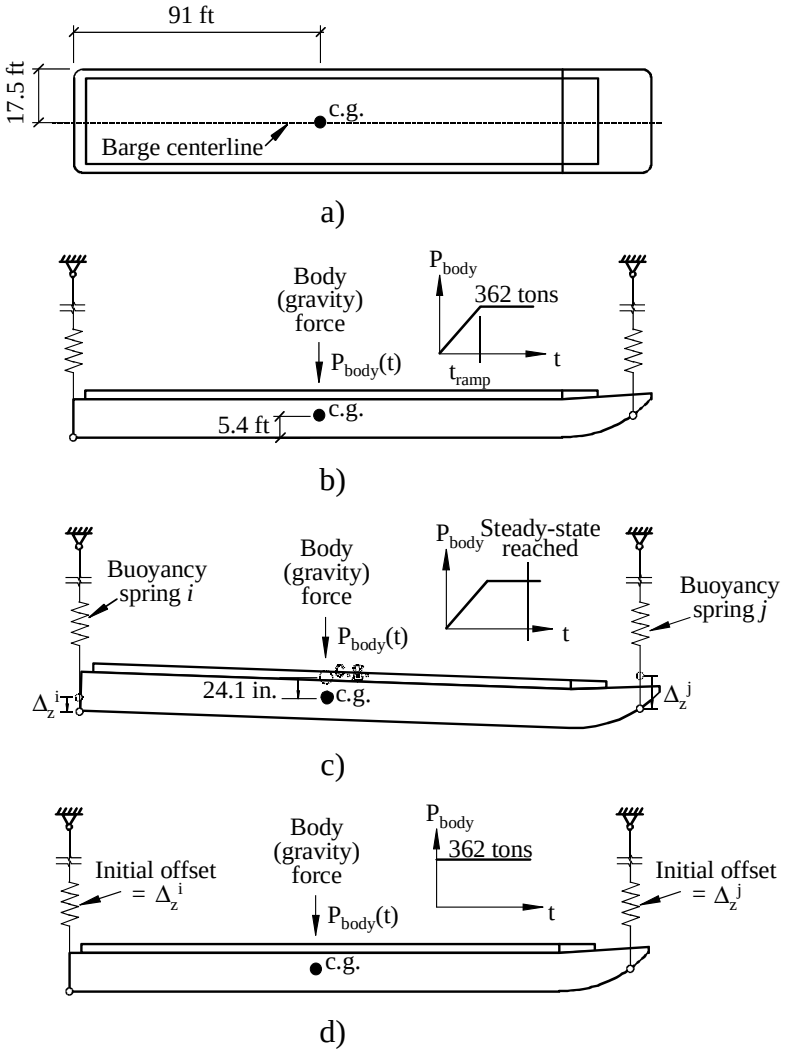

Figure 2.13 Empty barge buoyancy spring calibration: a) Location of c.g.; b) Quasi-static application of gravity loads; c) Steady-state displaced shape of barge; d) Calibrated schematic

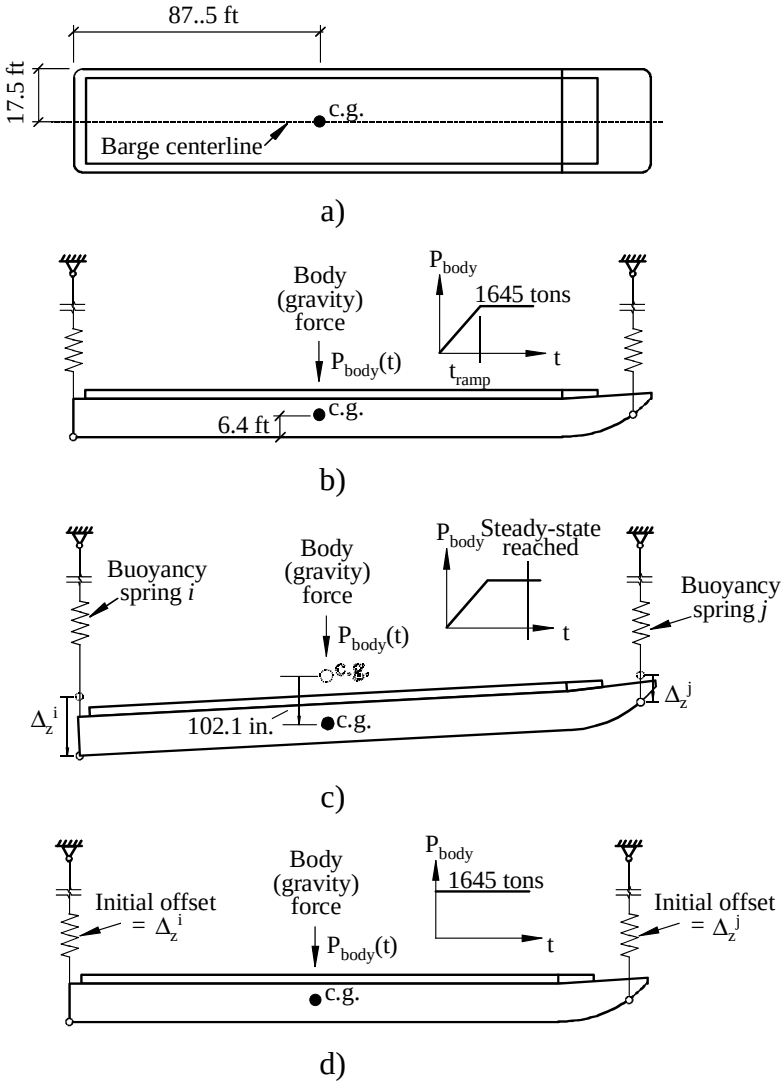

Figure 2.14 Loaded barge buoyancy spring calibration: a) Location of c.g.; b) Quasi-static application of gravity loads; c) Steady-state displaced shape of barge; d) Calibrated schematic

2.4 Efficient Barge Contact Definitions

For all collision simulations conducted in this study, barge collision forces are quantified using contact-impact algorithms in LS-DYNA (2009). Loads generated between the barge and a given hurricane protection structure are developed based on the interaction between any of a set of specified nodes on the barge model and any of a set of specified element faces (shell or solid) on the impacted structure. As an illustration of how the contact definition is implemented for a given case, consider the barge (nodal) contact definition shown in Figure 2.15. In this case, computational efficiency is achieved by only specifying those nodes on the barge that can potentially come into contact with the wall structure during collision. Contact forces that are generated possess both normal and transverse (frictional) components. The parameters for the

friction portion of the barge (steel) to wall (concrete) contact definition consist of 0.5 and 0.45 for static and dynamic coefficients of friction, respectively.

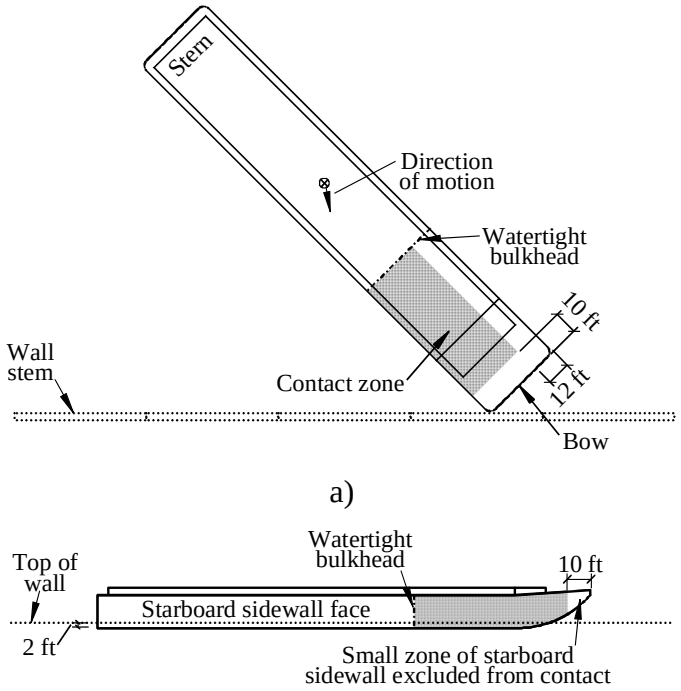

Figure 2.15 Empty barge, bow impact, large-angle, contact schematic:
a) Plan view; b) Elevation view

Additionally, in this study, an LS-DYNA algorithm is employed in all collision simulations such that self-contact of specified barge components is monitored. For steel-to-steel (self) contact, static and dynamic coefficients of friction are defined as 0.55 and 0.45, respectively. For the demonstration case shown in Figure 2.16, the self-contact zone is conservatively extended nearly 70 ft sternward from the barge bow to a watertight bulkhead (into which all longitudinal barge internal members terminate) to ensure that a sufficiently large self-contact zone is defined. Furthermore, for the demonstration case, portions of the barge—in which neither barge-to-structure contact nor self-contact are applicable—develop only nominal stresses due to collision. Consequently, those portions of the barge are rigidized as a means of substantially increasing computational efficiency (Figure 2.17). For all impact simulations conducted, analogous schemes (similar to those pertaining to the demonstration case) are used to efficiently incorporate barge-structure contact, barge self-contact, and barge rigidization into the barge FE model.

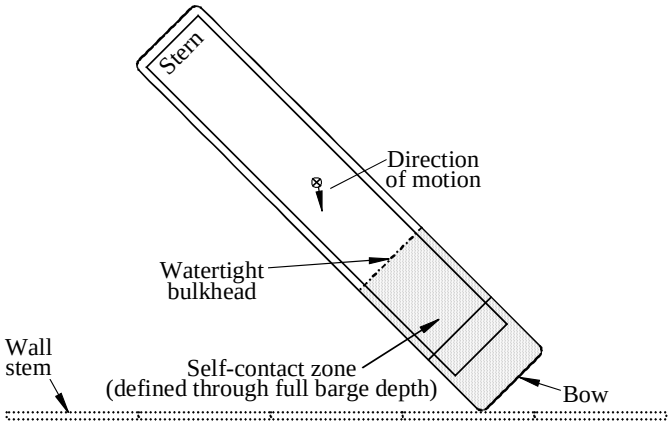

Figure 2.16 Empty barge, bow impact, large-angle, self-contact schematic (plan view)

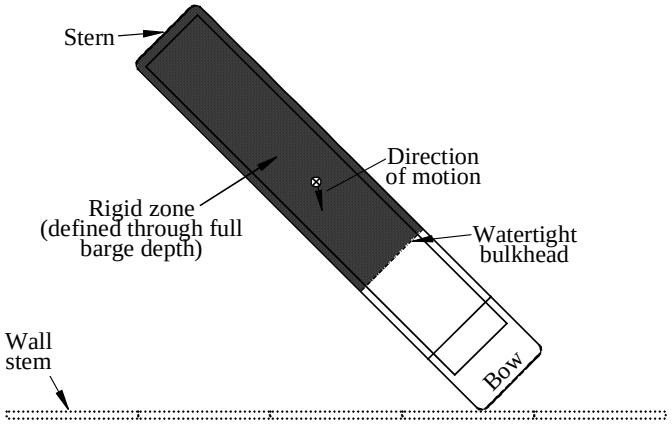

Figure 2.17 Empty barge, bow impact, large-angle, rigidization schematic (plan view)

CHAPTER 3
HURRICANE PROTECTION STRUCTURE MODELS

3.1 Overview

Three different hurricane protection structures are modeled in this study:

- HPO (USACE Hurricane Protection Office) wall located near St. Bernard Parish
- PRO (USACE Protection and Restoration Office) wall located near Algiers Canal
- PRO fronting protection (dolphin) system located near Hero Pumping Station

For each hurricane protection structure considered, details pertaining to structural resistance, soil resistance, and load modeling are given below. Each type of hurricane protection structure included in this study is modeled as several, adjacent structural units (e.g., multiple end-to-end monoliths, multiple side-by-side dolphins). However, structural resistance is identical for all structural units of a given structure type. Hence, the configuration for each structural FE model is detailed on a single-unit basis in Chapter 3 (details of multiple-unit model layouts are presented in Chapter 4).

3.2 Hurricane Protection Office (HPO) Wall Located Near St. Bernard Parish

3.2.1 Structural Configuration

Shown in Figures 3.1 - 3.2 are overall dimensions and features for a single HPO monolith—namely, the T-wall for Hydraulic Reach SB11, near St. Bernard Parish, Louisiana. Each monolith—consisting of a wall stem, footing, and piling—spans 50 ft and has a wall stem height of 11 ft. The reinforced concrete (R/C) footing and wall stem are supported on two rows of HP 14x73 piles (H-piles), where the pile row on the protected side of the wall is staggered. The H-piles are inclined at 1:2 (horizontal-to-vertical), contain a soil-embedment length greater than 90 ft (Figure 3.1), and are spaced along the monolith at 5.63 ft (Figure 3.2). Note that, in contrast to that of the H-piles, sheet piling is assumed to be provided primarily for seepage control (as opposed to structural resistance). Therefore, sheet piling is not included in the structural FE model.

Located at the ends of each monolith are non-structural, flexible waterstops (Figure 3.2). Consequently, each monolith is represented as a separate unit in the structural FE model, with no structural tie existing between individual monoliths. Linear elastic material models are employed for the HPO monolith R/C and steel material models (with elastic moduli of 3600 ksi and 29000 ksi, respectively).

A schematic diagram of the HPO monolith FE model—consisting of a wall stem, footing, H-piles, and soil—is shown in Figure 3.3. The corresponding FE model is shown in Figure 3.4. For most of the collision simulations conducted (see Section 4.2), the barge model initially contacts the top surface of the wall stem. Therefore, solid elements are used in this zone to provide a physically representative contact surface between the wall stem and barge. A 0.75 in. chamfer is included for the solid elements along the top of the wall stem. Shell elements—with physically representative structural thicknesses—are used to model the remainder of the wall stem and the footing. Nodal rigid bodies are used to structurally tie the top 2.58 ft of the wall stem (consisting of solid elements) to the underlying, tapered wall stem shell elements.

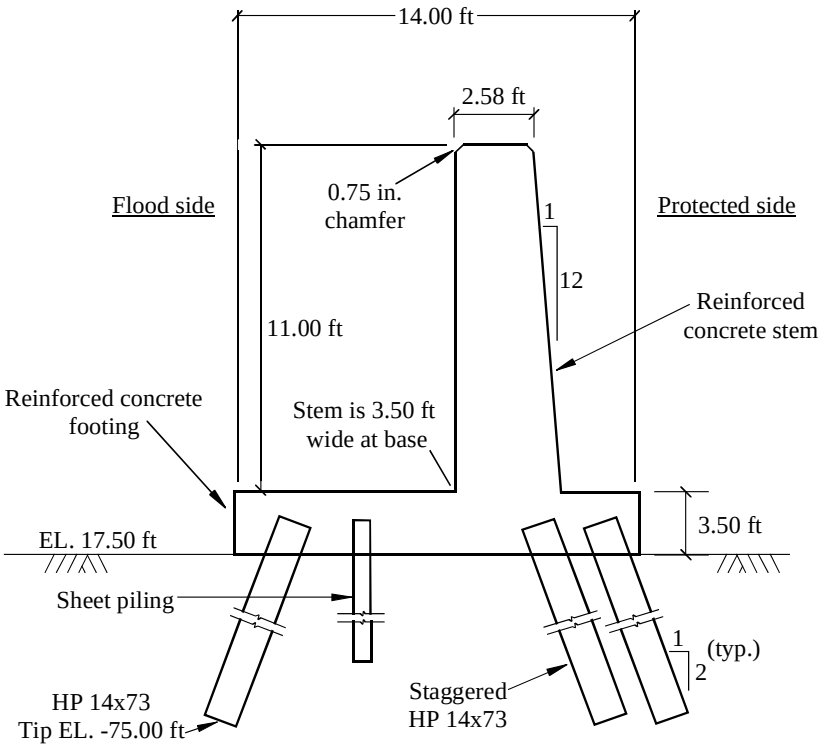

Figure 3.1 Cross-section of HPO monolith

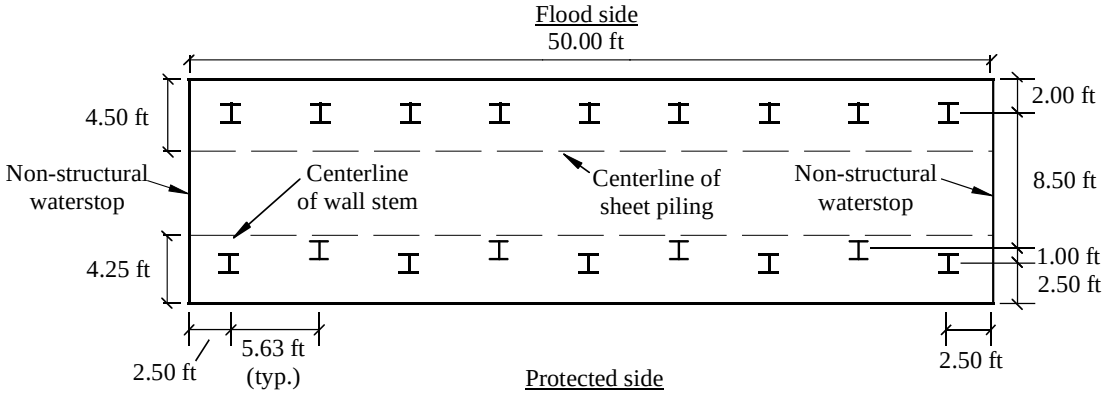

Figure 3.2 Plan view of HPO monolith

The HPO wall R/C footing is 3.5 ft thick, and hence, elements from the overlying wall stem and underlying H-piles that intersect the physical thickness of the footing are given special consideration (Figure 3.3). Specifically, portions of the wall stem shell elements that physically intersect the top half-thickness (1.75 ft) of the footing shell elements are modeled using a rigid material model. Additionally, H-pile (resultant frame) elements intersecting the bottom half-thickness of the footing shell elements are fitted with stiff (frame element) braces. The footing is modeled in this manner to produce flexible pile lengths which correspond to those of the physical footing bottom elevation. Finally, the mass of all elements that fall within the footing thickness is calibrated to equal to the physical footing mass.

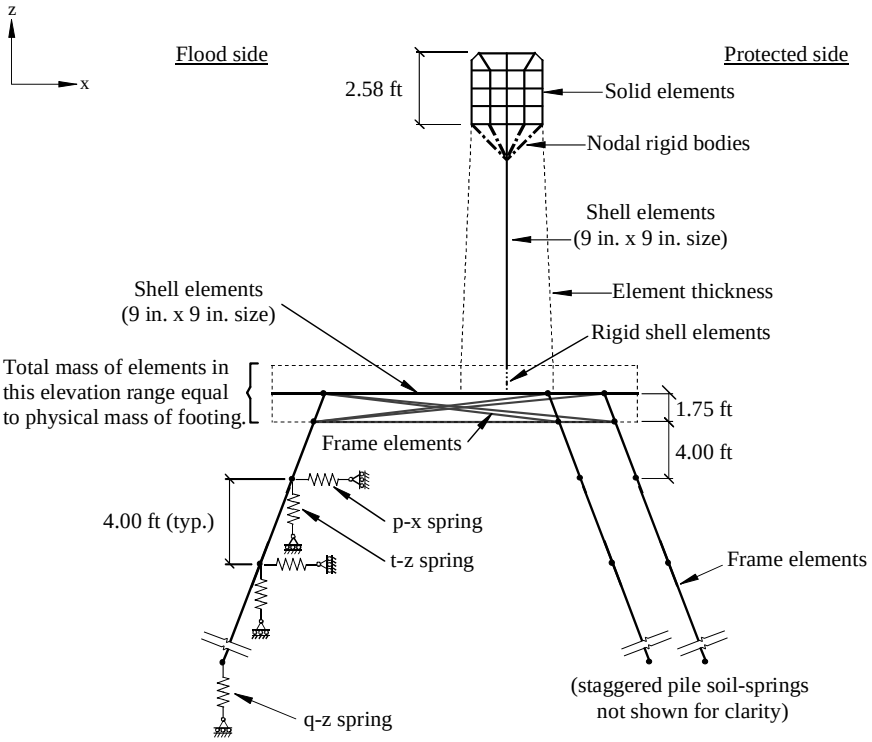

Figure 3.3 Schematic diagram of HPO monolith FE model

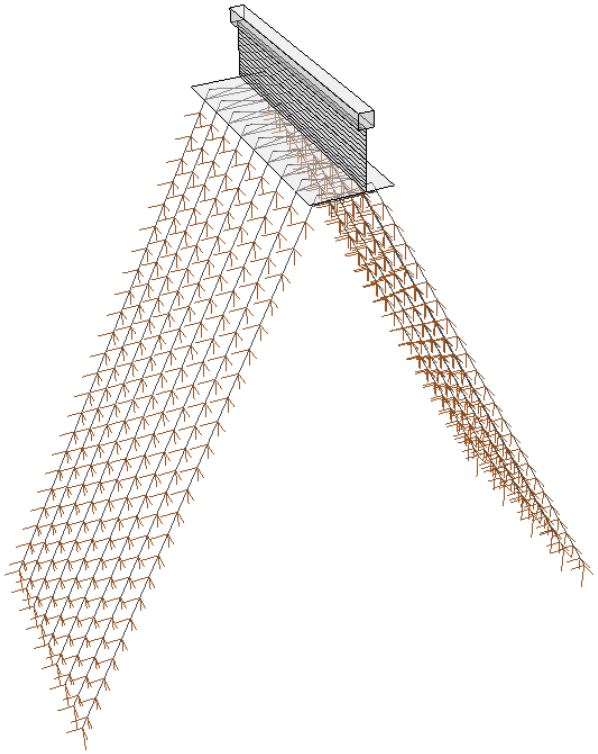

Figure 3.4 HPO monolith FE model (mesh not shown for clarity)

3.2.2 Soil Resistance

Soil resistance for the HPO monoliths is modeled using geotechnical data obtained by the USACE. The corresponding soil-layer profile and soil strength parameters are shown in Figure 3.5 and Table 3.1, respectively. For each soil layer, values of SPT blow counts, unit weight (γ), internal friction angle (ϕ), and undrained shear strength (S_u) are taken directly from the geotechnical report data. Representative design values—not directly available in available geotechnical reports—are used for strain at 50% of failure (ε_{50}), shear modulus (G), and Poisson's ratio (ν) since these parameters are found to have a relatively smaller effect on ultimate soil resistance. Additionally, for each soil layer, empirical correlations (FB-MultiPier 2009, FB-Deep 2009) are used to determine values of subgrade modulus (*k*) and vertical failure shear stress (τ_u). Specifically, for a given depth in the HPO soil profile, *k* and τ_u are formed by correlation using an ensemble average of standard penetration test (SPT) blow counts at the same depth.

Using soil strength parameters (Table 3.1) and H-pile dimensions, empirical force-deformation relationships are quantified (FB-MultiPier 2009) as a representation of soil stiffness. The empirical relationships—comprised of lateral (p-x, p-y), and skin (t-z)—are distributed along the H-piles at 4 ft vertical intervals. Specifically, at each pile node, a set of unique springs is used to model soil resistance at the respective vertical soil depth (Figure 3.3). P-y and p-x soil springs are modeled (as illustrated for a selected spring, in Figure 3.6a) to undergo loading and unloading, where the loading curve is nonlinear and the unloading curve is parallel to the initial slope of the loading. T-z springs are modeled (Figure 3.6b) to undergo nonlinear, elastic force-deformation. The full perimeter of the H-pile cross section (83.7 in.) is included in the t-z spring formulation for all clay layers; whereas, only the rectangular footprint of the H-pile (56.4 in.) is employed for sand layers. Pile tips are fitted with compression-only, nonlinear elastic tip (q-z) springs (Figure 3.6b). For each type of soil-spring, a corresponding set of translational constraints and restraints are employed. Consequently, the element axis for each soil-spring is always oriented parallel to the respective global axis, which ensures that pile deformations are resisted in an appropriate manner (see Consolazio et al. 2002 for details).

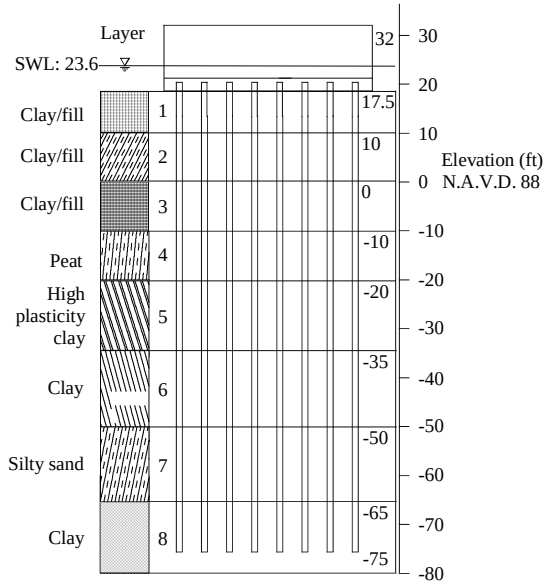

Figure 3.5 Soil-layer profile for HPO monolith

Table 3.1 HPO soil strength parameters

Layer	Soil type	SPT [a]	Top Elev.	γ	ϕ	k	S_u	ε_{50} [c]	G [c]	ν [c]	τ_u
			(ft)	(pcf)	(°)	(pci)	(psf)		(ksi)		(psf)
1	Clay/fill	4	17.5	125	NA	NA	800	0.02	0.279	0.4	343
2	Clay/fill	4	10	115.5	NA	NA	650	0.02	0.279	0.4	337
3	Clay/fill	4	0	115.5	NA	NA	650	0.02	0.279	0.4	337
4	Peat	4	-10	85	NA	NA	750	0.02	0.279	0.4	325
5	High plasticity clay	6	-20	105	NA	NA	648	0.02	0.279	0.4	483
6	Clay	7	-35	105	NA	NA	813	0.02	0.279	0.4	524
7	Silty sand	7	-50	114	30	22.5	NA	NA	0.405	0.2	373
8	Clay	8 [b]	-65	123	NA	NA	1008	0.02	0.279	0.4	612

[a] SPT blow count values are averaged, per layer, using the ensemble average, at each depth, of values from multiple SPT boring profiles.

[b] Ensemble average SPT value at -51 ft used for elevations below -51 ft.

[c] Representative design values used.

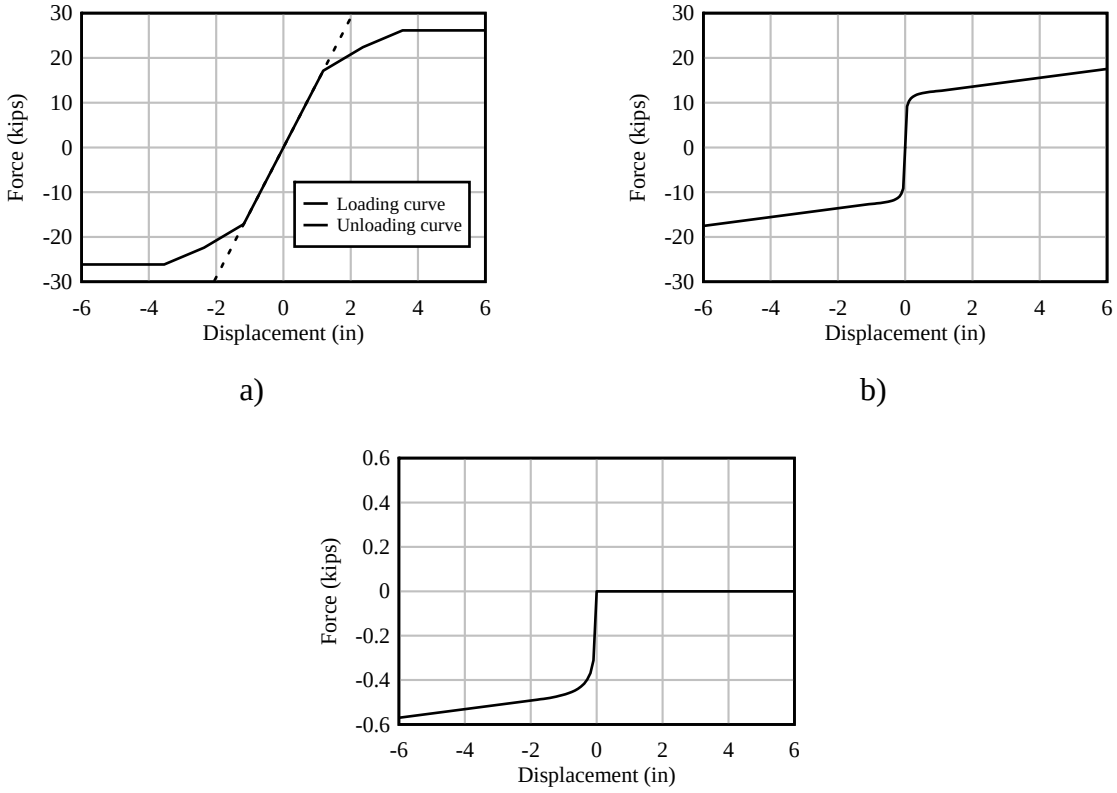

Figure 3.6 Sample soil-springs for HPO monolith: a) P-x, P-y springs at -28.8 ft; b) T-z spring at -28.8 ft; c) Q-z spring at -75 ft (tip)

3.2.3 Non-collision Load Modeling

In addition to self-weight (gravity) loads, breaking wave loads are also included in the HPO monolith FE model (per data obtained by the USACE). Specifically, hydrodynamic pressures are applied (as statically equivalent nodal loads) according to the distribution shown in Figure 3.7. For loaded zones of the monolith that are modeled using solid elements, loads are

applied directly to the element faces. However, for all loaded zones in which shell elements are employed, loads are applied to the element midplanes. Per structural drawings of the wall, the mudline elevation (17.5 ft) coincides with the bottom surface of the monolith footing. Consequently, soil pressure loads are not applied to R/C monolith components.

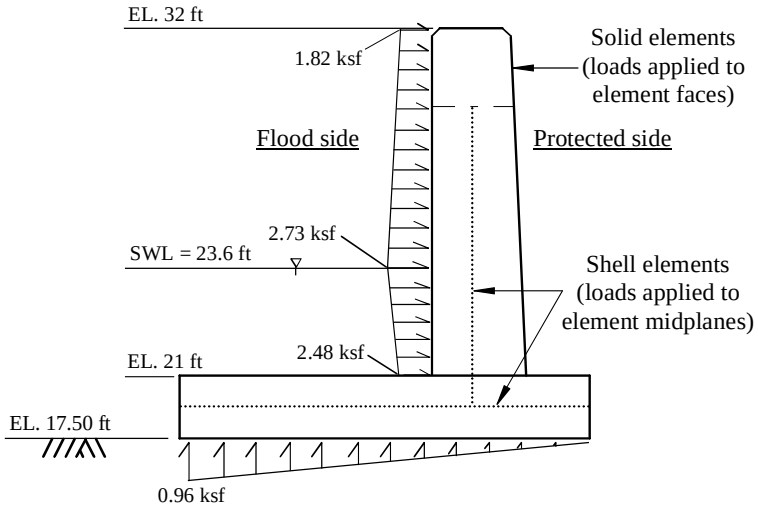

Figure 3.7 Schematic diagram of hydrodynamic loading on HPO monolith

Structural response to non-collision loads is incorporated in a manner analogous to that associated with the barge FE model buoyancy effects (see Section 2.3). Specifically, gravity and hydrodynamic loads are applied to the HPO monolith model and a quasi-static analysis is conducted. As part of the analysis, deformations induced in the underlying soil-springs are quantified. Then, for each soil spring, the corresponding deformation is supplied as an initial offset for all collision simulations conducted. Equilibrium is then approximately satisfied by—for the collision simulations—applying non-collision loads in an instantaneous and continuous manner. Consequently, dynamic oscillation of the HPO monolith in response to the sudden application of non-collision loading is not substantial (oscillations due to non-collision loading reach peak magnitudes of less than 0.5 in.).

3.2.4 Collision Load Contact Surface Modeling

Collision loading is modeled in this study by employing the contact-impact algorithms in LS-DYNA (2009). As part of this process, contact surfaces (i.e., contiguous groups of shell element faces) are defined throughout the monolith. A schematic of the defined contact surfaces for the HPO monolith is shown in Figure 3.8, where all portions of the wall that have the potential to come into contact with the barge during a given impact event are included in the definition. Specifically, the entire footing surface and wall stem on the flood side of the monolith (as well as the top of the wall stem) are defined as contact surfaces. To simplify modeling of the wall stem (which physically only tapers in thickness on the protected side), the wall stem shell elements are tapered on both the flood and protected sides. However, an overriding contact surface is defined along the wall stem that corresponds to the physical monolith wall stem surface.

Both normal and friction contact forces are accounted for as part of the contact-impact algorithms employed. Values of 0.50 and 0.45 are used, respectively, for static and dynamic coefficients of friction between HPO monolith (concrete) and barge (steel) surfaces.

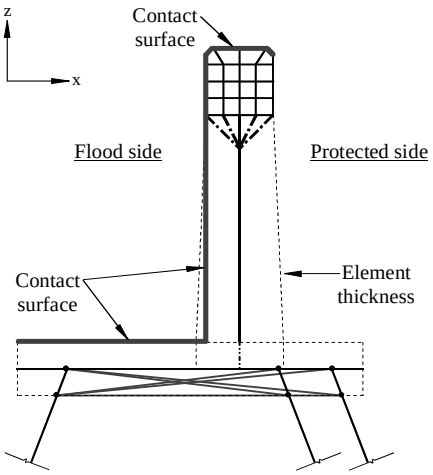

Figure 3.8 Schematic diagram of HPO monolith contact surfaces

3.3 Protection and Restoration Office (PRO) Wall Located Near Algiers Canal

3.3.1 Structural Configuration

The structural configuration for the PRO monolith considered in this study (Transition monolith T2 near Algiers Canal in Plaquemines Parish, Louisiana) is shown in Figures 3.9 - 3.10. The monolith is 27 ft in length with a relatively short wall stem height of 4.5 ft. Between each set of adjacent monoliths is a non-structural, flexible waterstop. Consequently, as is the case in the HPO wall model (Section 3.2), each monolith in the PRO wall model is represented as a separate unit that is not structurally connected to adjacent monoliths. The PRO monolith reinforced concrete footing and wall stem are supported on two rows of 14 in. (square) prestressed concrete piles spaced at 4.5 ft. The piles are inclined at 1:2 (horizontal-to-vertical) and are embedded more than 50 ft into the soil (Figure 3.9).

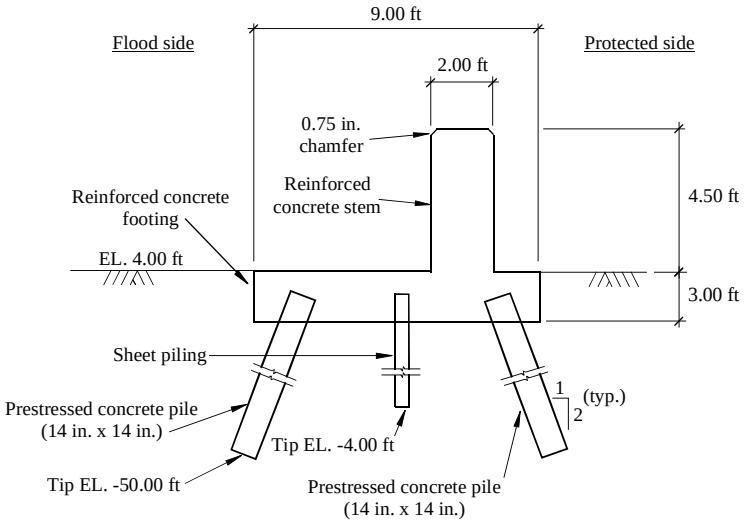

Figure 3.9 Cross-section of PRO monolith

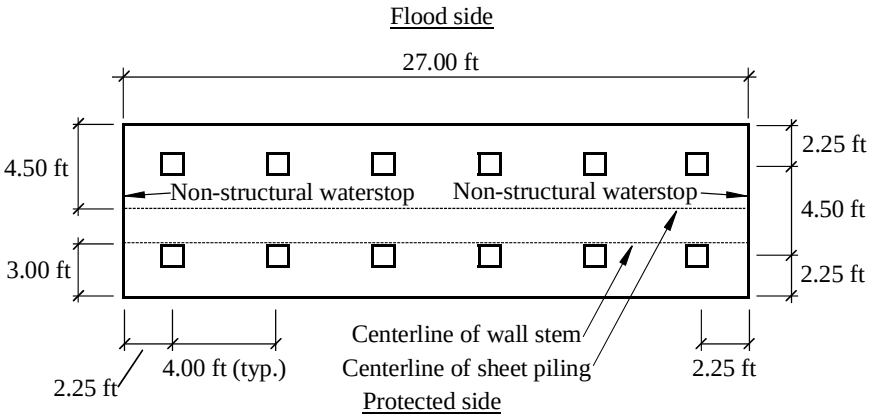

Figure 3.10 Plan view of PRO monolith

A schematic diagram of the PRO monolith FE model is shown in Figure 3.11, and the FE model is shown in Figure 3.12. In concept, the schematic is identical to that of the HPO wall; only the specific pile type and member dimensions are different. It is assumed that the piles of the PRO monolith are prestressed primarily to resist pile-installation (driving) stresses, and hence, prestress forces are not included in the PRO structural FE model. Furthermore, linear elastic material models are employed for reinforced concrete (3600 ksi elastic modulus) and steel (29000 ksi elastic modulus) PRO monolith components. Note that, as with the HPO monolith model, sheet piling is not included in the PRO structural FE model (the sheet piling embedment depth is less than 10 ft).

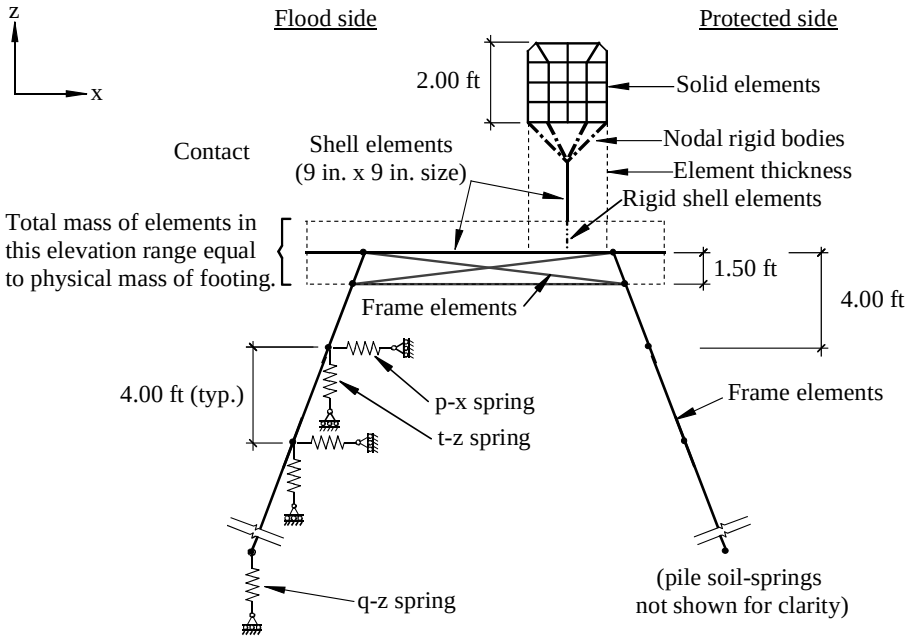

Figure 3.11 Schematic diagram of PRO monolith FE model

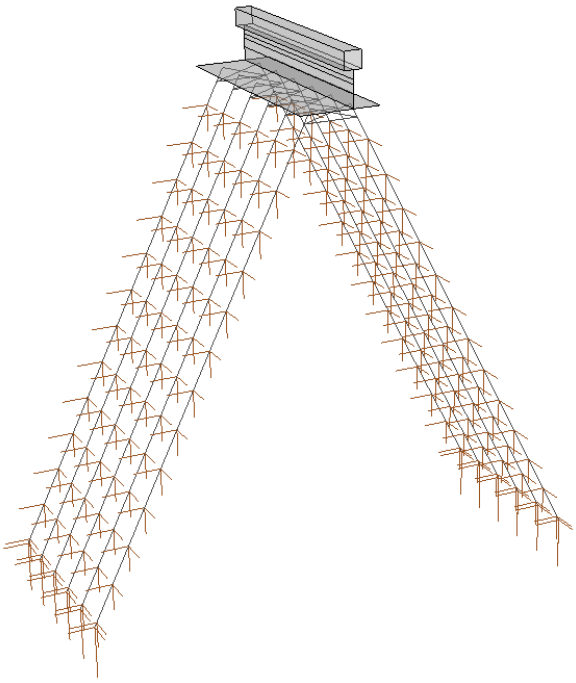

Figure 3.12 PRO monolith FE model (mesh not shown for clarity)

3.3.2 Soil Resistance

The soil-layer profile (based on data obtained by the USACE) for the PRO monolith is shown in Figure 3.13. As with that of the HPO monolith soil, values of γ, ϕ, and S_u for the PRO monolith soil are taken directly from available geotechnical data (Table 3.2). In turn, values of k and τ_u are estimated from ϕ and S_u, respectively. Furthermore, representative design values are employed for ε_{50}, G, and ν. Using the soil strength parameters from Table 3.2 and pile dimensions (a 56 in. pile perimeter is employed for all layers), soil resistance is incorporated into the PRO monolith FE model as unique sets of nonlinear soil-springs at all pile element nodes throughout each soil layer. Note that pile nodes are spaced at 4 ft apart vertically (Figure 3.11).

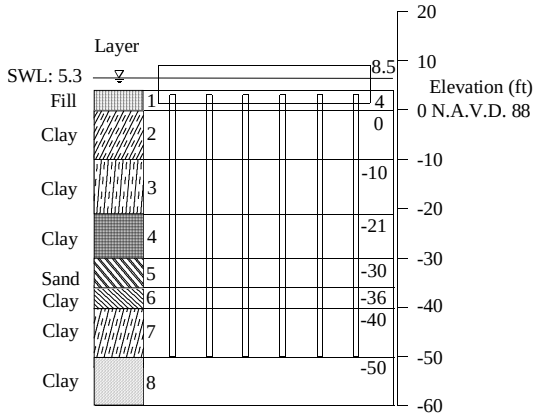

Figure 3.13 Soil-layer profile for PRO monolith

Table 3.2 PRO soil strength parameters

Layer	Soil type	Top Elev.	γ	ϕ	k [a]	S_u	ε_{50} [b]	G [b]	ν [b]	τ_u [c]
		(ft)	(pcf)	(°)	(pci)	(psf)		(ksi)		(psf)
1	Fill	4	110	NA	NA	400	0.02	0.279	0.4	413
2	Clay	0	87	NA	NA	400	0.02	0.279	0.4	413
3	Clay	-10	87	NA	NA	325	0.02	0.279	0.4	349
4	Clay	-21	108	NA	NA	500	0.02	0.279	0.4	490
5	Sand	-30	122	30	30	NA	NA	1.11	0.25	375 [a]
6	Clay	-36	108	NA	NA	567	0.02	0.279	0.4	537
7	Clay	-40	104	NA	NA	628	0.02	0.279	0.4	575
8	Clay	-50	104	NA	NA	714	0.02	0.279	0.4	625

[a] Estimated from angle of internal friction.

[b] Representative design values used.

[c] Unless otherwise noted, estimated from undrained shear strength per Tomlinson (1994).

3.3.3 Non-collision Load Modeling

Non-collision loading (gravity and wave loading) and structural response schemes employed in the PRO monolith FE model are identical to those used for the HPO monolith FE model. For the PRO monolith, however, wave pressures are relatively small in magnitude (Figure 3.14). In addition, consistent with that of the HPO monolith FE model, soil pressures are not applied to R/C elements in the PRO monolith FE model.

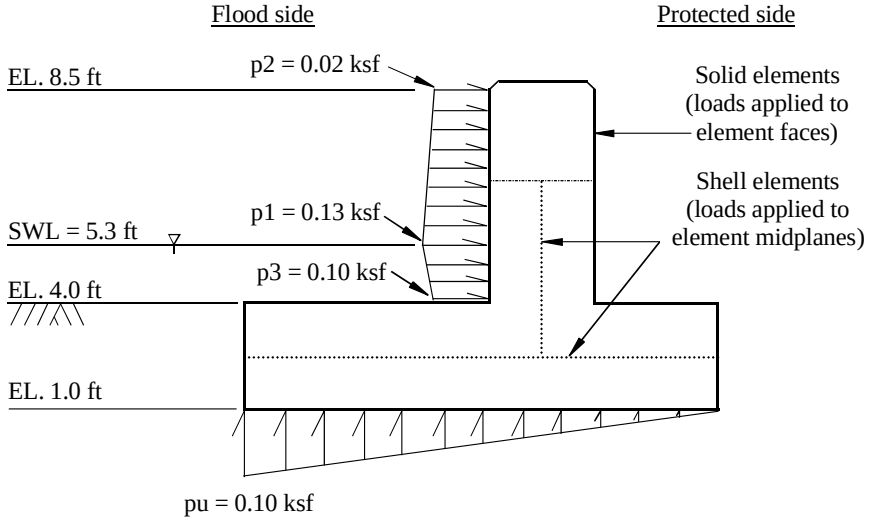

Figure 3.14 Schematic diagram of PRO monolith hydrostatic and hydrodynamic loading

3.3.4 Collision Load Contact Surface Modeling

A schematic of the designated contact surfaces for the PRO monolith FE model is shown in Figure 3.15. The model contact definition consists of contiguous surfaces throughout the horizontal footing surface on the flood side; vertical wall stem on the flood side; and, top of the wall stem. For the shell elements of the wall stem and footing, all contact surfaces are representative of the respective, physical monolith surfaces (i.e., contact is defined on the projected half-thickness of the shell elements on the flood side). The same concrete-steel friction scheme is employed as part of the PRO monolith and barge contact definition as that specified between the HPO monolith and the barge.

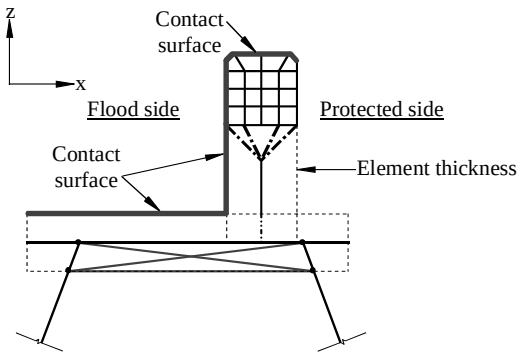

Figure 3.15 Schematic diagram of PRO monolith contact surfaces

3.4 PRO Fronting Protection (Dolphin) System Located Near Hero Pumping Station

3.4.1 Structural Configuration

The PRO dolphin unit considered in this study is based on those units in the dolphin cluster near Hero Pumping Station in New Orleans, Louisiana. The structural configuration for a single dolphin unit is shown in Figures 3.16 - 3.17. Atop the dolphin is a 4 ft thick, reinforced concrete cap with the shape of an irregular hexagon. Underlying the cap are three equilaterally oriented steel pipe piles, where each pile is inclined 3:1 vertical-to-horizontal and braced near the pile head with a W12x40 steel beam. The piles are filled with concrete from the pile head to an elevation of -18 ft. From -18 ft to the pile tip elevation (-135 ft), the steel pipe piles are plugged with soil.

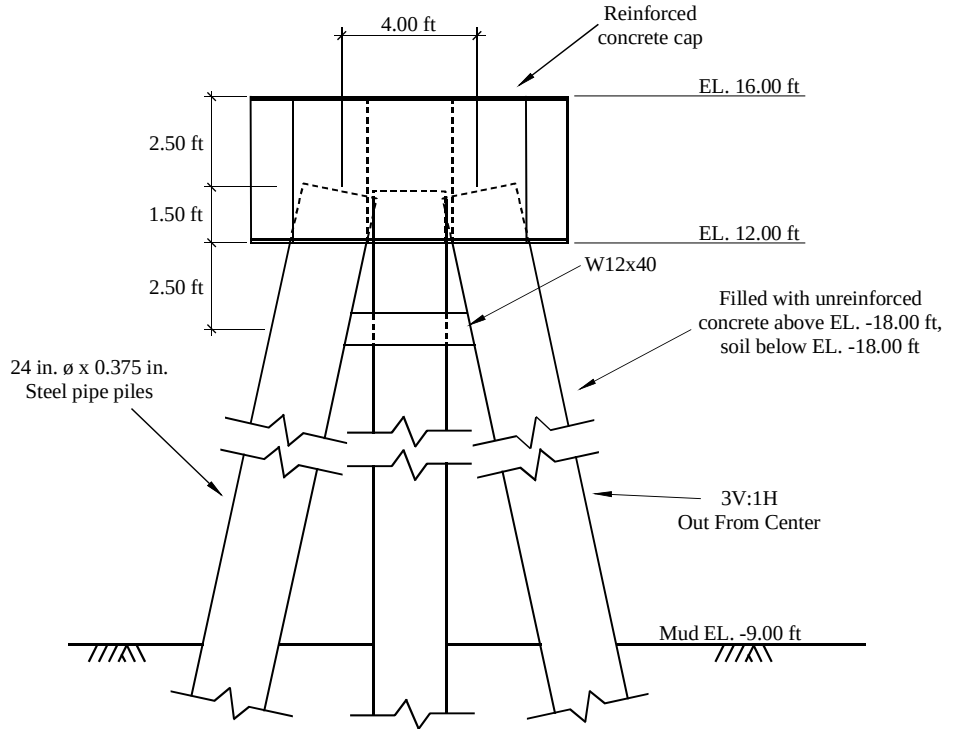

Figure 3.16 Cross-section of PRO dolphin unit

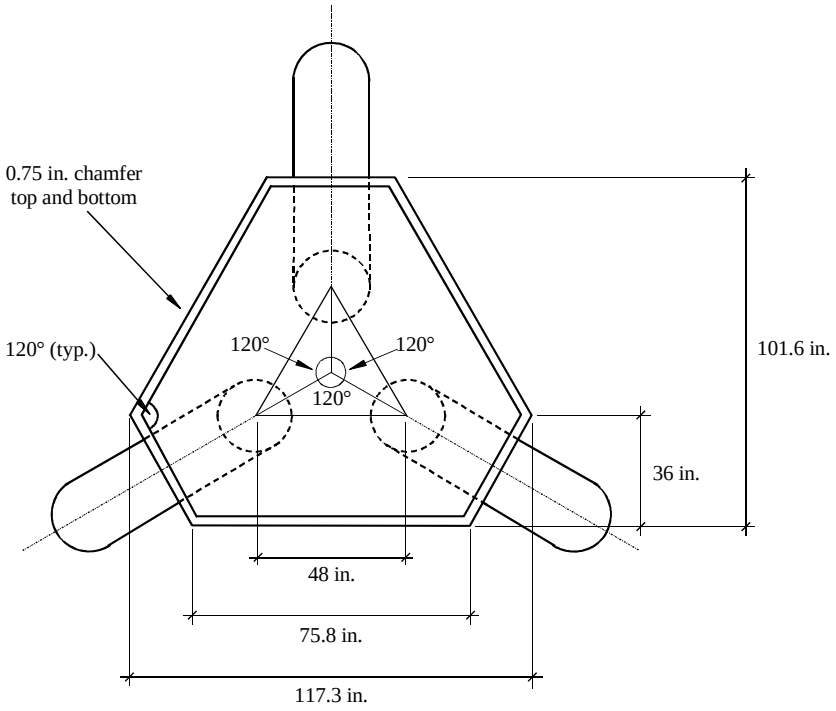

Figure 3.17 Plan view of PRO dolphin unit

A schematic diagram of the PRO dolphin FE model is shown in Figure 3.18. A rendering of the FE model is shown in Figure 3.19, showing the chosen element discretization. The dolphin cap is modeled using 9-in. solid elements with a linear-elastic concrete material model (3600 ksi elastic modulus). As with the HPO and PRO monoliths, a 0.75-in. chamfer is included along all cap edges.

Typically, the purpose of protective structures of this kind is to absorb significant collision energy through inelastic material deformation. Given the cap is 4 ft thick, nonlinear deformation in the cap is unlikely. Thus, a linear-elastic material model was used, as described previously. However, it was important to model the piles using refined, cross section-integrated beam elements, paired with representative nonlinear material descriptions. The strut members connecting each pile are also modeled in this manner.

To capture detailed nonlinear pile deformation, specialized cross section-integrated beam elements are used. For this type of element, the element cross section is discretized into multiple regions (Figure 3.20), each with a corresponding integration point—similar to other types of FE discretization. As the beam element deforms, strains and corresponding stresses are computed at each integration point, and these stresses are summed (numerically integrated) to form section forces and moments. The steel pipe piles, concrete pile plugs, and W-section struts were all modeled using cross section-integrated beam elements with approximately 100 integration points in each cross-section.

Detailed cross section modeling permits the direct use of nonlinear material models, since each integration point may have a unique magnitude of stress and strain. Thus, a nonlinear concrete model is employed for the plain concrete pile plug (maximum compressive stress of 4 ksi). The concrete material model includes strain-softening at large compressive strains, and cracking. Similarly, a nonlinear structural steel model (60-ksi yield stress, 90-ksi ultimate stress) is utilized for the steel pipe piles and wide-flange struts.

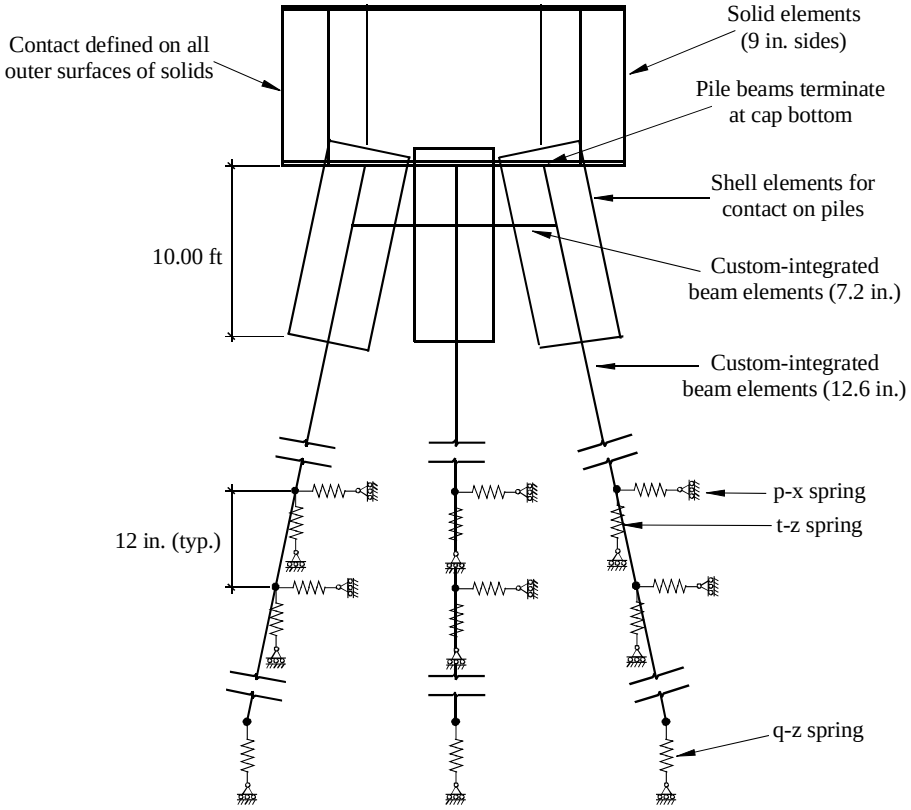

Figure 3.18 Schematic diagram of PRO dolphin FE model

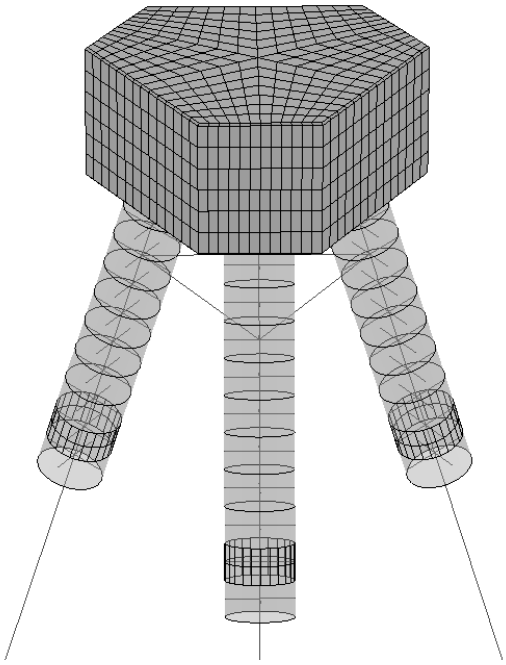

Figure 3.19 Rendering of PRO dolphin FE model (selected meshing shown)

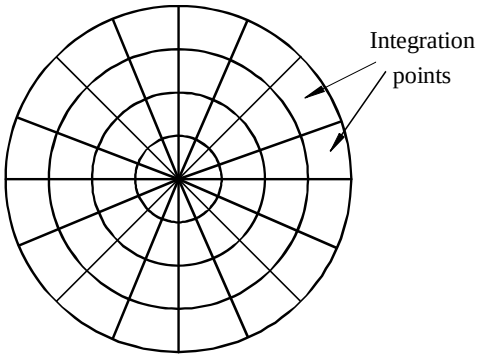

Figure 3.20 Pile beam element cross section-integration scheme
(only 64 integration points shown for clarity)

As shown in the PRO dolphin construction drawings, the steel pipe piles are filled with plain concrete between the cap and an elevation of -18 ft (Figure 3.21). The piles in this region were modeled using two collinear, nonlinear beam elements—one to represent the steel pipe, and one to represent the concrete plug. At a given location, both collinear elements share nodal degrees-of-freedom, enforcing strain compatibility between the concrete plug and steel pipe. At elevations below -18 ft, the pipe piles are assumed to be plugged with soil. It was assumed that the soil plug provides no structural resistance (through stiffness). However, for dynamic purposes, the mass of the soil plug was included by means of concentrated nodal masses (Figure 3.21).

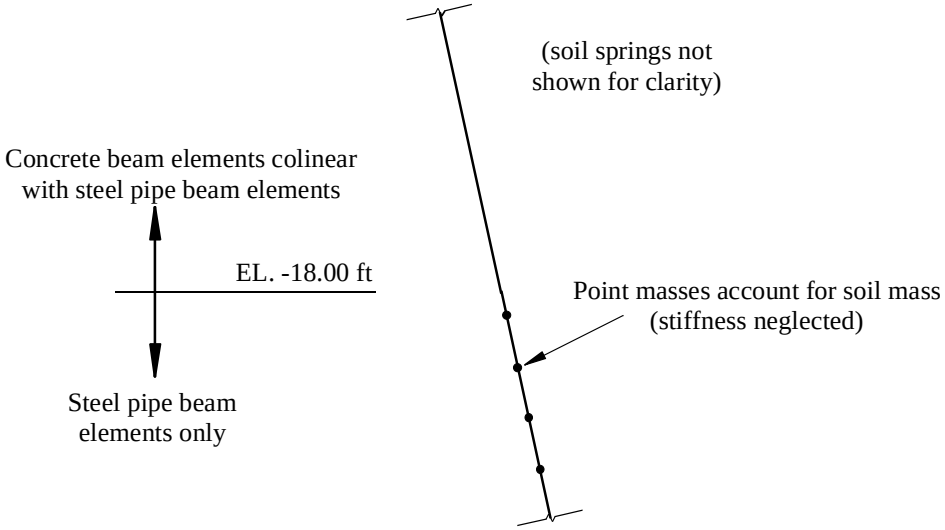

Figure 3.21 Pile frame element modeling

For the PRO dolphin model, connections between piles elements and the cap are modeled as fixed. That is, it is assumed that sufficient embedment or mechanical anchorage exists to develop the full pile moment capacity without failing the connection. In the model, fixity was accomplished means of an array of rigid elements, linking the pile beam elements to the cap solid elements. As illustrated in Figure 3.22, the rigid elements were connected to every cap node falling within the approximate pile footprint. This modeling scheme enforces rotational continuity at the pile head at any reasonable level of deformation.

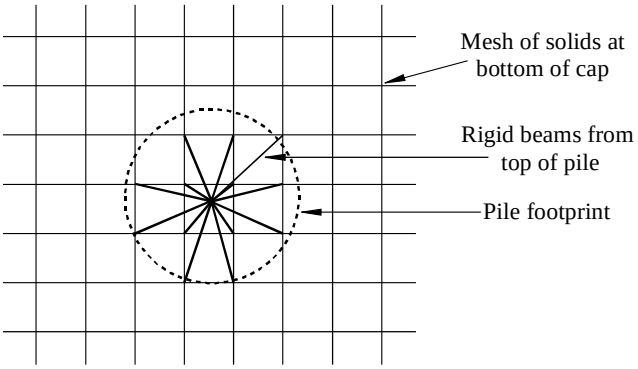

Figure 3.22 Connection model between pile frame elements and cap solid elements

3.4.2 Soil Resistance

The soil-layer profile and soil strength parameters for the PRO dolphin structure are presented in Figure 3.23 and Table 3.3, respectively. The means by which soil strength parameters are determined for the PRO dolphin soil model are largely consistent with those employed for the HPO monolith model. It should be noted, however, that values of undrained shear strength (S_u), provided by the USACE, are specific to a single boring. In contrast, values of vertical failure shear stress (τ_u) are determined based on correlations to, per layer, an ensemble average of SPT blow counts from multiple borings. Consequently, values of τ_u vary significantly relative to the available S_u values of respective soil layers.

Soil resistance is modeled in the dolphin structural FE model through the application of distributed nonlinear soil-springs along all embedded pile nodes. This modeling approach is consistent with the corresponding processes used in both the HPO and PRO monolith models. However, in accordance with the steel pipe-pile element discretization, soil-springs in the PRO dolphin model are densely spaced (at 1 ft vertical intervals) relative to the respective spacing intervals used in the HPO and PRO monolith FE models.

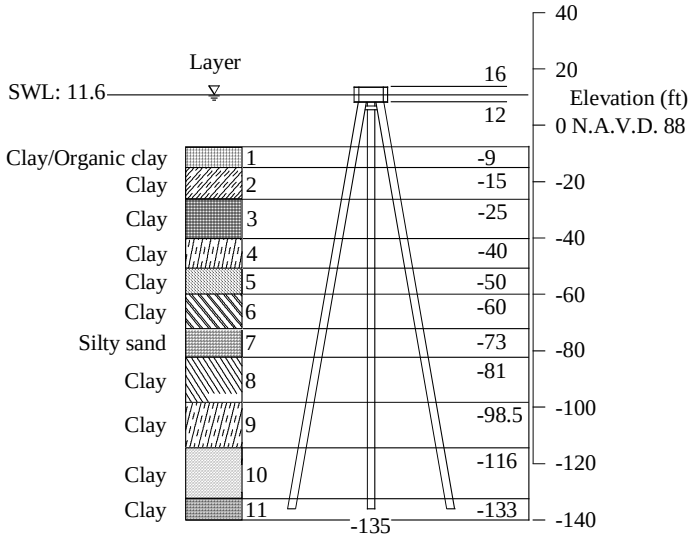

Figure 3.23 Soil-layer profile for dolphin structure

Table 3.3 Dolphin structure soil strength parameters

Layer	Soil type	SPT [a]	Top Elev.	γ	ϕ	k	S_u	ε_{50} [c]	G [c]	ν [c]	τ_u
			(ft)	(pcf)	(°)	(pci)	(psf)		(ksi)		(psf)
1	Clay/Organic clay	4	-9	80	NA	NA	115	0.02	0.279	0.4	373
2	Clay	5	-15	110	NA	NA	193	0.02	0.279	0.4	550
3	Clay	8	-25	98	NA	NA	348	0.02	0.279	0.4	760
4	Clay	6	-40	104	NA	NA	473	0.02	0.279	0.4	623
5	Clay	6	-50	101.5	NA	NA	560	0.02	0.279	0.4	638
6	Clay	9	-60	101	NA	NA	600	0.02	0.279	0.4	805
7	Silty sand	24	-73	122.5	30	113	NA	NA	1.115	0.25	1356
8	Clay	12	-81	119	NA	NA	709	0.02	0.279	0.4	1004
9	Clay	10	-98.5	119	NA	NA	876	0.02	0.279	0.4	916
10	Clay	9 [b]	-116	116	NA	NA	1040	0.02	0.279	0.4	860
11	Clay	9 [b]	-133	116	NA	NA	1200	0.02	0.279	0.4	860

[a] SPT blow count values are averaged, per layer, using the ensemble average, at each depth, of values from multiple SPT boring profiles.

[b] SPT blow count estimated based on single SPT boring profile.

[c] Representative design values used.

3.4.3 Non-collision Load Modeling

Due to the small submerged surface area of the dolphin (relative to those of the HPO and PRO monoliths), wave loading is neglected in the PRO dolphin FE model. Gravity loading, however, is present in the model. The non-collision (gravity) loading and structural response schemes employed for the PRO dolphin FE model are identical to those used for the HPO monolith and PRO monolith FE models. Application of body (gravity) forces to the PRO dolphin FE model results in only a nominal response. Consequently, only nominal dynamic oscillation occurs when the non-collision loads are applied instantaneously in conjunction with initial soil-spring offsets throughout the PRO dolphin FE model.

3.4.4 Collision Load Contact Surface Modeling

A schematic of the designated contact surfaces for the PRO dolphin FE model is shown in Figure 3.24. The dolphin (concrete) to barge (steel) contact definition includes all external cap surfaces. The concrete-to-steel frictional parameters employed are the same as those used for the HPO monolith model. The top of the reinforced concrete cap is included in the contact definition to account for the possibility that—during collision—the raked barge bow bottom surface may "climb" a given dolphin and come to rest on the top of the dolphin cap.

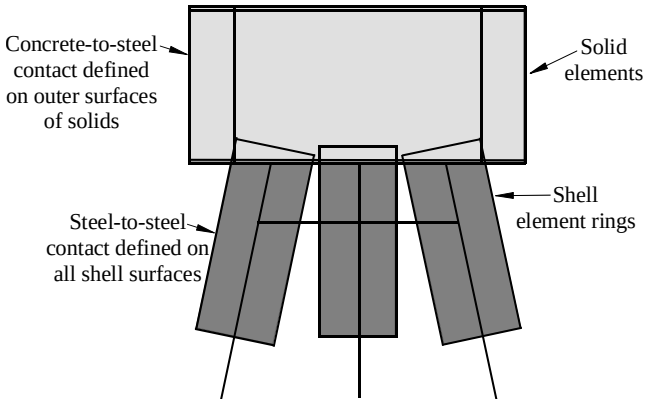

Figure 3.24 Schematic diagram of PRO dolphin contact surfaces

Depending on barge draft, contact with pile members is possible. However, these members are modeled with one-dimensional beam elements. No suitably accurate contact algorithm is available in LS-DYNA to directly model contact between the shell-element barge, and beam-element piles. Consequently, a contact scheme that provides a physically accurate contact surface is employed in which beam elements are used to model the pile structural resistance and shell elements are employed to model contact (Figure 3.25). In the potential contact region—approximately, the top 10 ft of pile length—a series of rigid, 24-in. diameter shell-element rings are used as a contact surface. The rings are connected to pile nodes by means of rigid links. Because each ring is structurally independent, large-scale pile deformation (flexure and shear) is permitted without interference. The contact rings merely provide a means of simulating the physically correct contact geometry and transmitting resulting contact forces to the structure. Steel-barge-to-steel-pile frictional parameters employed in the PRO dolphin FE model are the same as those used in the barge self-contact (steel-to-steel) definition.

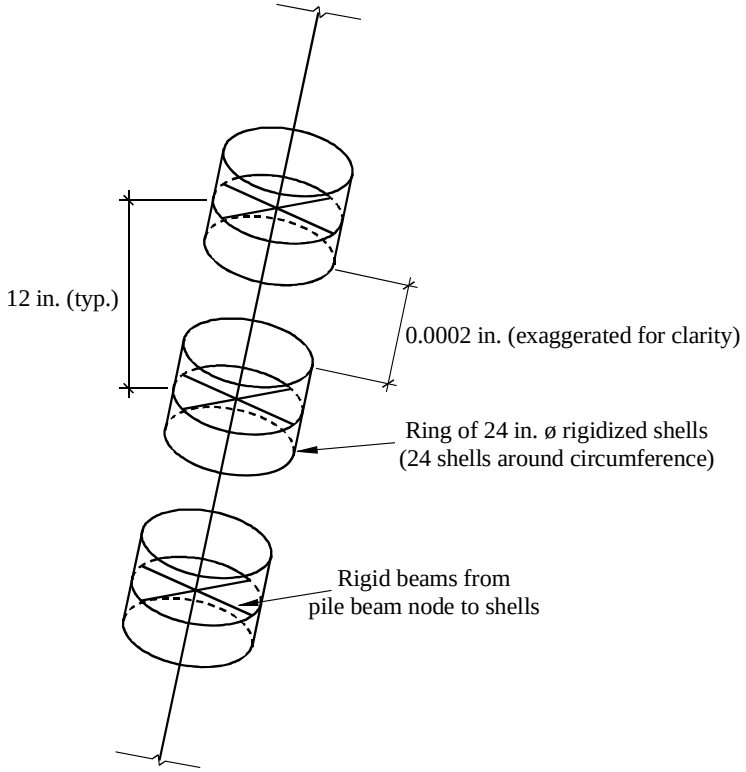

Figure 3.25 Schematic of contact scheme for pile beam elements

CHAPTER 4
SIMULATION RESULTS

4.1 Overview of Simulation Matrix

Using high-resolution finite element models of the hopper barge, HPO wall, PRO wall, and PRO dolphin structures, more than 50 fully dynamic impact simulations were conducted. Of the full simulation set, 24 impact scenarios serve as a baseline for comparison. As summarized in Table 4.1, the baseline simulation set consists of empty hopper barge impacts at various angles with respect to the wall or line of dolphins. For the baseline simulations, most model parameters are held constant (i.e., barge weight, draft, and initial velocities), and only the impact angle is varied. The eight impact cases shown in Table 4.1 were simulated for each of the structures of interest—HPO wall, PRO wall, and PRO dolphin. Force-histories and maximum forces predicted by the baseline simulations are presented in Sections 4.2 through 4.5.

Table 4.1 Baseline impact cases for HPO wall, PRO wall, and PRO dolphin

Impact condition	Impact angle (°)	Barge weight	Barge draft (ft)	Initial X-velocity (knot)	Initial Y-velocity (knot)
Barge side	0	Empty (362 tons)	2	5	1
Barge bow	1	Empty (362 tons)	2	5	1
Barge bow	15	Empty (362 tons)	2	5	1
Barge bow	30	Empty (362 tons)	2	5	1
Barge bow	45	Empty (362 tons)	2	5	1
Barge bow	60	Empty (362 tons)	2	5	1
Barge stern	15	Empty (362 tons)	2	5	1
Barge stern	60	Empty (362 tons)	2	5	1

In addition to the baseline impact cases, approximately 30 supplemental simulations were conducted to assess the sensitivity of impact forces to various model parameters such as barge positioning, impact velocity, soil resistance, and pile fixity. Results for these sensitivity analyses are presented later in this chapter.

4.2 Baseline Simulation Force-Histories—HPO Wall

In this section, force-histories for the baseline simulation set are presented, involving impact with the HPO wall structure (Figure 4.1). Different wall monoliths are engaged during impact, depending on the impact scenario. For example, four monoliths are engaged simultaneously during a perfect side impact (0° angle). Thus, for this case, the force-history shown in Figure 4.2 is a single trace showing the force *per monolith*, since the force on each engaged monolith is essentially identical. During oblique impact scenarios (Figures 4.3 - 4.9), initial contact is made with one or two wall monoliths, which induces rotational motion in the barge. Presumably, given sufficient time, barge rotation would eventually cause a subsequent impact when the opposite end of the barge collides with the wall. However, a significant portion of the initial barge kinetic energy is absorbed during the initial impact, through inelastic deformation, which diminishes the available energy for subsequent impact. Fluid cushioning effects would also reduce the velocity of the subsequent impact, thus, subsequent impacts caused by barge rotation were not considered as part of this study.

Force-history data for each impact scenario are presented in Figures 4.2 - 4.9. Force-histories presented here are considered “raw” data and have been only minimally filtered using a 100-Hz low-pass filter to eliminate high-frequency noise in the simulation results. Only

x-direction (transverse to the wall) forces are presented here [see Appendix A for x, y, and z-direction forces]. Schematics of each impact condition are also included in Figures 4.2 - 4.9. Wall monoliths that were actively engaged during the initial impact are highlighted in grey.

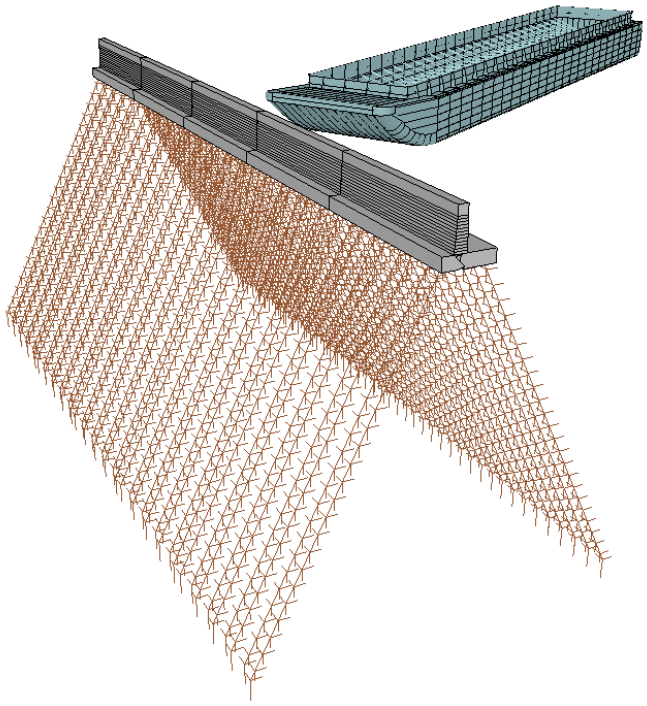

Figure 4.1 Rendering of barge impact simulation with HPO wall

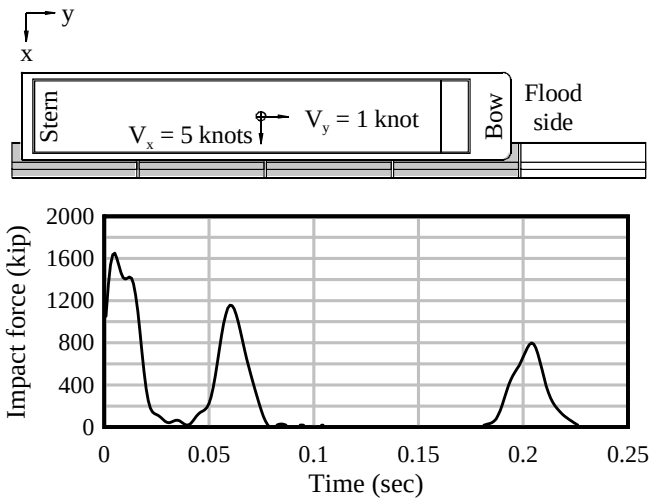

Figure 4.2 Empty barge, sidewall impact, HPO wall, 0° angle, x-direction force-history (note: impact force shown is *per monolith*)

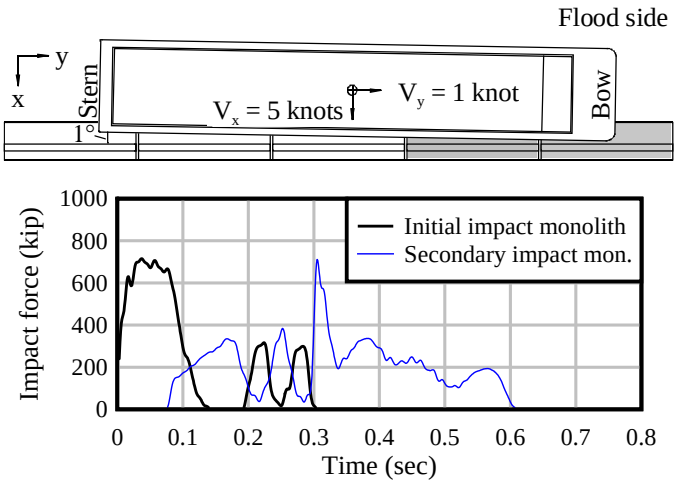

Figure 4.3 Empty barge, bow impact, HPO wall, 1° angle, x-direction force-history

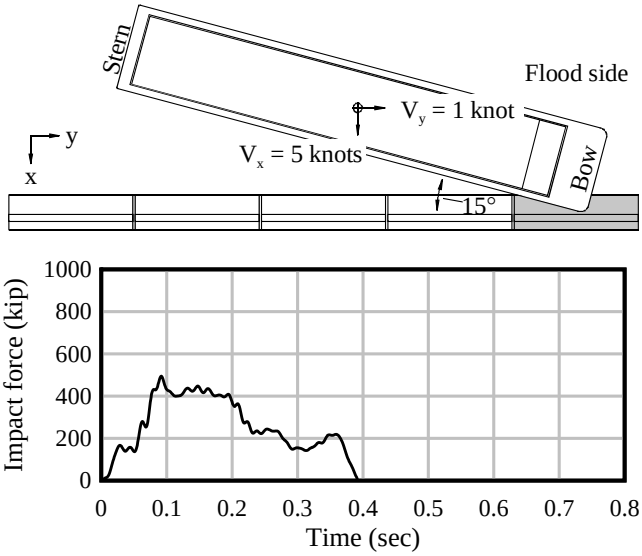

Figure 4.4 Empty barge, bow impact, HPO wall, 15° angle, x-direction force-history

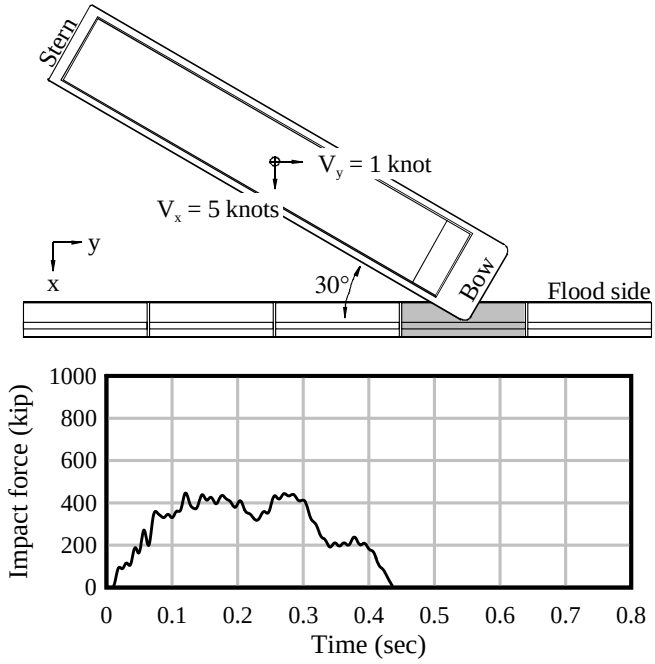

Figure 4.5 Empty barge, bow impact, HPO wall, 30° angle, x-direction force-history

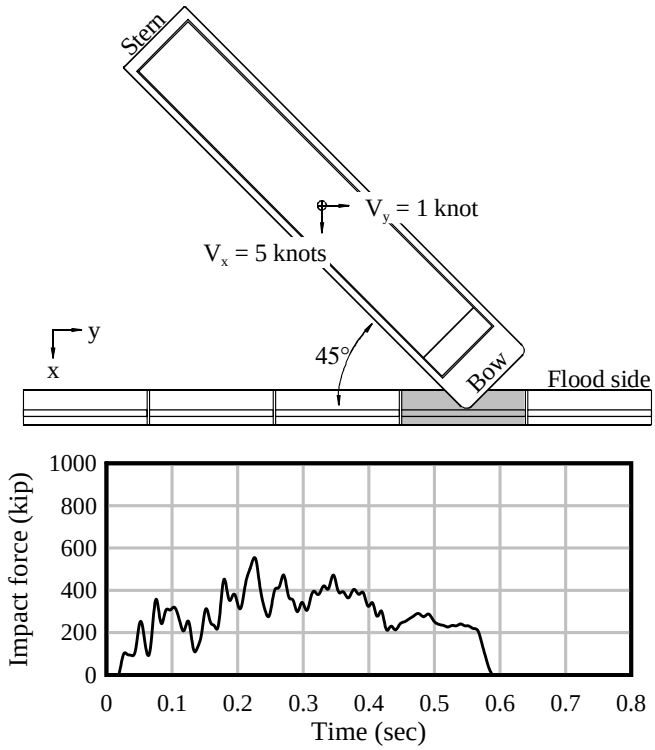

Figure 4.6 Empty barge, bow impact, HPO wall, 45° angle, x-direction force-history

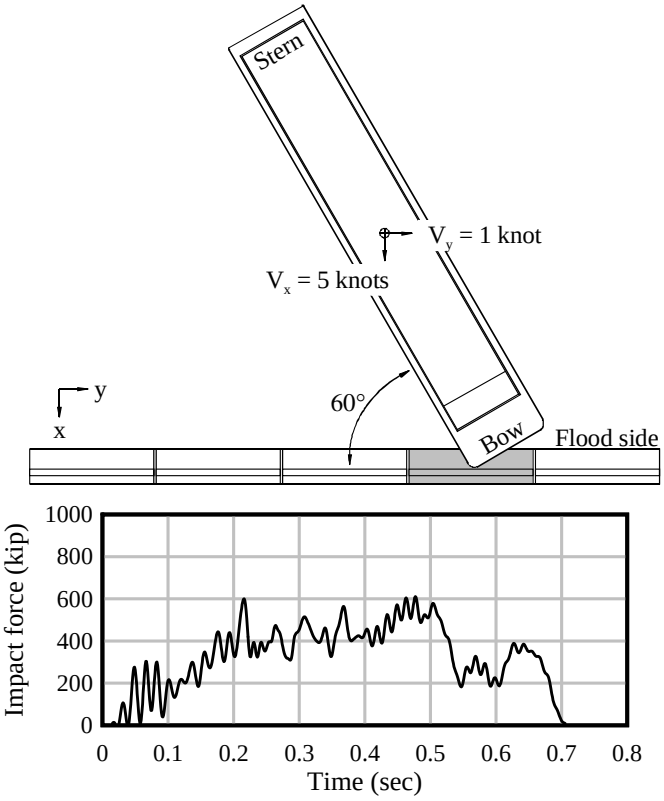

Figure 4.7 Empty barge, bow impact, HPO wall, 60° angle, x-direction force-history

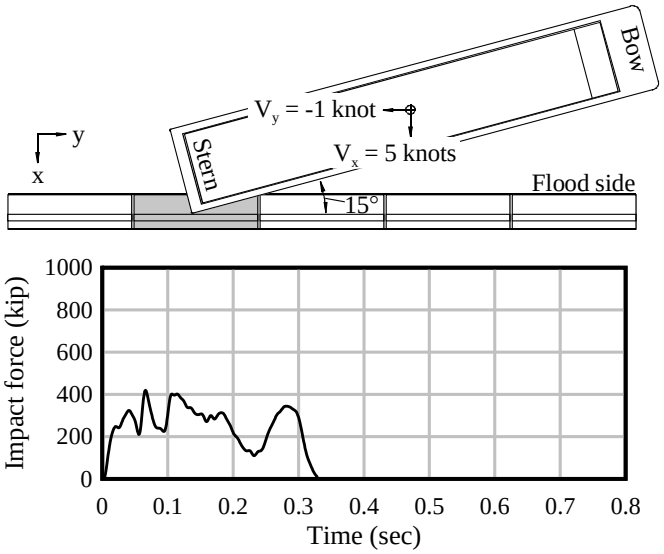

Figure 4.8 Empty barge, stern impact, HPO wall, 15° angle, x-direction force-history

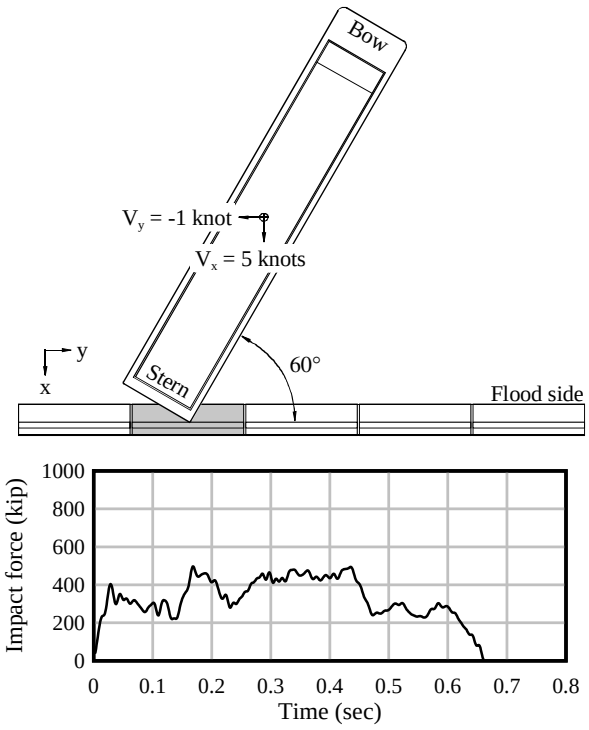

Figure 4.9 Empty barge, stern impact, HPO wall, 60° angle, x-direction force-history

4.3 Baseline Simulation Force-Histories—PRO Wall

In this section, force-histories for the baseline simulation set are presented, involving impact with the PRO wall structure (Figure 4.10). Presentation of force-histories and impact schematics in Figures 4.11 - 4.18 is identical to that of the HPO wall results. Note that during a perfect side impact (Figure 4.11), eight PRO wall monoliths are engaged simultaneously, compared to four for the HPO wall. Thus, per monolith forces are much smaller for the PRO wall. As before, only x-direction (transverse to wall) forces are presented here [See Appendix B for x, y, and z-direction forces].

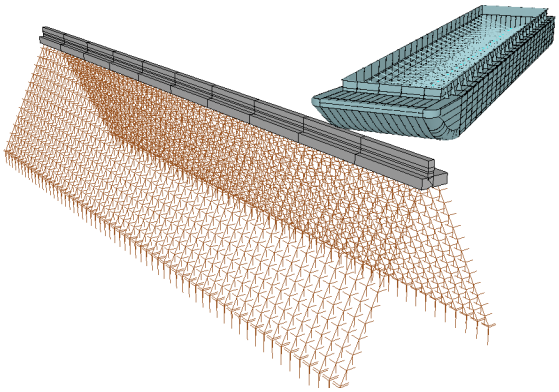

Figure 4.10 Rendering of barge impact simulation with PRO

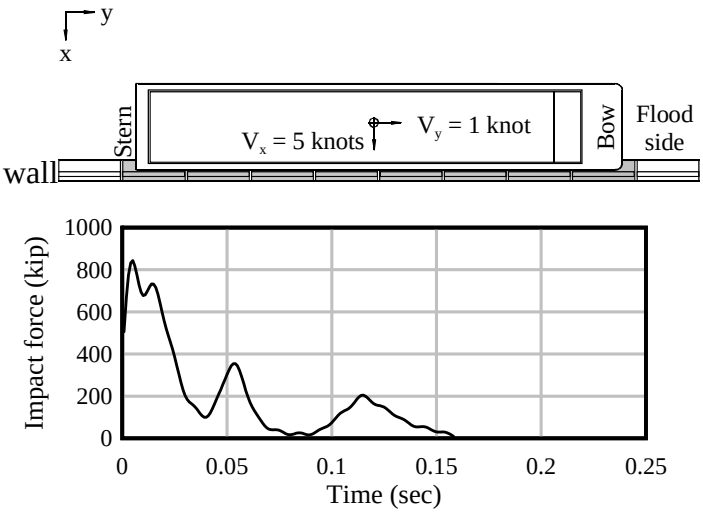

Figure 4.11 Empty barge, sidewall impact, PRO wall, 0° angle, x-direction force-history (note: impact force shown is *per monolith*)

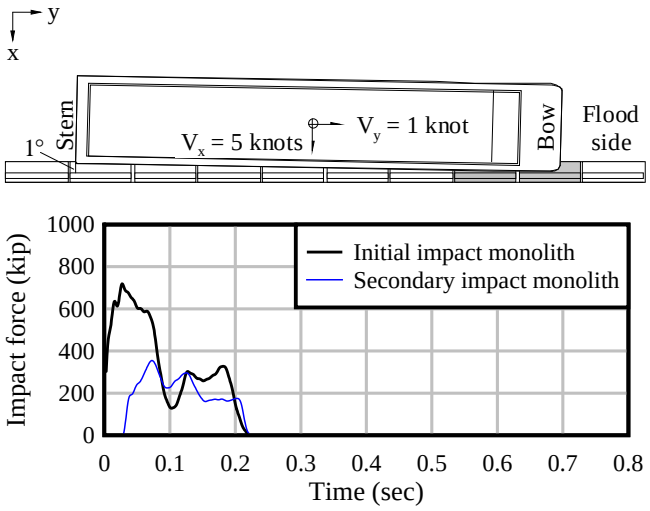

Figure 4.12 Empty barge, bow impact, PRO wall, 1° angle, x-direction force-history

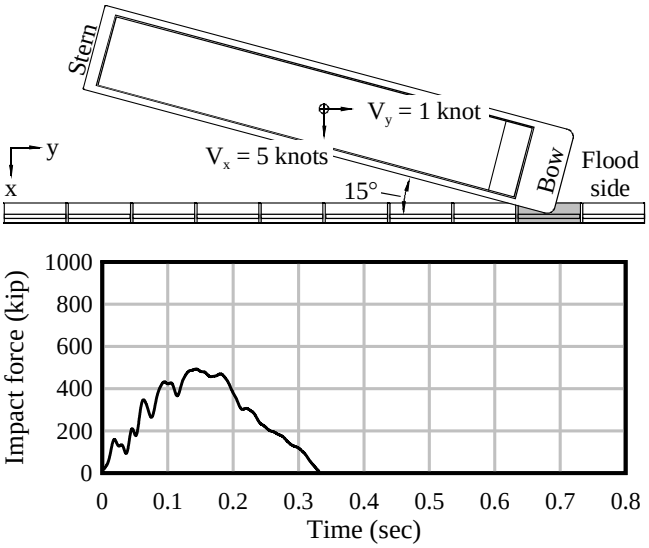

Figure 4.13 Empty barge, bow impact, PRO wall, 15° angle, x-direction force-history

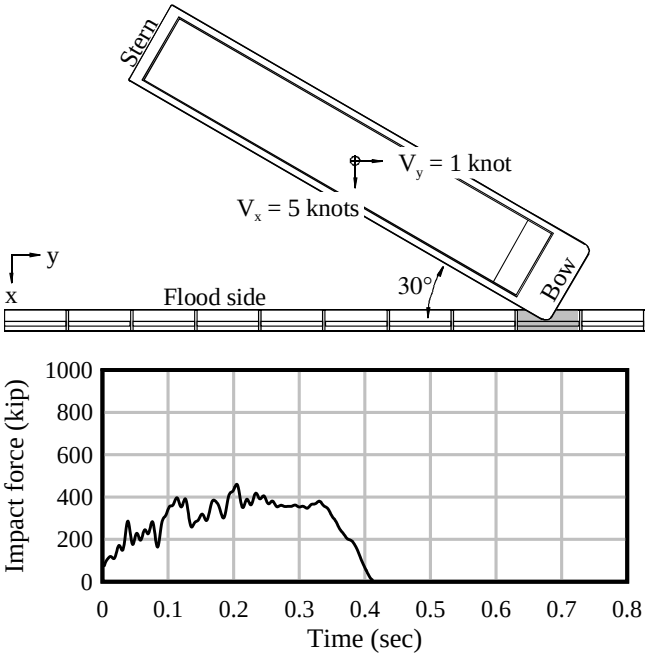

Figure 4.14 Empty barge, bow impact, PRO wall, 30° angle, x-direction force-history

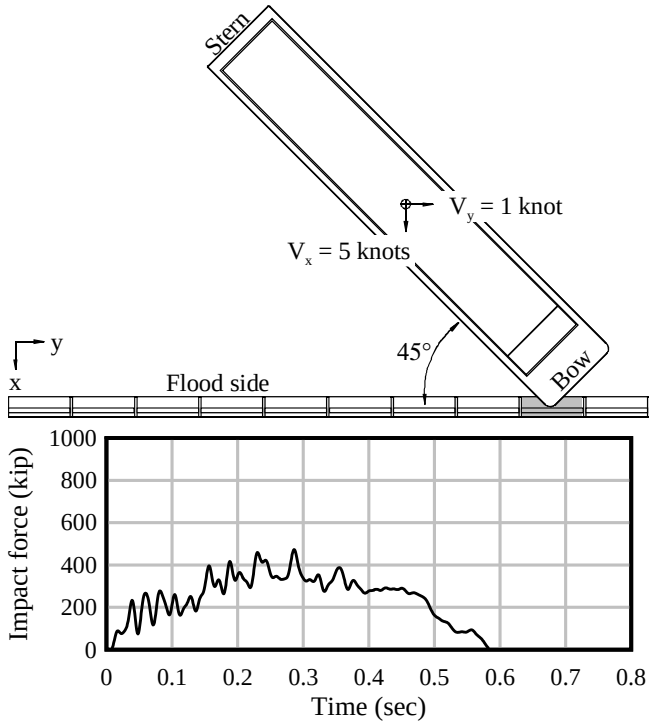

Figure 4.15 Empty barge, bow impact, PRO wall, 45° angle, x-direction force-history

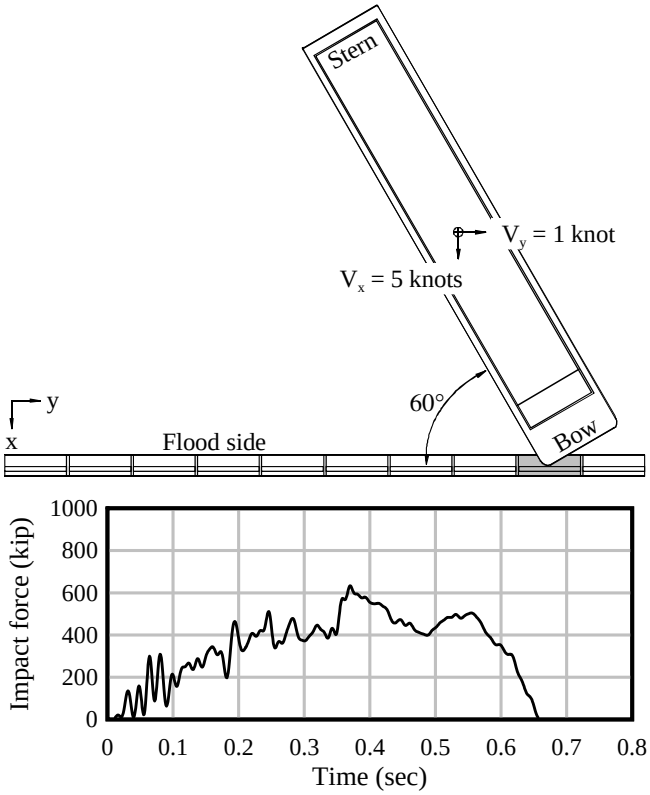

Figure 4.16 Empty barge, bow impact, PRO wall, 60° angle, x-direction force-history

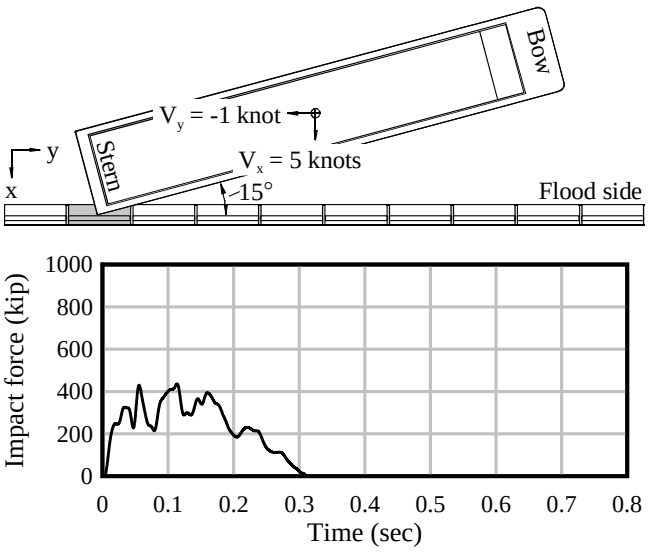

Figure 4.17 Empty barge, stern impact, PRO wall, 15° angle, x-direction force-history

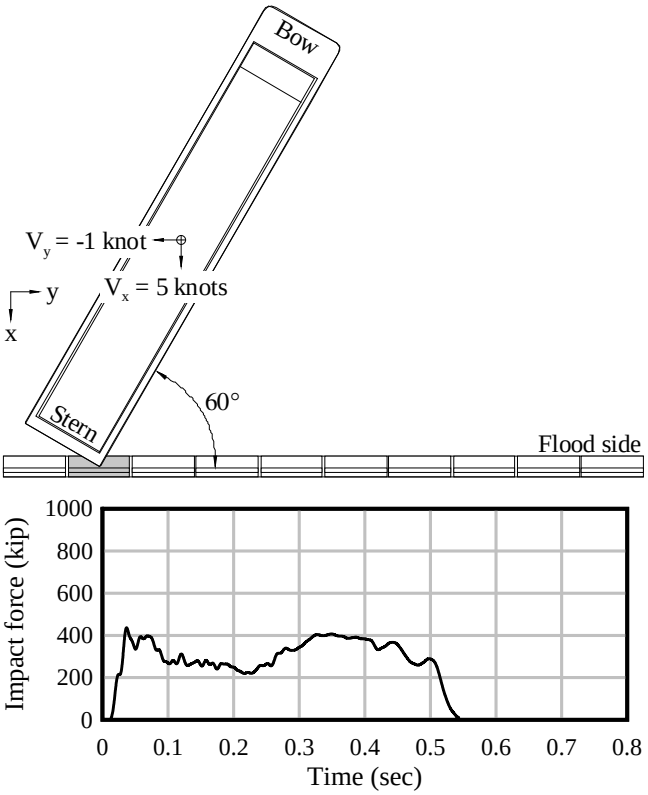

Figure 4.18 Empty barge, stern impact, PRO wall, 60° angle, x-direction force-history

4.4 Baseline Simulation Force-Histories—PRO Dolphin

In this section, force-histories for the baseline simulation set are presented, involving impact with the PRO dolphin protection structure (Figure 4.19). Note that, for these cases, the

barge was consistently positioned such that impact occurs with at least two dolphins at approximately the same time (Figures 4.20 - 4.27). Since multiple PRO dolphin units are impacted during the simulations, the PRO dolphin unit force-history with the greatest magnitude force is plotted using a solid black line. Other dolphin unit force-histories are plotted with colors corresponding to the location within the dolphin group.

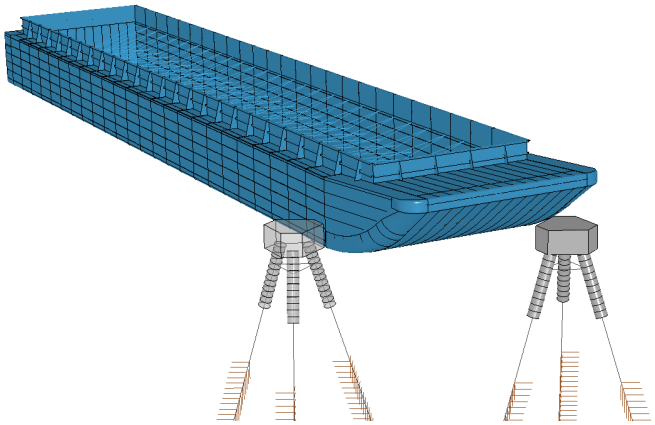

Figure 4.19 Rendering of barge impact simulation with PRO dolphin

The presentation of force-histories and impact schematics in Figures 4.20 - 4.27 is similar to that of the HPO and PRO wall results. However, note that force-histories presented in this section are the resultants of x and y-direction force components. This is because portions of the barge can pass between each dolphin, resulting in significant y-direction forces (when compared to wall impacts). See Appendix C for individual x, y, and z-direction force-histories.

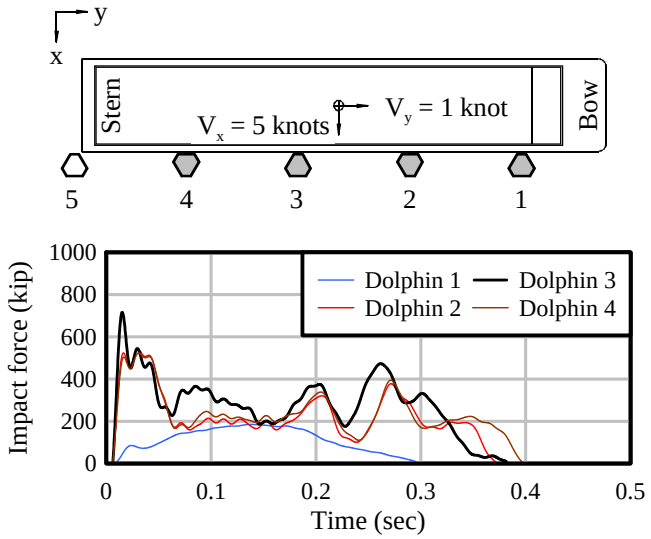

Figure 4.20 Empty barge, sidewall impact, PRO dolphin, 0° angle, resultant force-history

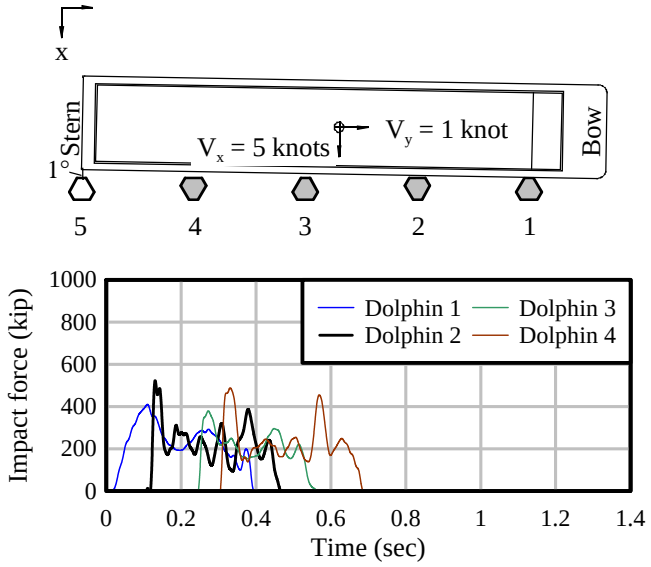

Figure 4.21 Empty barge, bow impact, PRO dolphin, 1° angle, resultant force-history

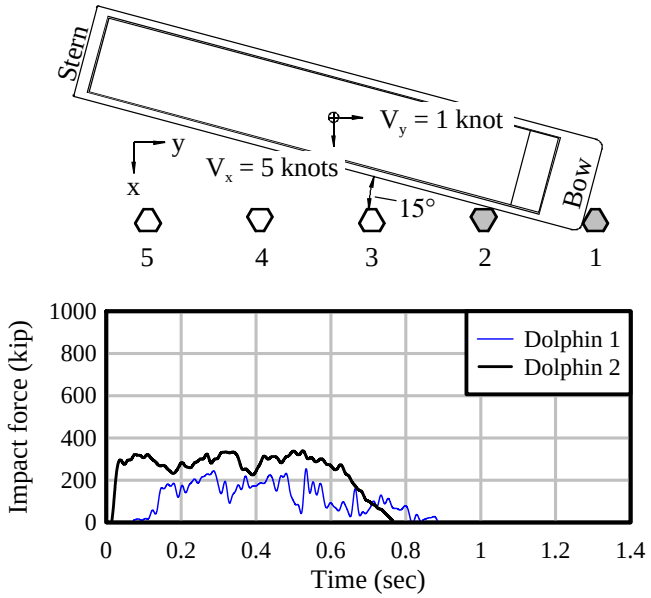

Figure 4.22 Empty barge, bow impact, PRO dolphin, 15° angle, resultant force-history

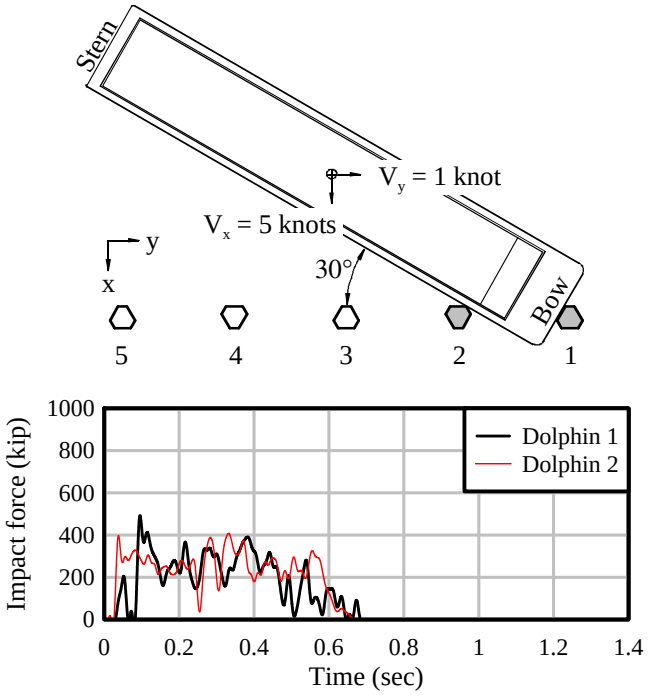

Figure 4.23 Empty barge, bow impact, PRO dolphin, 30° angle, resultant force-history

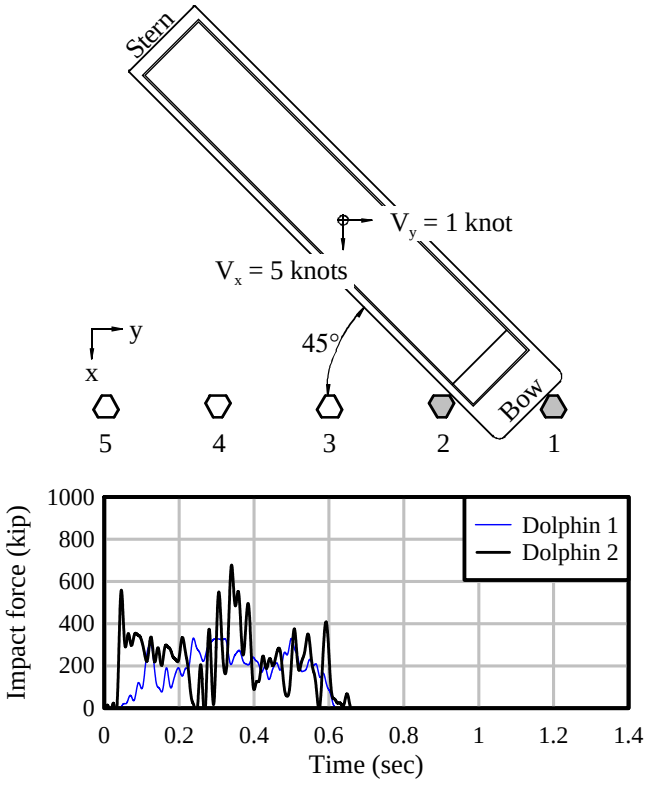

Figure 4.24 Empty barge, bow impact, PRO dolphin, 45° angle, resultant force-history

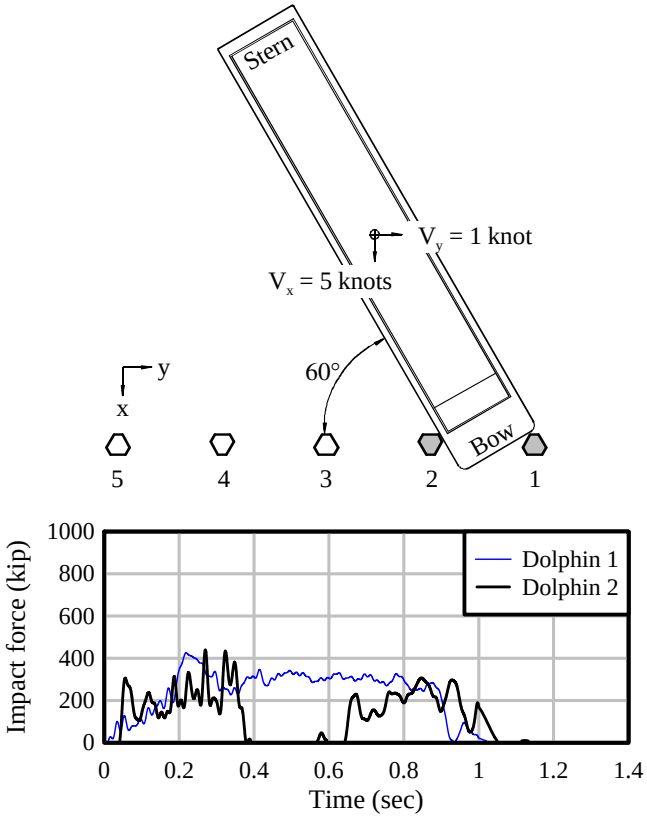

Figure 4.25 Empty barge, bow impact, PRO dolphin, 60° angle, resultant force-history

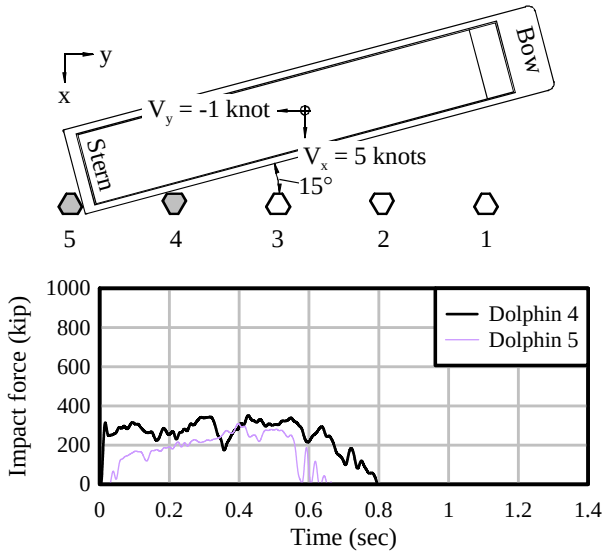

Figure 4.26 Empty barge, stern impact, PRO dolphin, 15° angle, resultant force-history

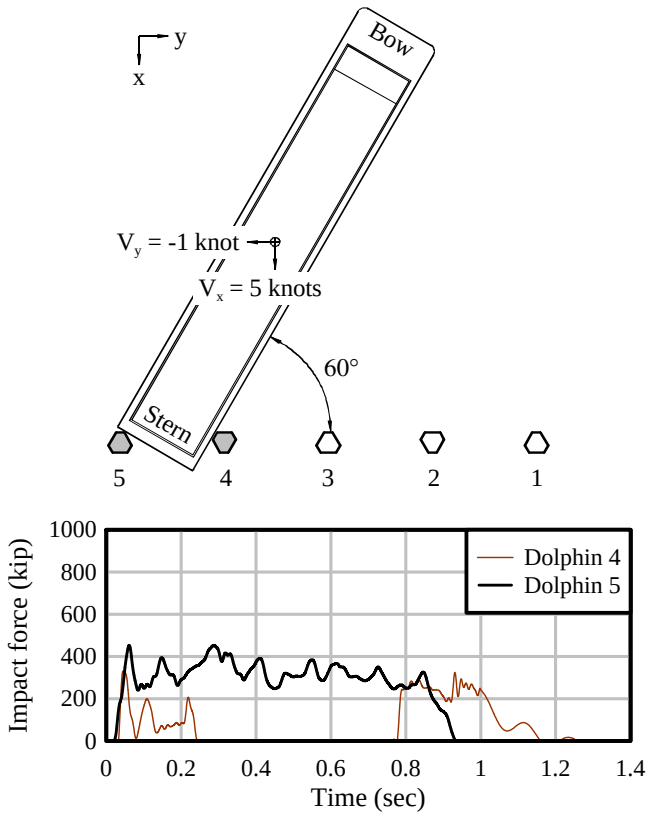

Figure 4.27 Empty barge, stern impact, PRO dolphin, 60° angle, resultant force-history

4.5 Maximum impact forces

As discussed previously, all impact force-histories presented in this report consist of, effectively, raw data. A 100-Hz low-pass filter was used simply to remove high-frequency noise from each force-history. However, significant transient oscillation is still present. Expectedly, the maximum impact force generated during each simulation occurs at the peak of a short-duration spike in load, sometimes as much as 200 kips higher than the overall trend in force.

The impact case shown in Figure 4.28 exemplifies this short-period oscillation. At approximately 0.21 sec, the impact force momentarily jumps from less than 400 kips, to over 600 kips. This spike in impact force is sustained for less than 0.02 sec, substantially less than one fundamental period of the HPO wall structure (approximately 0.15 to 0.20 sec). In this example, the overall maximum force occurs later in time, near 0.5 sec, when substantial oscillation is still present. During this span of time, the impact force momentarily reaches 611 kips, but only for a very short duration.

To quantify impact forces that are appropriate for use with static analysis and design procedures, it could be overly conservative to apply the peak dynamically-obtained load, due to the transient nature of the load. However, it should be noted that inertia-driven sway behavior in the wall could cause dynamic amplification of structural demands, most notably foundation forces. Such effects have been observed in barge impact simulations on bridge structures (Consolazio et al. 2006, Consolazio et al. 2010). If this type of dynamic effect were pronounced during impact with the wall and dolphin structures considered in the present study, static application of the peak dynamic force could potentially be unconservative. A detailed

investigation of dynamic wall behavior—which is beyond the scope of the current study would be necessary to determine whether dynamic amplification effects are significant for wall and dolphin structures.

Under the assumption that such dynamic amplification effects are not significant, it would be overly conservative to statically apply the raw maximum forces. Thus, the force-histories were post-processed using a Gaussian-kernel smoothing algorithm to remove short-duration transient spikes in impact force. A critical consideration when employing a smoothing technique of this type is selecting the range of data—bandwidth of the Gaussian kernel—over which the weighted average is considered. Since the fundamental natural period of both walls was observed to be approximately 0.2 sec, a bandwidth of about one-half the period (0.1 sec) was used in the kernel smoothing algorithm. As illustrated in Figure 4.28, the smoothing algorithm removes short-duration spikes from the load history, leaving only the overall trend of the impact loading event.

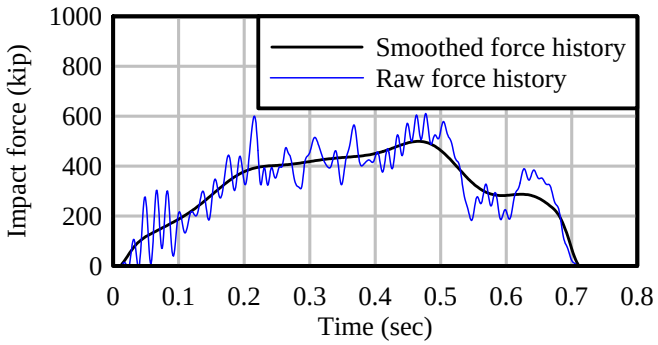

Figure 4.28 Force-history smoothing: Empty barge, bow impact, HPO wall, 60° angle

As expected, maximum forces obtained from the smoothed force-histories are universally lower in magnitude than those obtained from raw data. For the case shown in Figure 4.28, the raw maximum force is 611 kips, while the maximum force after smoothing is 499 kips. Assuming inertial effects do not amplify structural demands on the wall and foundation, the reduced maximum force after smoothing is more appropriate for use in static analysis.

Maximum forces predicted by each of the baseline impact simulations are reported for the HPO wall in Table 4.2, PRO wall in Table 4.3, and the PRO dolphin in Table 4.4. Maximum forces presented in these tables were obtained from force-histories that were processed using the Gaussian kernel smoothing technique cited above. Note that HPO and PRO wall forces reported in Tables 4.2 and 4.3 are x-direction forces (transverse to wall), while PRO dolphin forces (Table 4.4) are resultants of x and y-direction impact forces.

Table 4.2 Maximum forces for HPO wall impacts

Impact condition	Impact angle (°)	Barge weight	Number of engaged monoliths	Max. force per monolith (kip)
Barge side	0	Empty (362 tons)	4	1440
Barge bow	1	Empty (362 tons)	2	625
Barge bow	15	Empty (362 tons)	1	410
Barge bow	30	Empty (362 tons)	1	397
Barge bow	45	Empty (362 tons)	1	389
Barge bow	60	Empty (362 tons)	1	499
Barge stern	15	Empty (362 tons)	1	318
Barge stern	60	Empty (362 tons)	1	448

Table 4.3 Maximum forces for PRO wall impacts

Impact condition	Impact angle (°)	Barge weight	Number of engaged monoliths	Max. force per monolith (kip)
Barge side	0	Empty (362 tons)	8	722
Barge bow	1	Empty (362 tons)	2	609
Barge bow	15	Empty (362 tons)	1	436
Barge bow	30	Empty (362 tons)	1	379
Barge bow	45	Empty (362 tons)	1	367
Barge bow	60	Empty (362 tons)	1	529
Barge stern	15	Empty (362 tons)	1	307
Barge stern	60	Empty (362 tons)	1	360

Table 4.4 Maximum forces for PRO dolphin impacts

Impact condition	Impact angle (°)	Barge weight	Number of engaged dolphins	Max. force per dolphin (kip)
Barge side	0	Empty (362 tons)	4	435
Barge bow	1	Empty (362 tons)	2	318
Barge bow	15	Empty (362 tons)	1	314
Barge bow	30	Empty (362 tons)	1	307
Barge bow	45	Empty (362 tons)	1	368
Barge bow	60	Empty (362 tons)	1	354
Barge stern	15	Empty (362 tons)	1	315
Barge stern	60	Empty (362 tons)	1	396

As shown in Table 4.2, maximum impact forces for the HPO wall ranged from approximately 300 to 500 kips for all oblique impact scenarios (angles 15° and greater), with an average of 410 kips. Forces generated during oblique impact with the PRO wall (Table 4.3) were similar, ranging from approximately 300 to 530 kips, and averaging 400 kips. Oblique impact forces for the PRO dolphin protective structure were slightly lower (Table 4.4), ranging from 300 to 400 kips, and averaging approximately 340 kips.

Forces generated during side-on (0°), and nearly side-on (1°) collisions are generally higher than the oblique impact conditions. This difference is especially pronounced in the HPO wall, where the maximum force (per wall monolith) is almost three times the largest oblique impact force. For this wall, the 1° collision force (625 kips), is 25% larger than the most severe oblique force. The increase in loads for side-on impact conditions is less severe for the PRO wall and PRO dolphin.

Several reasons exist for assigning reduced importance to side-on impact forces. Foremost is the duration of the impact event, especially for 0° cases. For 0° impact with either wall structure, the duration of the collision event is less than one natural period of the structure. It is likely that such large loads develop, in large part, from inertial resistance provided by the mass of the wall. Secondly, the probability of a barge impact occurring at an angle of 1° or less is likely very small. Unfortunately, insufficient data are available to quantitatively assess the probability of occurrence of 0° or 1° impacts. Lastly, impact velocities (transverse to the wall) for 0° or 1° impacts are likely to be less than the 5 knots used in this study. During a side impact, a large volume of water must be displaced between the barge and wall, which can slow the barge immediately prior to impact. This would imply that the forces predicted by 5-knot side-on simulations might be overly conservative [the influence of initial velocity on impact forces is discussed below].

4.6 Sensitivity of Impact Forces to Selected Model Parameters

Approximately 30 additional simulations were conducted to assess the sensitivity of barge impact forces to a variety of different model parameters. Each sensitivity study includes one or more additional simulations under varied conditions, which can then be directly compared to a corresponding baseline simulation set.

4.6.1 Barge payload—fully loaded impacts

For all baseline simulations, the barge was empty with a small residual payload (362 tons). In the empty configuration, impact velocities were 5 knots transverse to the wall (or line of dolphins), and 1 knot longitudinally. However, fully loaded barges may also impact hurricane protection systems, but with potentially greater kinetic energy. Thus, ten additional simulations were conducted using a fully loaded barge—five with the HPO wall, and five with the PRO dolphin. When loaded, the barge and payload total 1645 tons. The impact velocity transverse to the wall was reduced to 4 knots, and the longitudinal velocity remained 1 knot. At these impact velocities, the fully loaded barge possesses approximately 3.5 times as much momentum and 3.0 times as much kinetic energy as an empty barge. Impact force-histories for the fully loaded impact cases are presented in Figures 4.29 - 4.38.

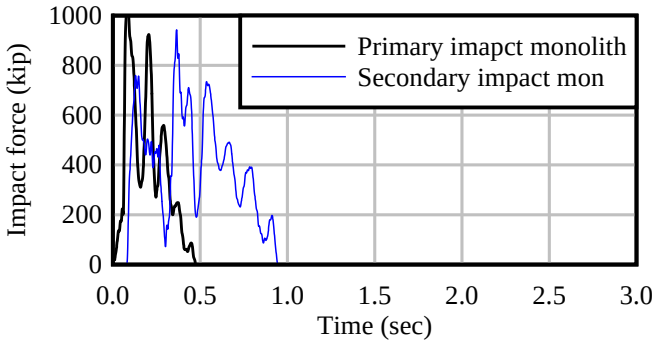

Figure 4.29 Fully-loaded barge, bow impact, HPO wall, 1° angle

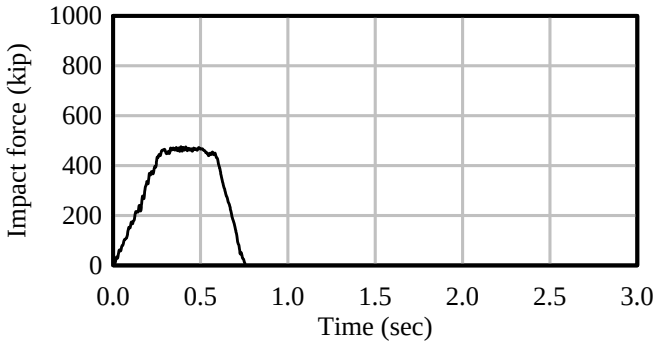

Figure 4.30 Fully-loaded barge, bow impact, HPO wall, 15° angle

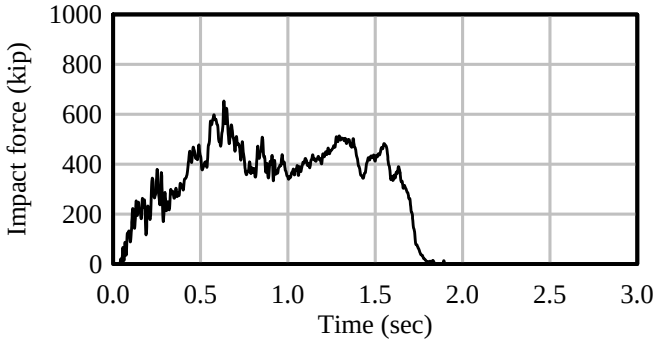

Figure 4.31 Fully-loaded barge, bow impact, HPO wall, 60° angle

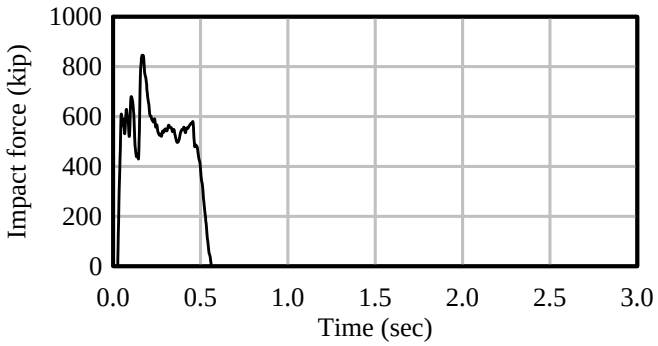

Figure 4.32 Fully-loaded barge, stern impact, HPO wall, 15° angle

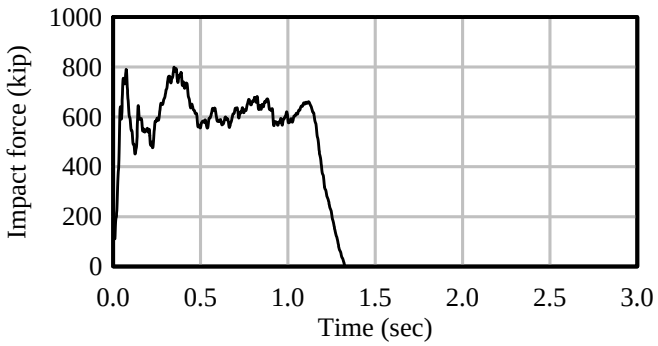

Figure 4.33 Fully-loaded barge, stern impact, HPO wall, 60° angle

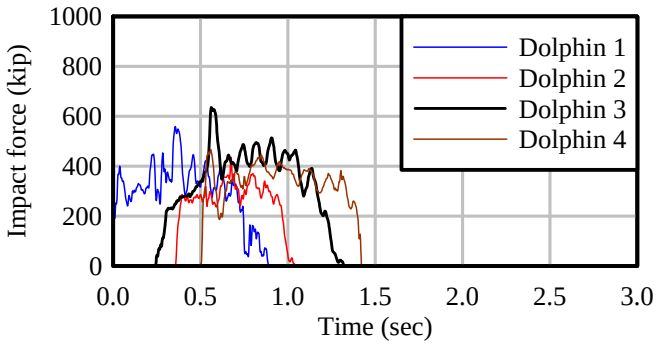

Figure 4.34 Fully-loaded barge, bow impact, PRO dolphin, 1° angle

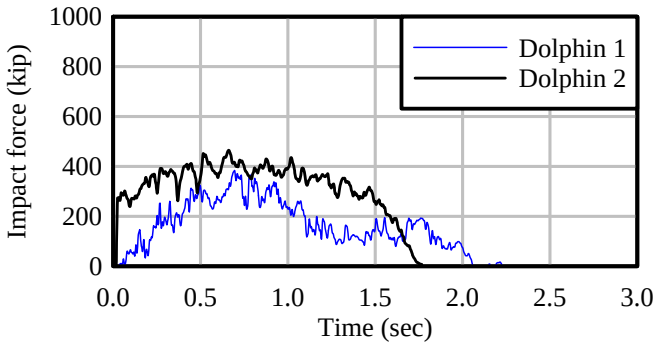

Figure 4.35 Fully-loaded barge, bow impact, PRO dolphin, 15° angle

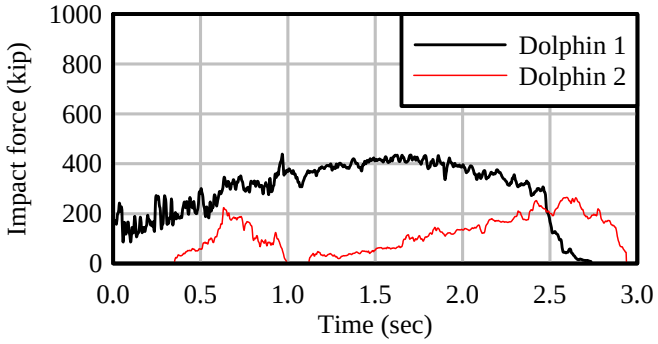

Figure 4.36 Fully-loaded barge, bow impact, PRO dolphin, 60° angle

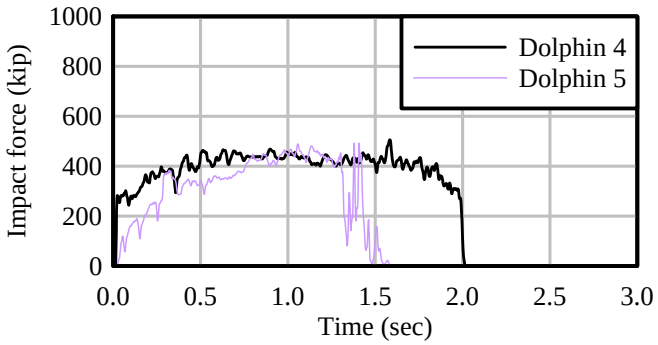

Figure 4.37 Fully-loaded barge, stern impact, PRO dolphin, 15° angle

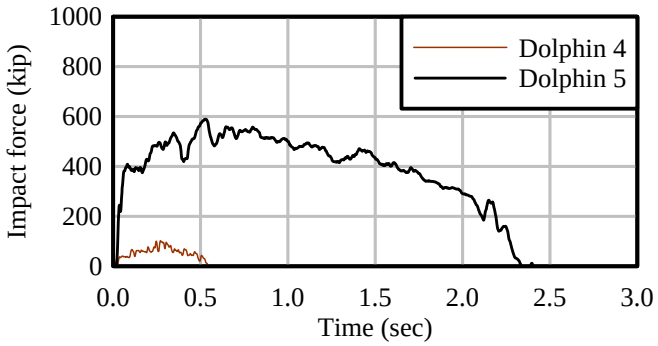

Figure 4.38 Fully-loaded barge, stern impact, PRO dolphin, 60° angle

Figures 4.29 - 4.38 indicate that fully loaded barge impacts generate both larger forces and longer impact durations than corresponding empty barge impacts (recall Sections 4.2 and 4.4). Maximum impact forces (Table 4.5) are universally higher than those generated by an empty barge. For bow impacts with the HPO wall, differences between empty and loaded impact forces are relatively small, at 7 - 14%. This finding implies that the barge bow has reached an effective plastic load, at which additional impact energy (and crushing depth) cannot generate substantially higher forces. In contrast, for stern impacts with the HPO wall, the fully loaded barge causes significantly larger impact forces—as much as two times larger. This suggests that the barge stern has additional crushing capacity for energies larger than those associated with the empty condition. Thus, with a fully loaded barge, the 60° stern impact case controls at approximately 750 kips.

For impacts with the PRO dolphin, fully loaded impact forces were universally higher—by approximately 20 - 60%. However, no significant discrepancy exists between increases associated with bow and stern impacts. Again, the 60° stern impact case controls at approximately 550 kips.

Table 4.5 Maximum forces for empty and loaded barge impacts

Impact condition	Impact angle	Impacted structure	Velocity empty barge	Max. force empty barge	Velocity loaded barge	Max. force loaded barge	Percent difference
			(knot)	(kip)	(knot)	(kip)	
Barge bow	1°	HPO wall	5	625	4	669	7.0%
Barge bow	15°	HPO wall	5	410	4	466	13.7%
Barge bow	60°	HPO wall	5	499	4	545	9.2%
Barge stern	15°	HPO wall	5	318	4	664	108.8%
Barge stern	60°	HPO wall	5	448	4	749	67.2%
Barge bow	1°	PRO dolphin	5	318	4	498	56.6%
Barge bow	15°	PRO dolphin	5	314	4	424	35.0%
Barge bow	60°	PRO dolphin	5	354	4	421	18.9%
Barge stern	15°	PRO dolphin	5	315	4	455	44.4%
Barge stern	60°	PRO dolphin	5	396	4	553	39.6%

4.6.2 Barge initial velocity—side-on impacts

As previously noted, during side-on and nearly side-on impacts (angles 1° or less), water between the barge and wall must be displaced very rapidly. It has been observed that this phenomenon slows the barge immediately prior to impact. Thus, even if the barge is propelled by wind at approximately 5 knots (or 4 knots for a loaded barge), realistic impact velocities for side-on cases may be much lower. Consequently, two additional 1° simulations were conducted with the HPO wall—one with an empty barge, and one with a fully loaded barge—with impact occurring at half the velocity used for more oblique impacts. Force-histories for these half-speed cases are compared to the corresponding full-speed histories in Figures 4.39 - 4.40. Note that barge impacts at 1° engage two wall monoliths. However, forces on the secondary monolith are consistently smaller. Therefore only the forces for the primary impact monolith are shown for clarity.

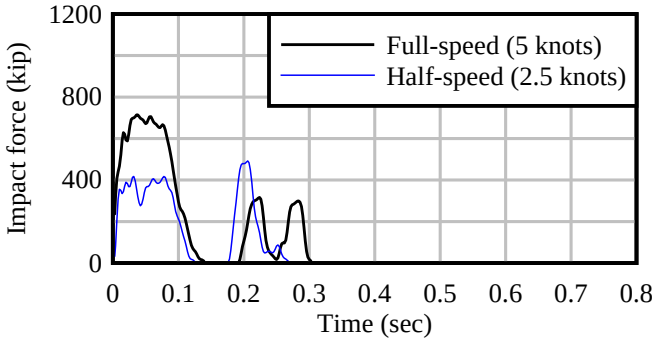

Figure 4.39 Force-history comparison: Empty barge, bow impact, HPO wall, 1° angle (only primary impact monolith shown)

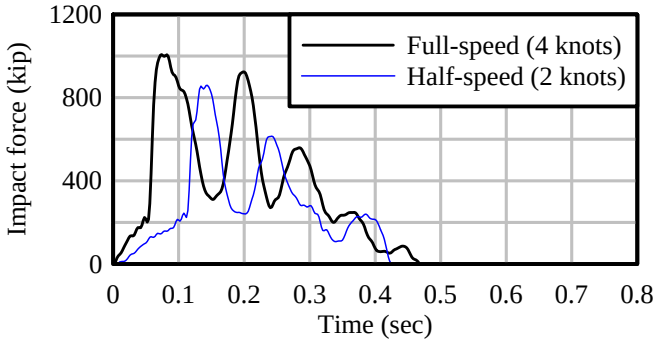

Figure 4.40 Force-history comparison: Loaded barge, bow impact, HPO wall, 1° angle (only primary impact monolith shown)

Reducing the impact velocity by 50% had the effect of reducing load magnitudes and, to a lesser extent, impact durations (Figures 4.39 - 4.40). In contrast, filtered maximum impact forces developed at half-speed (Table 4.6) were significantly smaller. Thus, if the cushioning effect observed during nearly side-on barge impacts slows the barge by 50%, it would be reasonable to neglect the 0° and 1° impact forces presented in Section 4.5, since this impact condition would not control design forces.

Table 4.6 Maximum forces for full-speed and half-speed 1° impacts

Impact condition	Impact angle (°)	Barge weight	Impacted wall structure	Max. force full-speed (kip)	Max. force half-speed (kip)	Percent difference
Barge bow	1	Empty (362 tons)	HPO	625	342	-45.3%
Barge bow	1	Loaded (1645 tons)	HPO	669	505	-24.5%

4.6.3 Barge initial kinetic energy—oblique impacts

Additional 60° bow impact simulations on the HPO wall were conducted to investigate the influence of initial barge kinetic energy on resulting impact forces (Figure 4.41). Using an empty barge, the velocity component perpendicular to the wall (V_x) was set to 3, 4, 5, and 6 knots, while the longitudinal component (V_y) was held constant at 1 knot. Additionally, one fully-loaded simulation was constructed with V_x equal to 4 knots. The resulting impact load histories are shown in Figures 4.42 - 4.46.

As shown in Figures 4.42 - 4.46, both impact load and load duration increased with increasing initial barge kinetic energy and momentum. Maximum impact loads are summarized in Table 4.7 and are compared to velocity and kinetic energy in Figure 4.47. For the cases considered, maximum forces increased with both momentum and energy, but not without limit. The loaded (4-knot) impact case had significantly more initial momentum and energy than any empty barge case. However, this did not result in a larger maximum impact force. Only the load duration was affected by the increase in momentum and energy. Thus, it appears that with momentum larger than approximately 300 kip-sec, or energy higher than 1200 kip-ft, impact forces have reached a limiting value of about 550 kips.

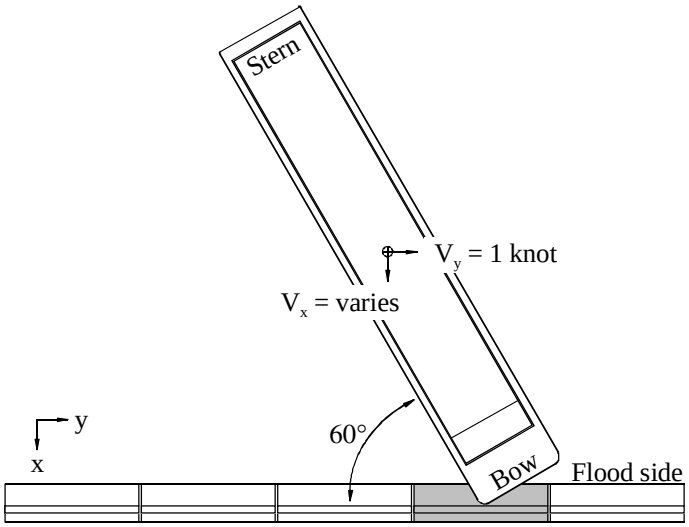

Figure 4.41. Impact conditions—HPO wall

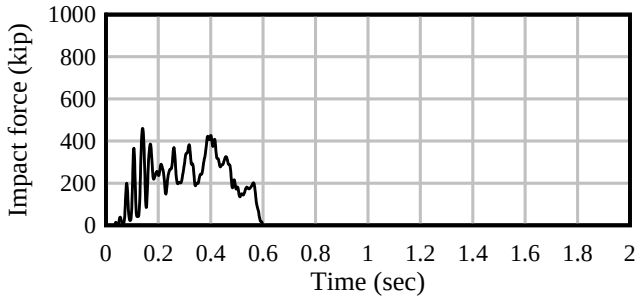

Figure 4.42 Empty barge, bow impact, HPO wall, 60° angle, initial V_x=3 knots

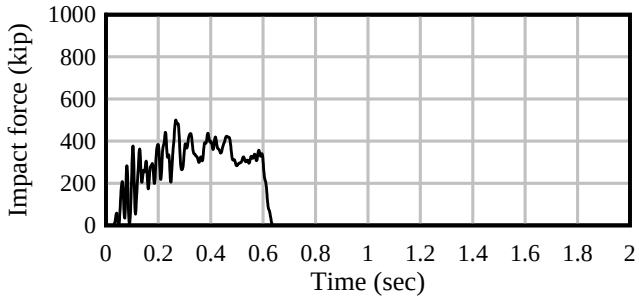

Figure 4.43 Empty barge, bow impact, HPO wall, 60° angle, initial V_x=4 knots

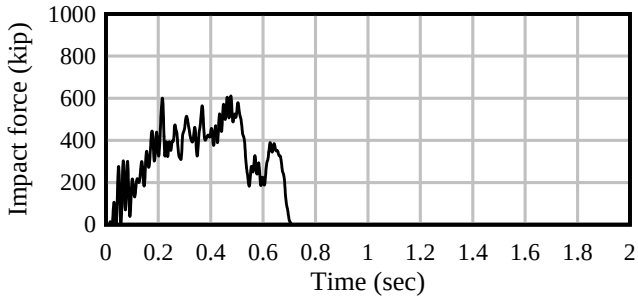

Figure 4.44 Empty barge, bow impact, HPO wall, 60° angle, initial V_x=5 knots

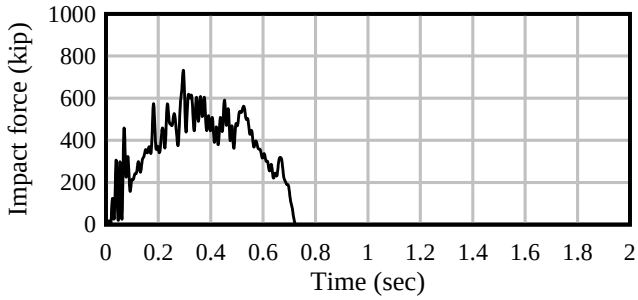

Figure 4.45 Empty barge, bow impact, HPO wall, 60° angle, initial V_x=6 knots

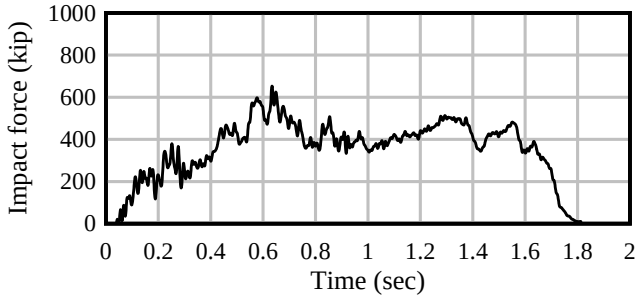

Figure 4.46 Loaded barge, bow impact, HPO wall, 60° angle, initial V_x=4 knots

Table 4.7 Maximum forces for various impact energies

Impact condition	Impact angle	Barge weight	Impacted structure	Initial velocity	Initial momentum	Kinetic energy	Max. impact force
	(°)			(knot)	(kip-sec)	(kip-ft)	(kip)
Barge bow	60	Empty (362 tons)	HPO	3	114	288	329
Barge bow	60	Empty (362 tons)	HPO	4	152	513	378
Barge bow	60	Empty (362 tons)	HPO	5	190	801	499
Barge bow	60	Empty (362 tons)	HPO	6	278	1150	547
Barge bow	60	Loaded (1645 tons)	HPO	4	690	2330	545

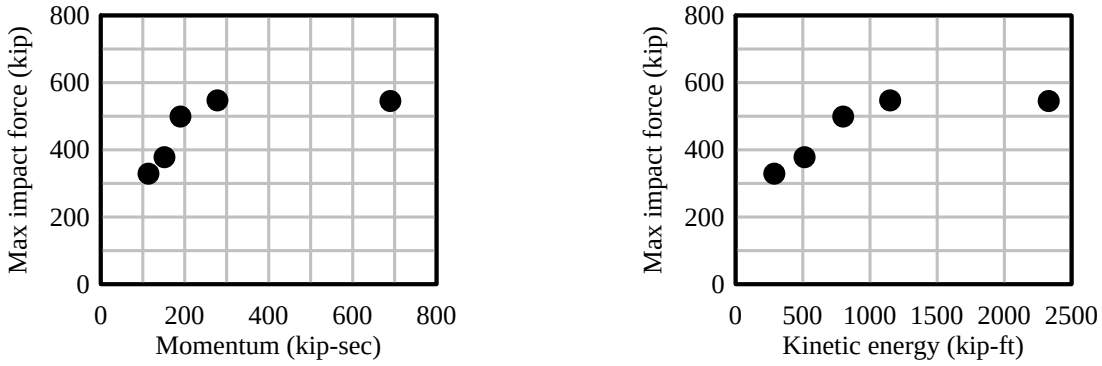

a) b)

Figure 4.47 Maximum impact force as a function of:
a) Initial impact velocity, and b) Initial kinetic energy

4.6.4 Barge position with respect to wall monoliths

Throughout this study, the barge has consistently been positioned such that initial contact occurs at the center of the active wall monolith (Figure 4.48a). It was reasoned that this location should be the stiffest region along the length of each wall monolith. Thus, impact forces generated during impact with this stiffer region should be conservative when compared to those generated from other potential barge positions.

To assess this assumption, one additional simulation was conducted, placing the initial contact point much closer to the edge of the active monolith. The simulation consists of an empty barge impacting the HPO wall at 60°. The barge was positioned such that initial contact occurs 5 ft from the end of the active monolith (Figure 4.48b).

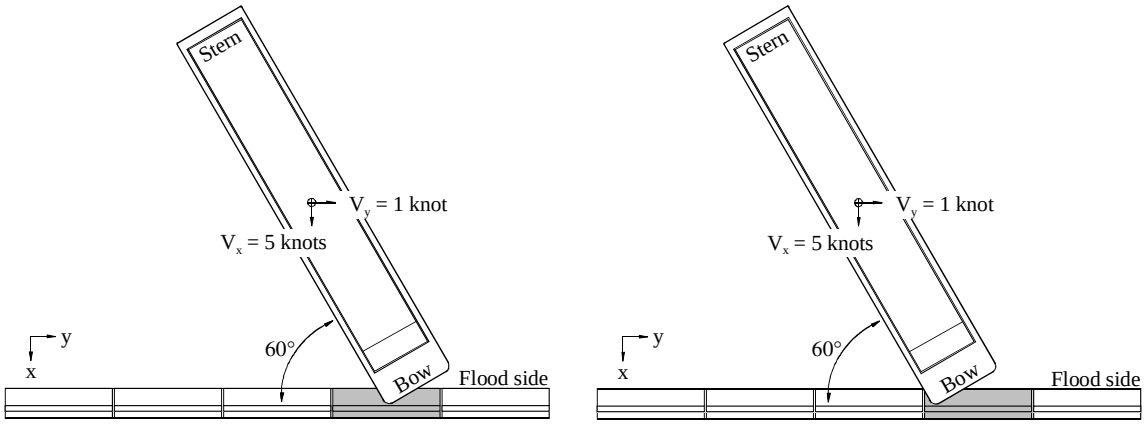

a) b)

Figure 4.48 Empty barge, bow impact, HPO wall, 60° angle with impact point positioned at:
a) Center of impact monolith, and b) 5 ft from end of monolith

Because the only change between the simulations shown in Figures 4.48a and 4.48b is the location of initial contact, force-histories obtained for the two simulations are directly

comparable. As illustrated in Figure 4.49 and Table 4.8, the impact forces generated at the center and near the edge are very similar, differing by only about 12%.

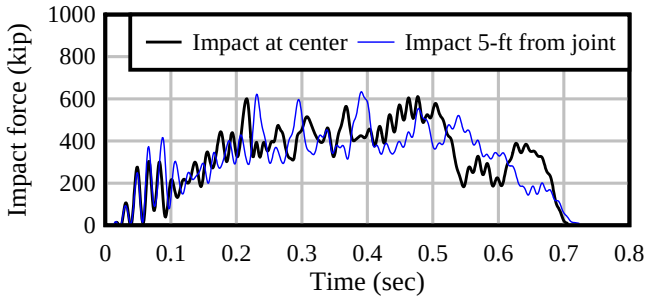

Figure 4.49 Sensitivity of impact point location—impact force-history

Table 4.8 Maximum forces for monolith-center and near-joint impact

Impact condition	Impact angle	Barge weight	Impacted wall structure	Max. force at center	Max. force near joint	Percent difference
	(°)			(kip)	(kip)	
Barge bow	60	Empty (362 tons)	HPO	499	437	-12.4%

4.6.5 Barge position with respect to PRO dolphins

As discussed previously (Section 4.4), for a given impact angle, barge impact on a line of dolphins can occur at an indeterminate number of different positions. For example, at large oblique angles, impact may involve one or two dolphin structures. Furthermore, if impact with two dolphins occurs, the barge may engage both simultaneously, or strike one before the other. Additionally, the dolphin configuration considered in this study utilizes an alternating dolphin orientation along the line, with every other dolphin reversed 180° relative to adjacent dolphins. Given that dolphin structures are likely to have differing stiffness and strength characteristics, depending on the direction of impact, four additional simulations (60° angle bow impact, and 60° stern impact) were conducted to assess how the initial barge position influences impact forces.

The baseline orientation (Figures 4.50 and 4.53) consists of positioning the barge such that impact occurs with two dolphins approximately simultaneously. For a given impact angle and impact velocity, there exists only one unique position such that this occurs. For the baseline cases, the dolphin directly in front of the barge is oriented with the “pointed” face (of the dolphin pile cap) oriented toward the waterway. The “reversed” orientation (Figures 4.51 and 4.54) also involves simultaneous engagement of two dolphins, but the dolphin directly in front of the barge has the wider, flat surface facing the waterway. Lastly, in the “centered” configuration (Figures 4.52 and 4.55), impact occurs with one dolphin only, and the engaged dolphin is centered along the bow or stern width.

Maximum impact forces predicted for each orientation considered are summarized in Table 4.9. In the interest of developing a consistent orientation for all barge angles, only the baseline and reversed orientations are pertinent. It is noted that the centered orientation is not possible at oblique angles smaller than 45° due to interference with other dolphins. Because impact forces generated using the baseline and reversed orientations varied by only 2 - 8%, impact force does not appear sensitive to the choice of dolphin orientation. Consequently, the baseline orientation was selected for all other barge impact simulations on the PRO dolphin.

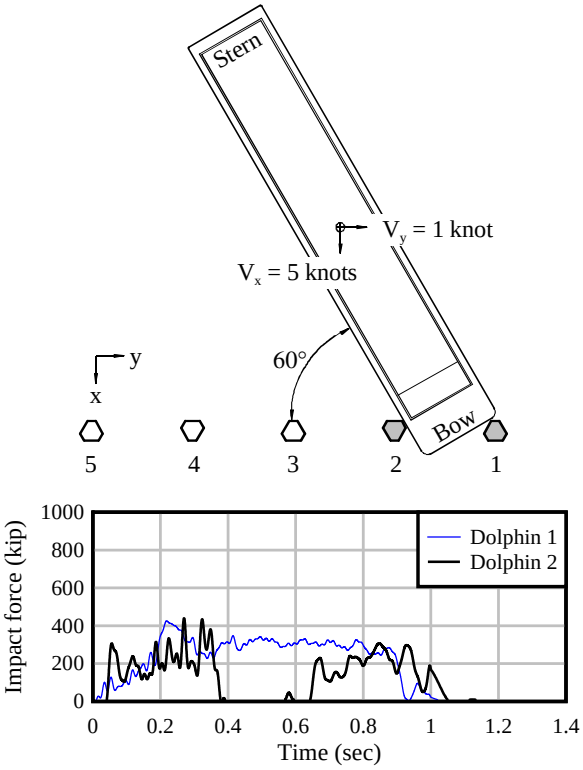

Figure 4.50 Empty barge, bow impact, PRO dolphin, 60° angle, baseline dolphin orientation

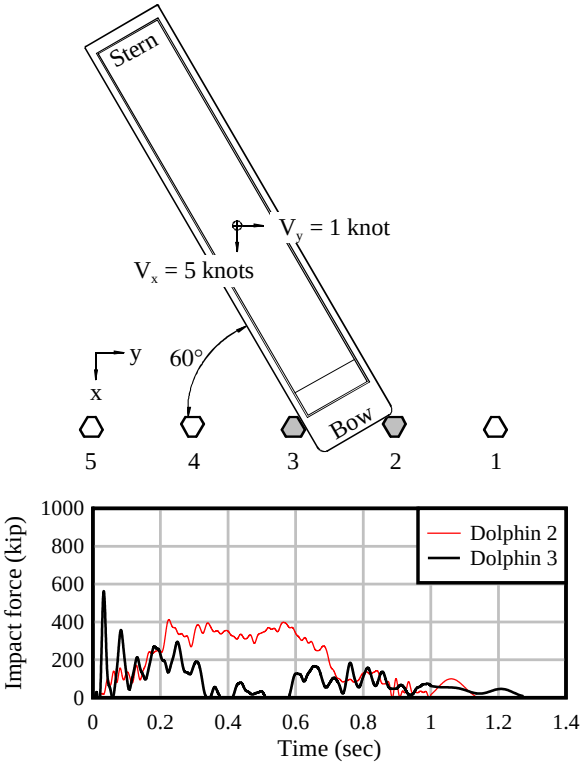

Figure 4.51 Empty barge, bow impact, PRO dolphin, 60° angle, reversed dolphin orientation

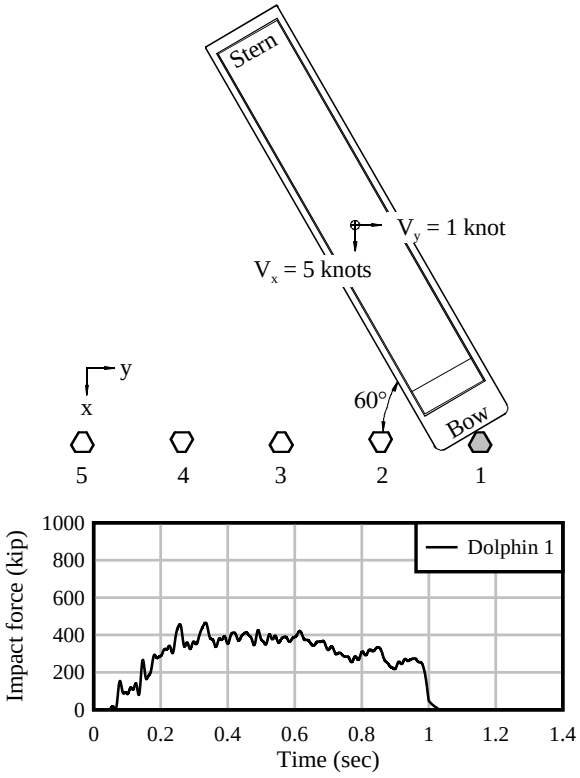

Figure 4.52 Empty barge, bow impact, PRO dolphin, 60° angle, centered on dolphin

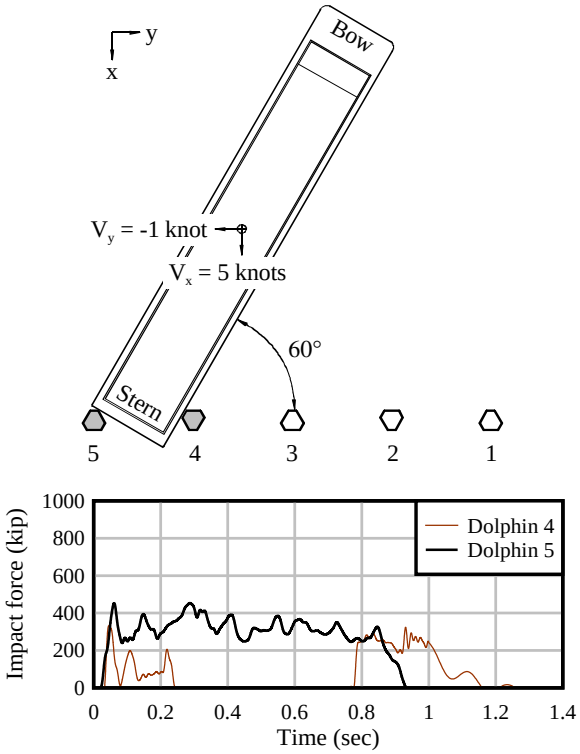

Figure 4.53 Empty barge, stern impact, PRO dolphin, 60° angle, baseline dolphin orientation

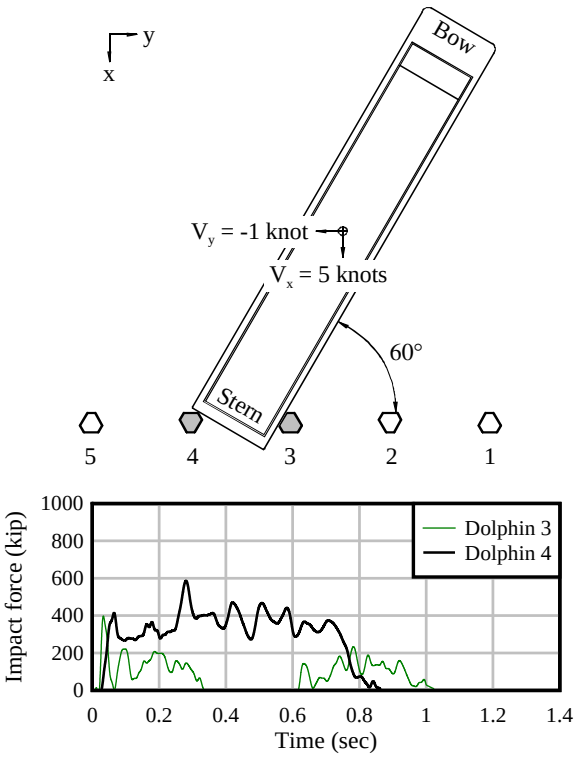

Figure 4.54 Empty barge, stern impact, PRO dolphin, 60° angle, reversed dolphin orientation

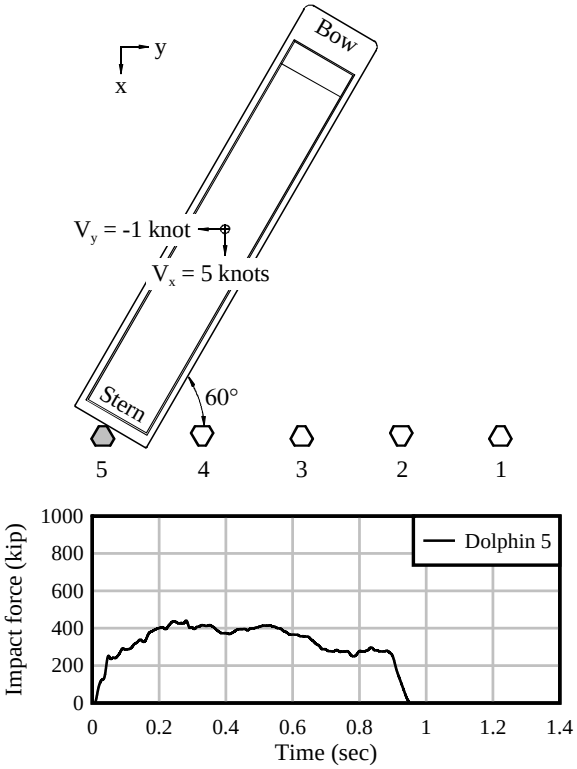

Figure 4.55 Empty barge, stern impact, PRO dolphin, 60° angle, centered on dolphin

Table 4.9 Maximum forces for PRO dolphin impacts in various orientations

Impact condition	Impact angle (°)	Barge weight	Barge/dolphin orientation	Number of engaged dolphins	Max. force per dolphin (kip)
Barge bow	60	Empty (362 tons)	Baseline	2	354
Barge bow	60	Empty (362 tons)	Reversed	2	361
Barge bow	60	Empty (362 tons)	Centered	1	389
Barge stern	60	Empty (362 tons)	Baseline	2	396
Barge stern	60	Empty (362 tons)	Reversed	2	430
Barge stern	60	Empty (362 tons)	Centered	1	418

4.6.6 Wall-pile connection

For all barge impact scenarios presented thus far in this report, the connections between the piles and the wall footing are assumed to be fixed such that the pile head cannot rotate relative to the footing. Given that a fixed pile head condition provides additional stiffness to the impacted structure (relative to one with pinned-head piles), conservative estimates of impact forces should result for the fixed head condition.

However, as documented in construction drawings, the specified pile embedment—9 in. for the HPO wall, 12 in. for the PRO wall, and 18 in. for the PRO dolphin—is likely insufficient to develop the full pile moment capacity. Consequently, four additional simulations were conducted with pinned pile head connections to assess the assumption that modeling these connections as fixed is conservative with respect to prediction of impact forces. Specifically, 60° bow and stern impacts were considered, with both the HPO and PRO wall structures. The resulting force-histories are compared to those obtained from identical simulations with fixed pile head connections (Figures 4.56 - 4.59).

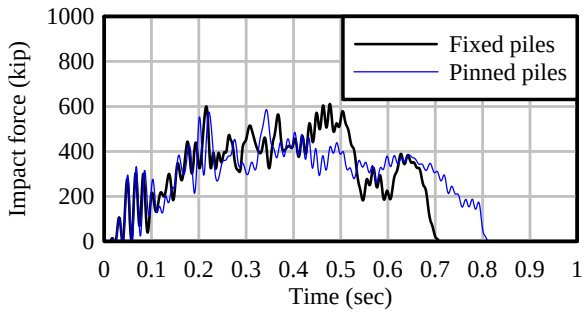

Figure 4.56 Force-history comparison: Empty barge, bow impact, HPO wall, 60° angle

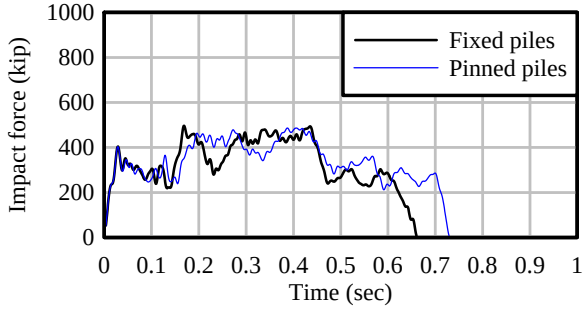

Figure 4.57 Force-history comparison: Empty barge, stern impact, HPO wall, 60° angle

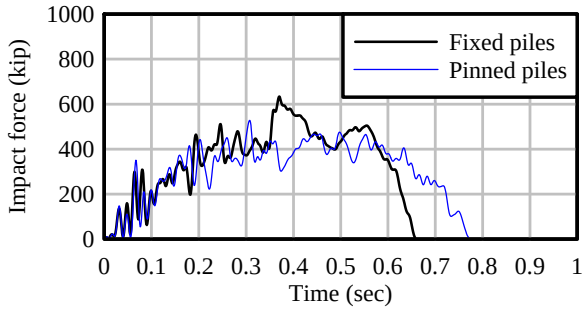

Figure 4.58 Force-history comparison: Empty barge, bow impact, PRO wall, 60° angle

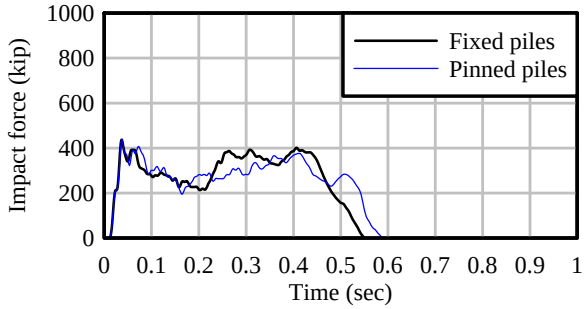

Figure 4.59 Force-history comparison: Empty barge, stern impact, PRO wall, 60° angle

As illustrated in Figures 4.56 - 4.59, impact durations are longer for walls with pinned piles, as expected, given that increased flexibility results from pinning the piles. Additionally, maximum forces generated using pinned piles are smaller in magnitude than with fixed piles. Thus, the maximum forces summarized in Table 4.10 imply that the baseline simulation forces—generated using fixed pile heads—are, in fact, conservative.

Table 4.10 Maximum forces for fixed and pinned pile heads

Impact condition	Impact angle	Barge weight	Impacted wall structure	Max. force fixed piles (kip)	Max. force pinned piles (kip)	Percent difference
Barge bow	60°	Empty (362 tons)	HPO	499	427	-14.4%
Barge stern	60°	Empty (362 tons)	HPO	448	444	-0.9%
Barge bow	60°	Empty (362 tons)	PRO	529	425	-19.7%
Barge stern	60°	Empty (362 tons)	PRO	360	341	-5.6%

4.6.7 Soil strength and stiffness

As discussed previously, soil-structure interaction was modeled by means of distributed nonlinear discrete spring elements along the embedded length of pile elements. Lateral soil resistance (P-x, and P-y), skin friction (τ-z), and tip resistance (Q-z) were all considered. A force-deformation relationship for each soil spring was developed based on readily available correlations to either SPT or CPT profiles. While a deterministic treatment of soil resistance (stiffness and strength) are necessary for numerical modeling, realistically, significant variability is present. Potential sources of uncertainty include in-situ spatial variability and variability in empirical soil parameter correlations. While the soil-structure interaction modeling techniques

employed in this study have been validated against both reduced-scale and full-scale experiments, uncertainty associated with modeling soil behavior should still be considered. Consequently, a series of additional simulations were conducted to assess the sensitivity of barge impact loads to variation in soil resistance.

In experimental studies of barge impact with bridge piers, it was observed that cohesive soil resistance can increase by as much as 100% under such rapid loading conditions (McVay et al. 2005, Consolazio et al. 2006). Accordingly, as an upper-bound assessment, the soil strength and stiffness were doubled. Specifically, all ordinate values of load-displacement curves that define soil resistance were doubled (Figure 4.60).

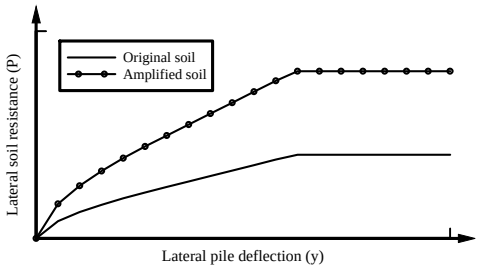

Figure 4.60 Amplified soil strength and stiffness (example P-y curve shown)

To assess the influence of soil resistance on the barge impact loads, six additional impact simulations were conducted with amplified soil resistance—three on the HPO wall, and three on the PRO wall. Impact forces from these simulations are compared to corresponding baseline simulations (using the original soil resistance) in Figures 4.61 - 4.66.

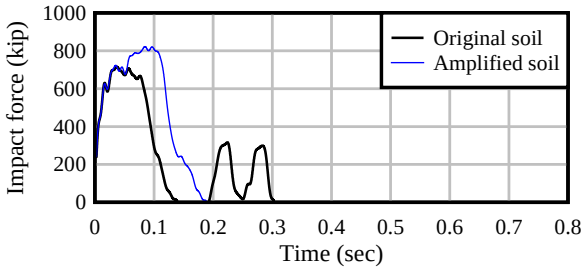

Figure 4.61 Force-history comparison: Empty barge, bow impact, HPO wall, 1° angle (only primary impact monolith shown)

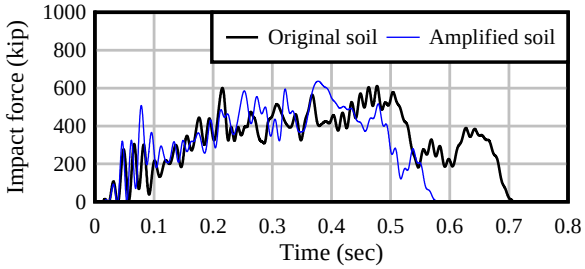

Figure 4.62 Force-history comparison: Empty barge, bow impact, HPO wall, 60° angle

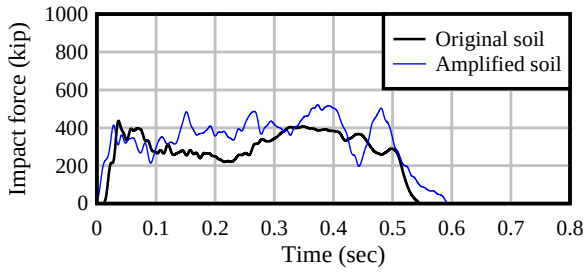

Figure 4.63 Force-history comparison: Empty barge, stern impact, HPO wall, 60° angle

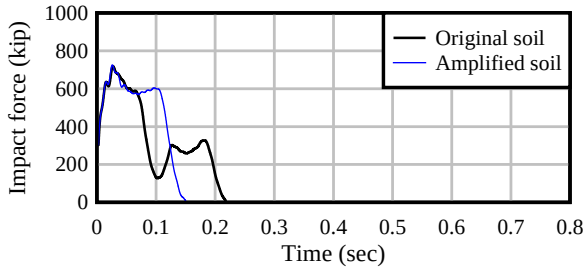

Figure 4.64 Force-history comparison: Empty barge, bow impact, PRO wall, 1° angle (only primary impact monolith shown)

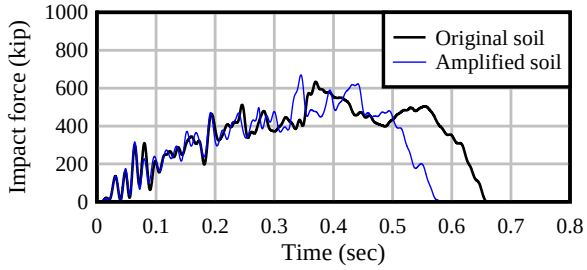

Figure 4.65 Force-history comparison: Empty barge, bow impact, PRO wall, 60° angle

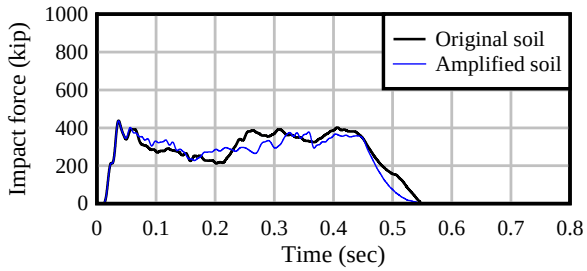

Figure 4.66 Force-history comparison: Empty barge, stern impact, PRO wall, 60° angle

In general, maximum impact forces were not very sensitive to the substantial increase in soil resistance that was introduced (Table 4.11). For most impact conditions, the peak force changed only nominally. However, an approximate 12% increase in peak force was observed for the 1° bow impact case with the HPO wall (Figure 4.61).

While peak forces remained effectively the same, the increase in stiffness of the wall/soil system resulted in reduced impact durations. Thus, a smaller proportion of the barge kinetic energy is absorbed by the wall/soil structure when the soil resistance is amplified. Furthermore, this increase in wall/soil system stiffness resulted in smaller wall displacements during impact. For the purpose of assessing peak impact forces, however, substantial variation in soil resistance appears to be not of primary concern.

Table 4.11 Maximum forces for original and amplified soil model

Impact condition	Impact angle (°)	Barge weight	Impacted wall structure	Max. force original soil (kip)	Max. force amplified soil (kip)	Percent difference
Barge bow	1	Empty (362 tons)	HPO	625	701	12.2%
Barge bow	60	Empty (362 tons)	HPO	499	516	3.4%
Barge stern	60	Empty (362 tons)	HPO	448	449	0.2%
Barge bow	1	Empty (362 tons)	PRO	609	608	-0.2%
Barge bow	60	Empty (362 tons)	PRO	529	527	-0.4%
Barge stern	60	Empty (362 tons)	PRO	360	342	-5.0%

4.6.8 Barge Bow Impact Location: Underside of Rake Versus Headlog

All simulations discussed previously were conducted under the assumption that the waterline elevation coincides with the top-of-wall elevation (recall Figure 2.15). Consequently, in both empty (2-ft draft) and fully loaded (5-ft draft) configurations, impact occurs on the underside of the raked portion of the barge bow. However, conceivable impact conditions exist in which initial bow impact would occur with the headlog corner, rather than the rake—e.g. if mean water level is far below the top-of-wall elevation, or if the barge impacts while in a wave trough. Therefore, four additional simulations were conducted involving headlog impact with the HPO wall. Note that headlog impact was not considered with the PRO wall because the wall is too short to realistically accommodate this vertical barge placement. Impact force histories associated with headlog impacts are compared to corresponding rake impacts in Figures 4.67 – 4.70.

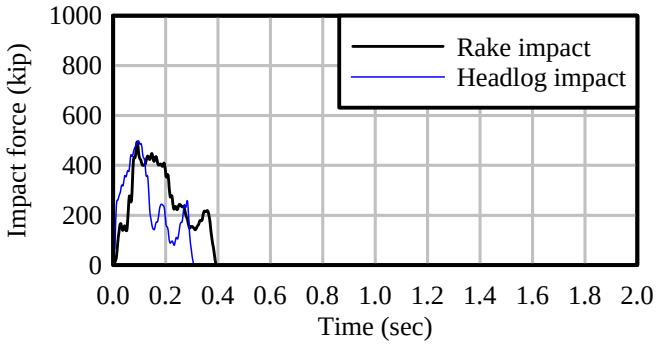

Figure 4.67 Force-history comparison: Empty barge, bow impact, HPO wall, 15° angle

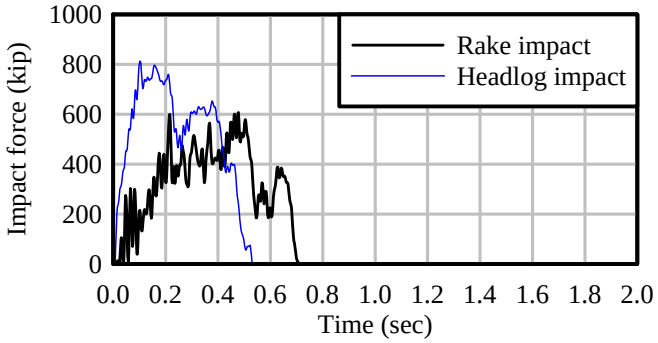

Figure 4.68 Force-history comparison: Empty barge, bow impact, HPO wall, 60° angle

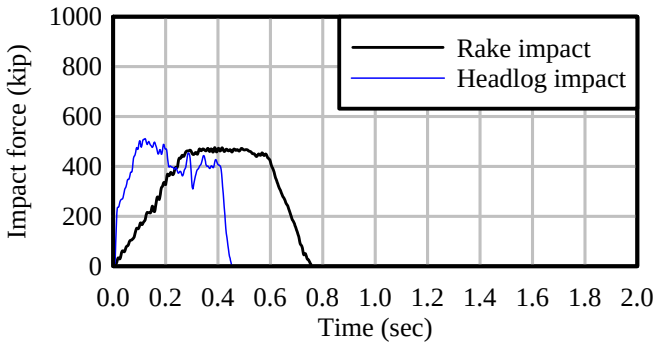

Figure 4.69 Force-history comparison: Loaded barge, bow impact, HPO wall, 15° angle

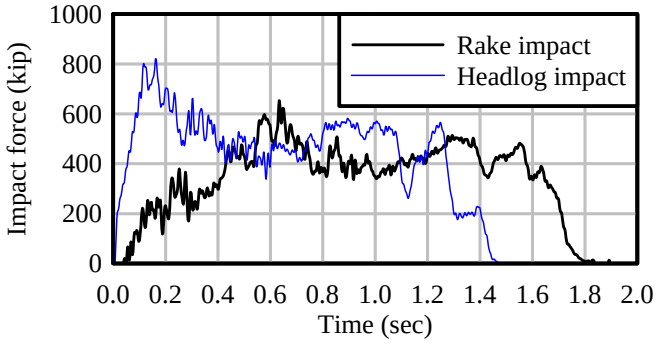

Figure 4.70 Force-history comparison: Loaded barge, bow impact, HPO wall, 60° angle

Maximum forces for the headlog impact simulations are summarized and compared to those obtained from rake impact scenarios in Table 4.12. No significant differences in maximum impact force were observed for the 15° cases. However, maximum forces generated by 60° headlog impacts were 30 – 50% higher than rake impact forces. Furthermore, for all cases considered, headlog impact durations were notably shorter. These findings suggest that the barge headlog is both stiffer and stronger (higher yield load) than the underside of the rake. Given the

increase in forces associated with headlog impact, substantial design advantage could be gained by minimizing the likelihood of this impact scenario.

Table 4.12 Maximum forces for impact with barge rake and headlog

Impact condition	Impact angle (°)	Barge weight	Impacted wall structure	Max. force rake impact (kip)	Max. force headlog impact (kip)	Percent difference
Barge bow	15	Empty (362 tons)	HPO	410	395	-3.65%
Barge bow	60	Empty (362 tons)	HPO	499	738	47.9%
Barge bow	15	Loaded (1645 tons)	HPO	466	475	1.93%
Barge bow	60	Loaded (1645 tons)	HPO	545	707	29.7%

CHAPTER 5
CONCLUSIONS AND RECOMMENDATIONS

Errant barge vessels pose a serious risk to hurricane protection structures during a hurricane event. As documented in this study, significant impact forces are manifested when hurricane winds and associated waves propel a barge into walls or fronting protection systems. The aim of the current study was to quantify dynamic impact forces associated with specified impact conditions on two hurricane protection walls and one fronting protection system—namely, the HPO wall, PRO wall, and PRO dolphin. Dynamic force-histories were developed using high-resolution finite element impact simulations between a jumbo hopper barge and the three structures of interest.

Eight baseline impact conditions were considered for each of the three structures. Each baseline simulation involved impact with varying impact angles, at 5 knots transverse to the wall (or line of dolphins) and 1 knot longitudinally. Force-histories were obtained from each simulation and further processed, using a Gaussian kernel smoothing technique.

After smoothing each force-history, maximum forces were quantified that disregard high frequency force oscillations not likely to influence static structural response. Maximum forces for perfectly side-on or nearly side-on impact conditions (0° and 1°), were generally larger than those produced during oblique impacts (15° or more). Insufficient information is currently available to quantify the probability of occurrence of 0° to 1° impacts; however, such probability is likely small. Furthermore, significant barge slowing has been observed (in a separate, parallel study) in side-on impact scenarios, due to a hydrodynamic cushioning effect. If this effect is significant, forces predicted by baseline simulations for 0° to 1° may be overly conservative. Thus, if small-angle impacts are deemed unimportant, maximum forces are approximately 500 kips for the HPO wall, 530 kips for the PRO wall, and 400 kips for the PRO dolphin. However, if 0° to 1° impacts are deemed to be of concern, maximum impact forces (per monolith or dolphin) are approximately 1440 kips for the HPO wall, 720 kips for the PRO wall, and 435 kips for the PRO dolphin.

Simulations were also conducted with a fully loaded barge impacting the HPO wall and PRO dolphin. Maximum impact forces from fully loaded simulations were shown to increase dramatically relative to empty barge simulations, especially for stern impacts with the HPO wall. In addition, significantly larger impact forces were observed when impact occurs with the barge bow headlog (as opposed to the underside of the rake). Thus, if hurricane protection structures are to be designed to resist impacts from fully loaded barges or to resist headlog impact scenarios, it may be prudent to increase design impact loads as indicated in this report.

It is important to note that forces documented in this report can only be considered to be statically appropriate loads if dynamic effects, such as inertia-driven sway of the monolith or dolphin cap, do not greatly affect structural demands. No direct assertions can be made regarding the relative importance dynamic amplification phenomena based on the results of this study.

In addition to baseline simulations, approximately 30 additional simulations were conducted to assess the sensitivity of maximum impact loads to various model parameters (e.g., soil resistance, barge impact energy, pile connectivity). Maximum impact forces were generally found to be insensitive to even drastic variation of model parameters. The only parameters that significantly influenced impact forces were initial barge kinetic energy and initial momentum. Impact forces for bow impacts were found to increase along with impact energy and momentum, but ultimately plateau at approximately 550 kips. However, a fully loaded barge impacting

stern-first at 60° was found to generate a maximum force of approximately 750 kips, and an *empty* barge impacting with the bow headlog at 60° generated a force of approximately 740 kips. Therefore, selecting statically appropriate design loads ultimately depends on the choice of impact conditions that hurricane protection systems are desired to resist.

REFERENCES

American Association of State Highway and Transportation Officials (AASHTO), *Guide Specification and Commentary for Vessel Collision Design of Highway Bridges, 2nd Ed*., AASHTO, Washington D.C., 2009.

Consolazio, G.R., Cook, R.A., and Lehr, G.B., *Barge Impact Testing of the St. George Island Causeway Bridge Phase I: Feasibility Study*. Structures Research Report No. 783, Engineering and Industrial Experiment Station, University of Florida, Gainesville, Florida, 2002.

Consolazio, G.R., and Cowan, D.R., "Numerically Efficient Dynamic Analysis of Barge Collisions with Bridges Piers", *ASCE Journal of Structural Engineering*, 131(8):1256-66, 2005.

Consolazio, G.R., Cook, R.A., McVay, M.C., Cowan, D.R., Biggs, A.E., and Bui, L., *Barge Impact Testing of the St. George Island Causeway Bridge*, University of Florida Engineering and Industrial Experiment Station, University of Florida, Gainesville, Florida, Structures Research Report No. 26868, 2006.

Consolazio, G.R., Davidson, M.T., and Cowan, D.R. "Barge Bow Force-Deformation Relationships for Barge-Bridge Collision Analysis", *Journal of the Transportation Research Board*, 2131:3-14, 2009.

Consolazio, G.R., Davidson, M.T., and Getter, D.J., "Dynamic Amplification of Pier Column Internal Forces Due to Barge-Bridge Collision", *Journal of the Transportation Research Board*, 2172:11-22, 2010.

European Committee for Standardization (CEN). *Eurocode 1: Actions on Structures – Part 1-7: General Actions – Accidental Actions (EN 1991-1-7:2007-02)*, CEN, Brussels, 2007.

FB-Deep, *FB-Deep User's Manual*. Florida Bridge Software Institute, University of Florida, Gainesville, Florida, 2009.

FB-MultiPier, *FB-MultiPier User's Manual*. Florida Bridge Software Institute, University of Florida, Gainesville, Florida, 2009.

Getter, D.J., and Consolazio, G.R., "Relationships of Barge Bow Force-Deformation for Bridge Design: Probabilistic Consideration of Oblique Impact Scenarios", *Journal of The Transportation Research Board*, 2251:3-15, 2011.

Getter, D.J., Consolazio, G.R., and Davidson, M.T., "Equivalent Static Analysis Method for Barge Impact-Resistant Bridge Design", *ASCE Journal of Bridge Engineering*, 16(6):718-27, 2011.

LS-DYNA, *LS-DYNA Keyword User's Manual: Version 971*, Livermore Software Technology Corporation, Livermore, CA, 2009.

McVay, M. C., Wasman, S.J., and Bullock, P.J., *St. George Geotechnical Investigation of Vessel Pier Impact*, Engineering and Industrial Experiment Station, University of Florida, Gainesville, Florida, 2005.

Patev, R.C., Barker, B.C., and Koestler, L.V., *Prototype Barge Impact Experiments, Allegheny Lock and Dam 2, Pittsburgh, Pennsylvania*, U.S. Army Corps of Engineers (USACE) Report, Washington D.C., 2003a.

Patev, R.C., Barker, B.C., and Koestler, L.V., *Full-Scale Barge Impact Experiments, Robert C. Byrd Lock and Damn, Gallipolis Ferry, West Virginia*, U.S. Army Corps of Engineers (USACE) Report, Washington D.C., 2003b.

Tomlinson, M.J., *Pile Design and Construction*, Taylor & Francis, Abingdon, UK, 1994.

U.S. Army Corps of Engineers (USACE), *ETL-1110-2-563: Engineering and Design, Barge Impact Analysis for Rigid Walls*, USACE, Washington D.C., 2004.

Yuan, P., Harik, I.E., and Davidson M.T., *Multi-Barge Flotilla Impact Forces on Bridges*, Kentucky Transportation Center Report KTC-08-13/SPR261-03-2F, University of Kentucky, Lexington, 2008.

APPENDIX A
HPO WALL PARALLEL (TO MONOLITH) AND VERTICAL LOAD-HISTORIES

Presented in Appendix A are the global (x, y, and z) force-histories obtained from eight baseline LS-DYNA collision simulations conducted between a jumbo hopper barge and a Hurricane Protection Office (HPO) wall. For each case, a schematic is included where impact angles, impact velocities, global coordinate systems, and the engaged monolith(s) are denoted. Furthermore, the orientation of the barge relative to the HPO wall is illustrated for each case. A summary of pertinent parameters for each analysis case is given in Table A.1.

Table A.1 Impact cases for HPO wall

Impact condition	Impact angle (°)	Barge weight	Barge draft (ft)	Initial X-velocity (knot)	Initial Y-velocity (knot)
Barge side	0	Empty (362 tons)	2	5	1
Barge bow	1	Empty (362 tons)	2	5	1
Barge bow	15	Empty (362 tons)	2	5	1
Barge bow	30	Empty (362 tons)	2	5	1
Barge bow	45	Empty (362 tons)	2	5	1
Barge bow	60	Empty (362 tons)	2	5	1
Barge stern	15	Empty (362 tons)	2	5	1
Barge stern	60	Empty (362 tons)	2	5	1

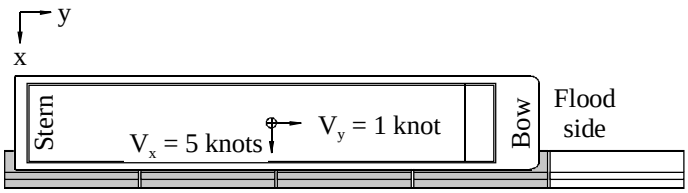

a)

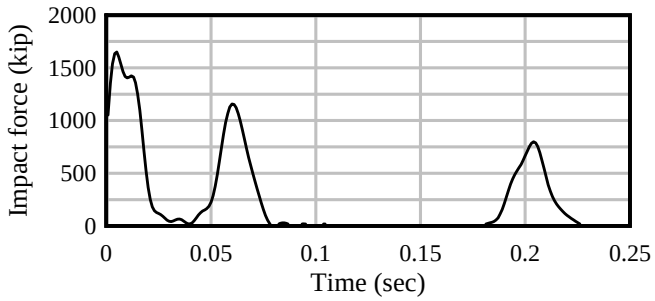

b)

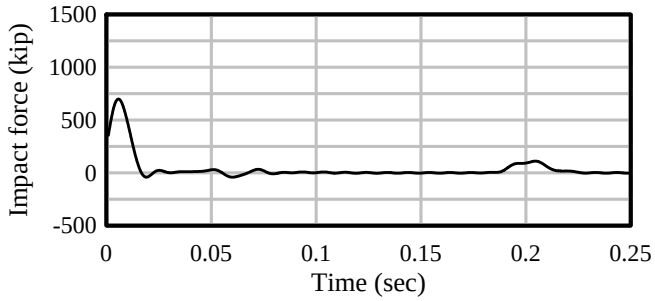

c)

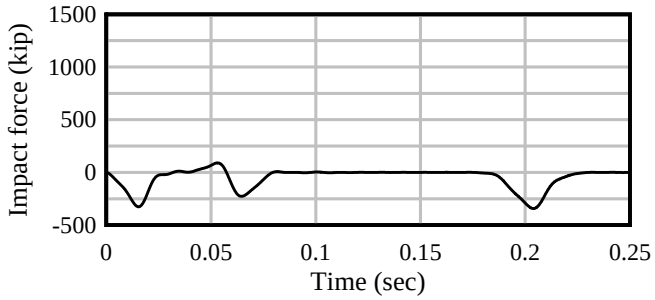

d)

Figure A.1 Empty barge, sidewall impact, HPO wall, 0° angle impact force-histories: a) Schematic; b) X-direction; c) Y-direction; d) Z-direction

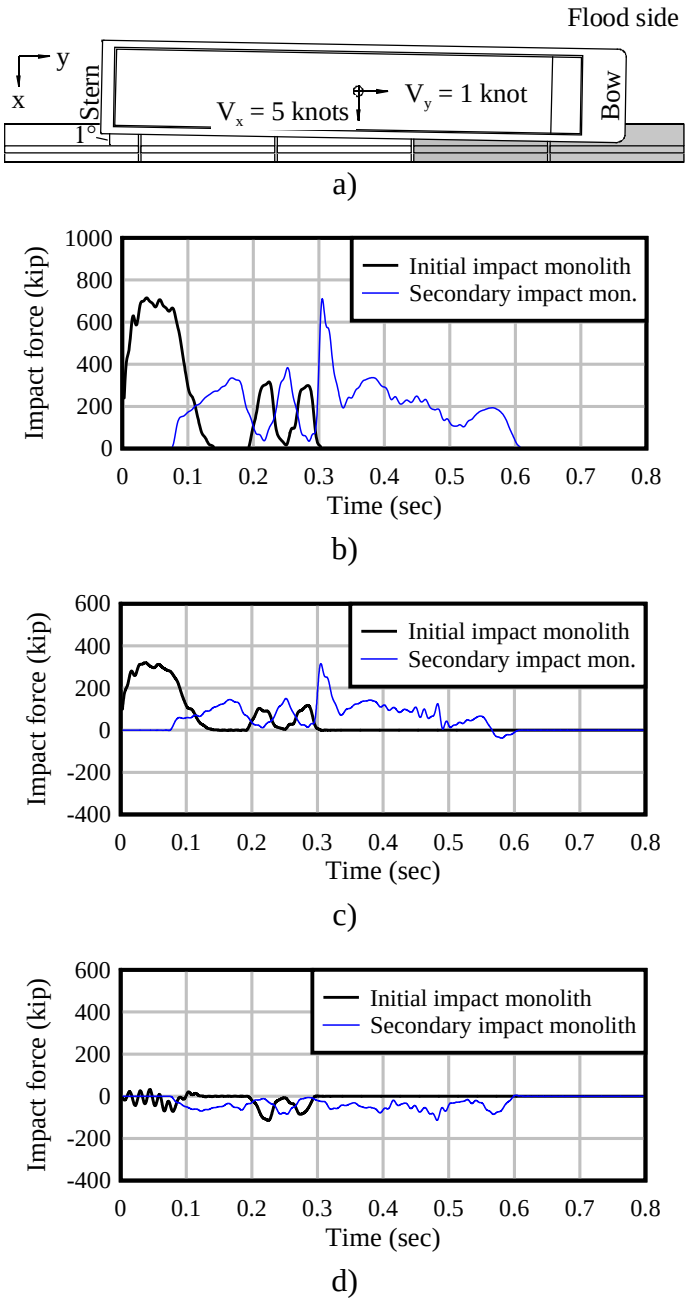

Figure A.2 Empty barge, bow impact, HPO wall, 1° angle impact force-histories: a) Schematic; b) X-direction; c) Y-direction; d) Z-direction

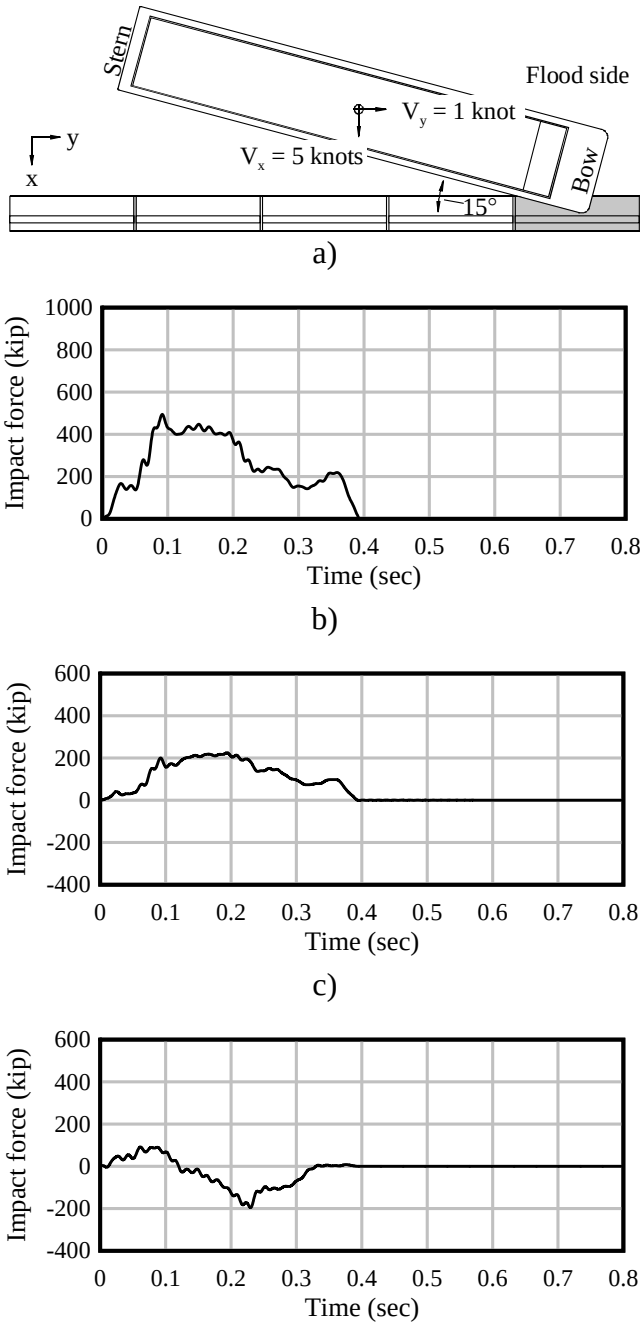

Figure A.3 Empty barge, bow impact, HPO wall, 15° angle impact force-histories: a) Schematic; b) X-direction; c) Y-direction; d) Z-direction

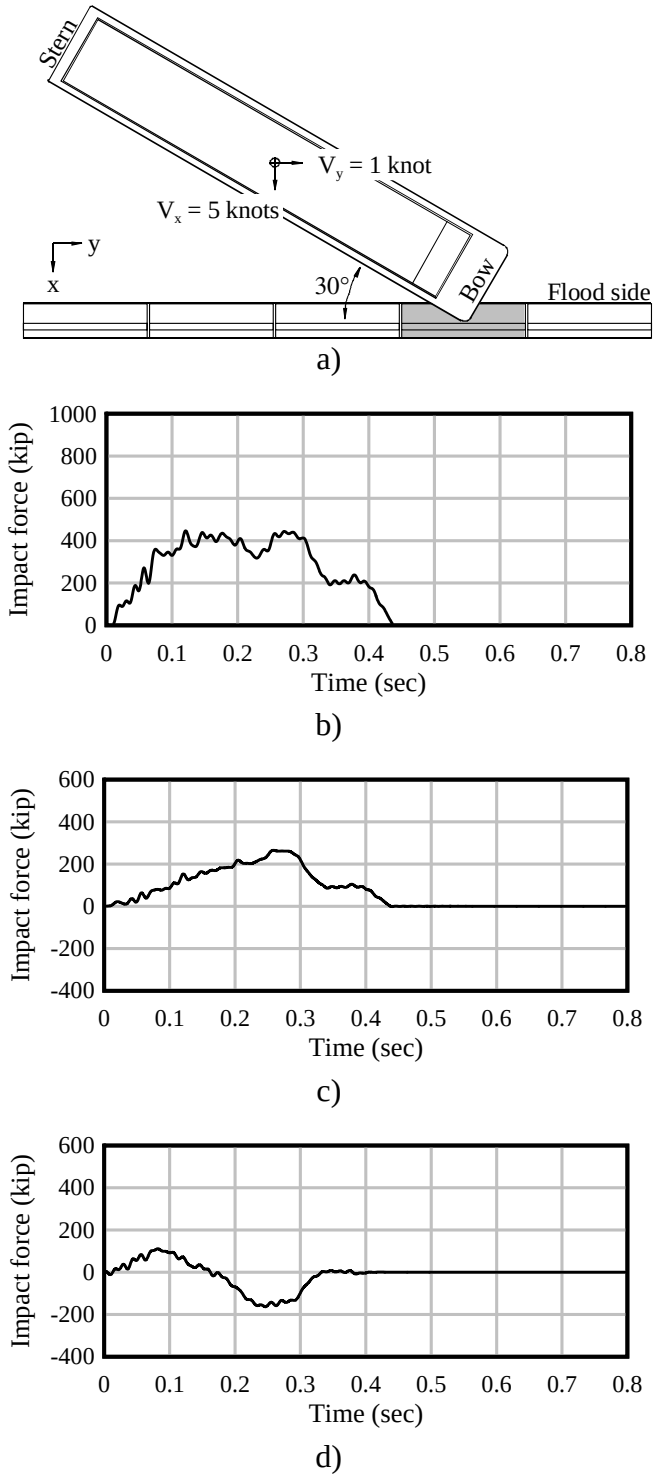

Figure A.4 Empty barge, bow impact, HPO wall, 30° angle impact force-histories: a) Schematic; b) X-direction; c) Y-direction; d) Z-direction

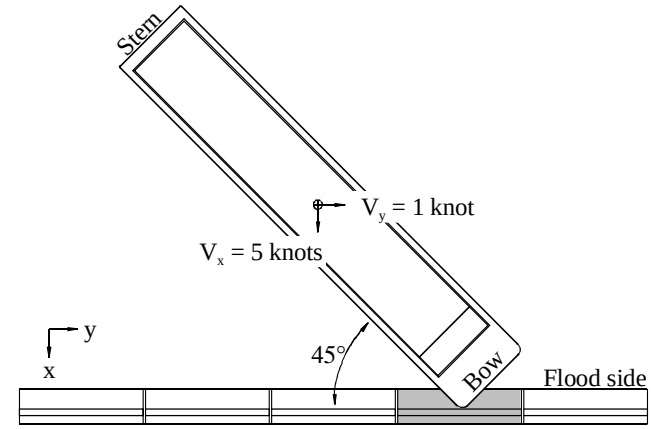

a)

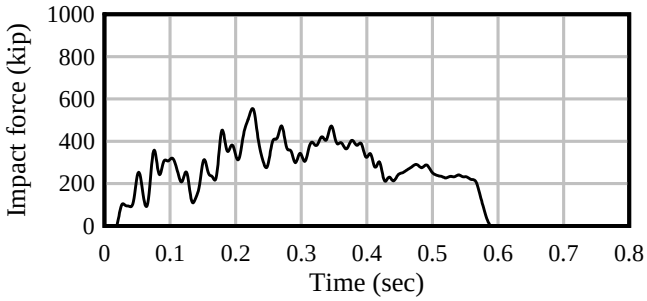

b)

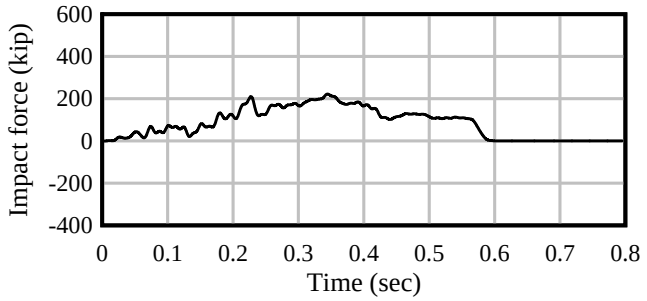

c)

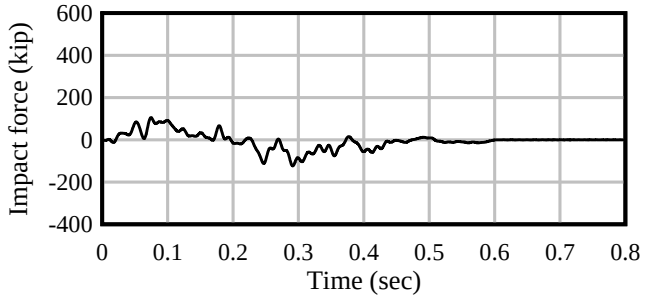

d)

Figure A.5 Empty barge, bow impact, HPO wall, 45° angle impact force-histories: a) Schematic; b) X-direction; c) Y-direction; d) Z-direction

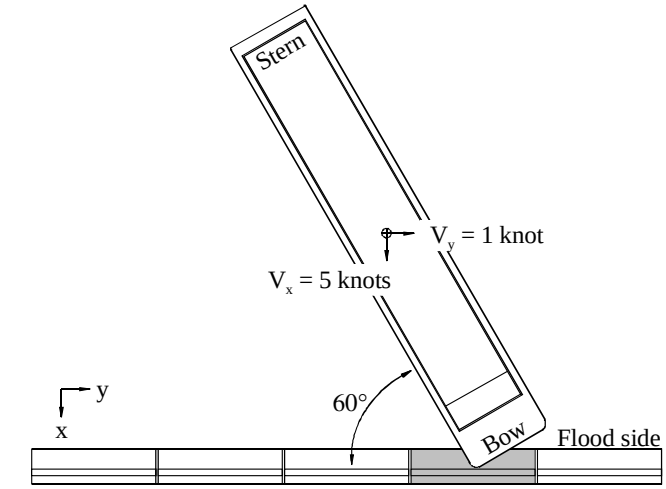

a)

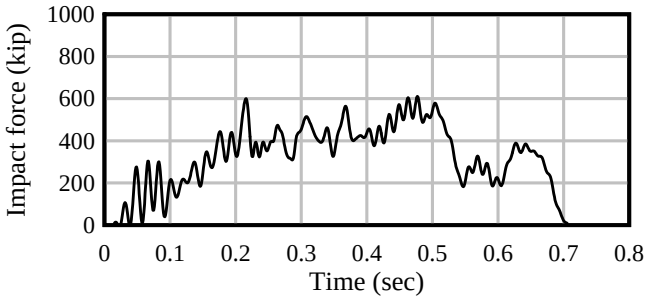

b)

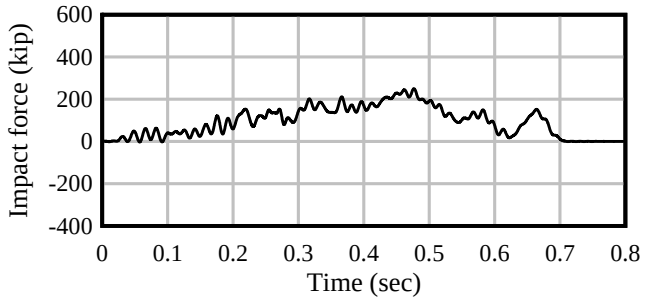

c)

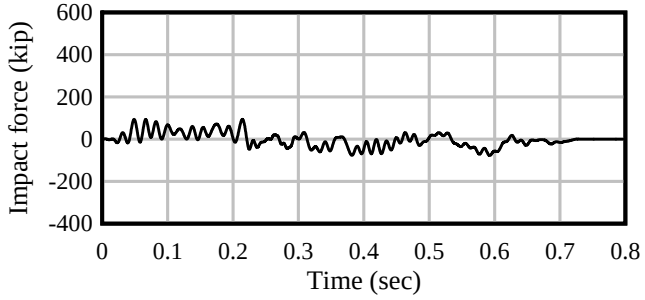

d)

Figure A.6 Empty barge, bow impact, HPO wall, 60° angle impact force-histories: a) Schematic; b) X-direction; c) Y-direction; d) Z-direction

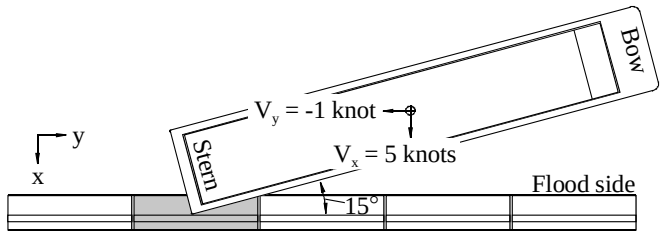

a)

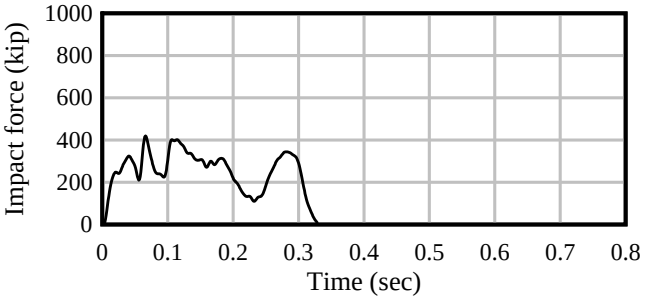

b)

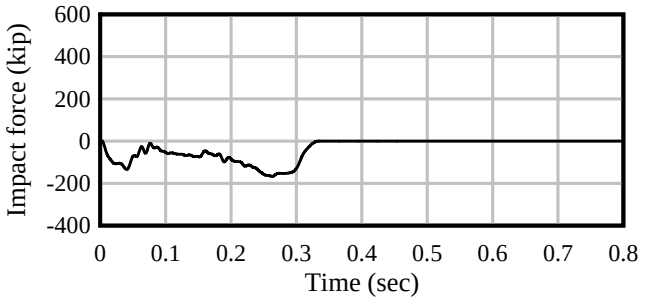

c)

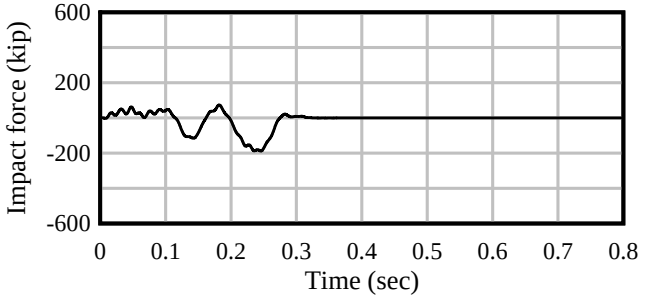

d)

Figure A.7 Empty barge, stern impact, HPO wall, 15° angle impact force-histories: a) Schematic; b) X-direction; c) Y-direction; d) Z-direction

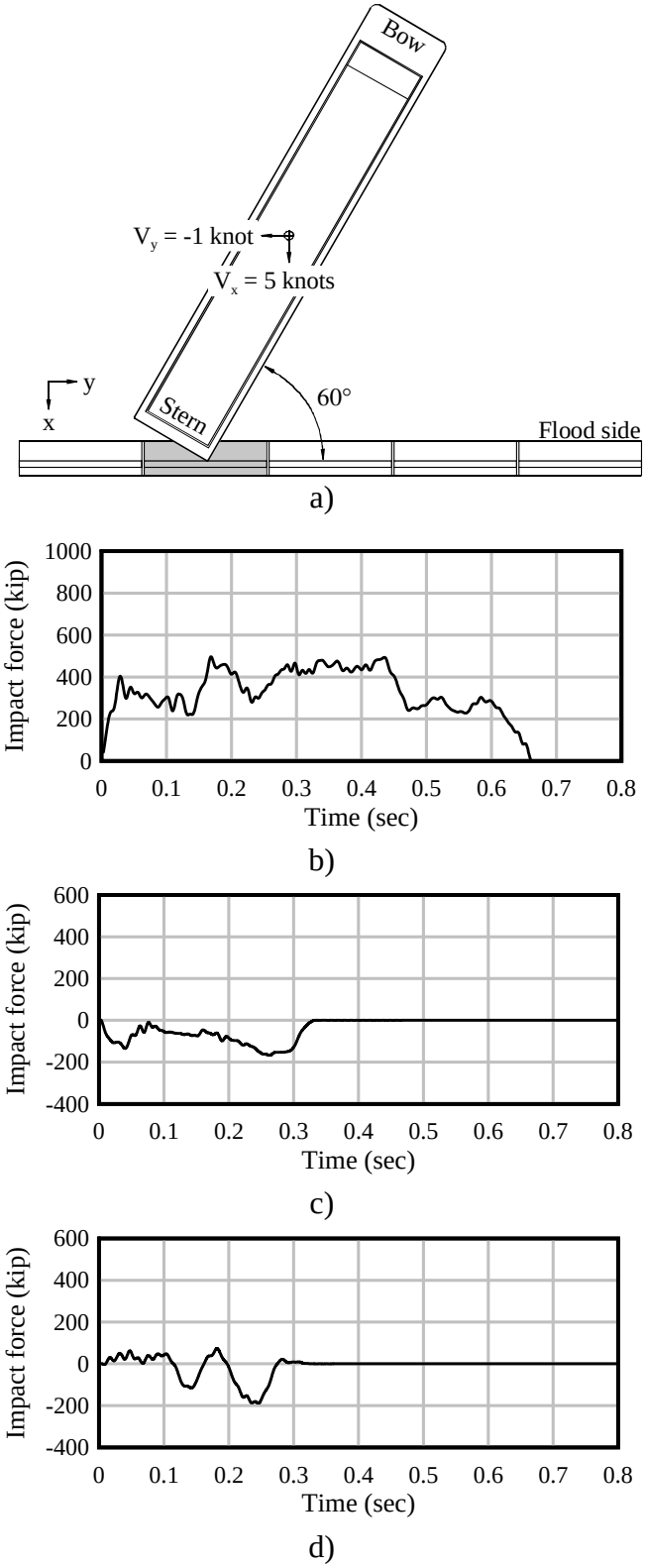

Figure A.8 Empty barge, stern impact, HPO wall, 60° angle impact force-histories: a) Schematic; b) X-direction; c) Y-direction; d) Z-direction

APPENDIX B
PRO WALL PARALLEL (TO MONOLITH) AND VERTICAL LOAD-HISTORIES

Presented in Appendix B are the global (x, y, and z) force-histories obtained from eight baseline LS-DYNA collision simulations conducted between a jumbo hopper barge and a Protection and Restoration Office (PRO) wall. For each case, a schematic is included where impact angles, impact velocities, global coordinate systems, and the engaged monolith(s) are denoted. Furthermore, the orientation of the barge relative to the PRO wall is illustrated for each case. A summary of pertinent parameters for each analysis case is given in Table B.1.

Table B.1 Impact cases for PRO wall

Impact condition	Impact angle (°)	Barge weight	Barge draft (ft)	Initial X-velocity (knot)	Initial Y-velocity (knot)
Barge side	0	Empty (362 tons)	2	5	1
Barge bow	1	Empty (362 tons)	2	5	1
Barge bow	15	Empty (362 tons)	2	5	1
Barge bow	30	Empty (362 tons)	2	5	1
Barge bow	45	Empty (362 tons)	2	5	1
Barge bow	60	Empty (362 tons)	2	5	1
Barge stern	15	Empty (362 tons)	2	5	1
Barge stern	60	Empty (362 tons)	2	5	1

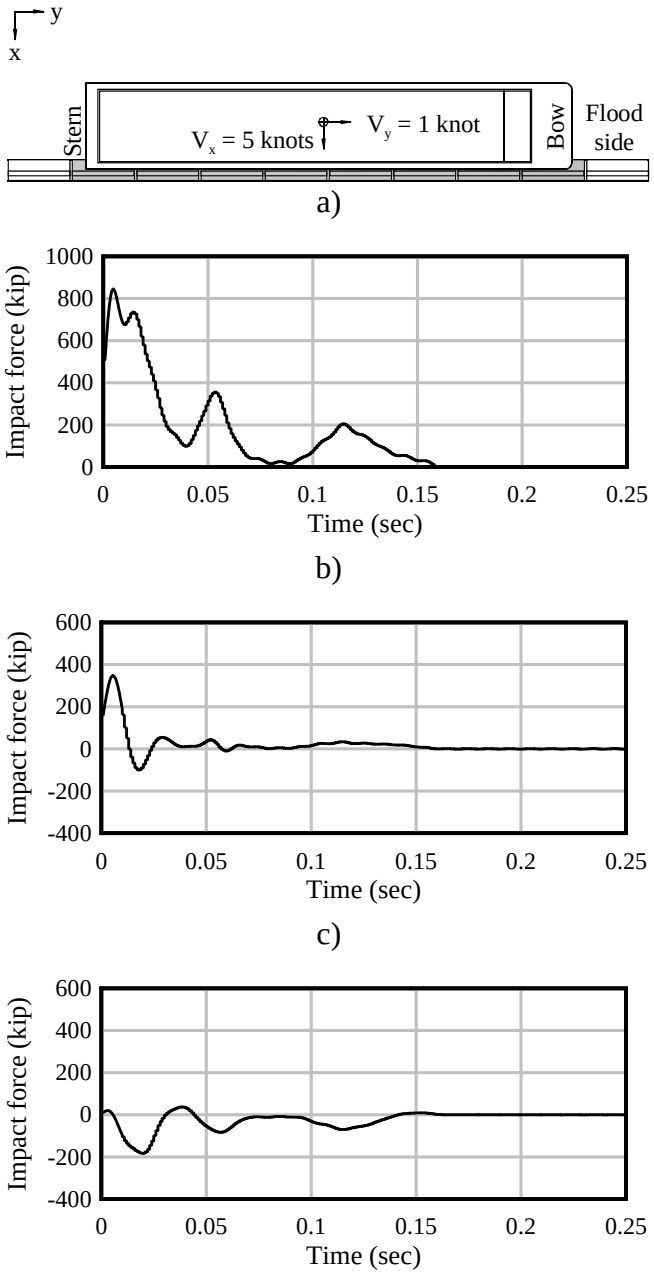

Figure B.1 Empty barge, sidewall impact, PRO wall, 0° angle, impact force-histories: a) Schematic; b) X-direction; c) Y-direction; d) Z-direction

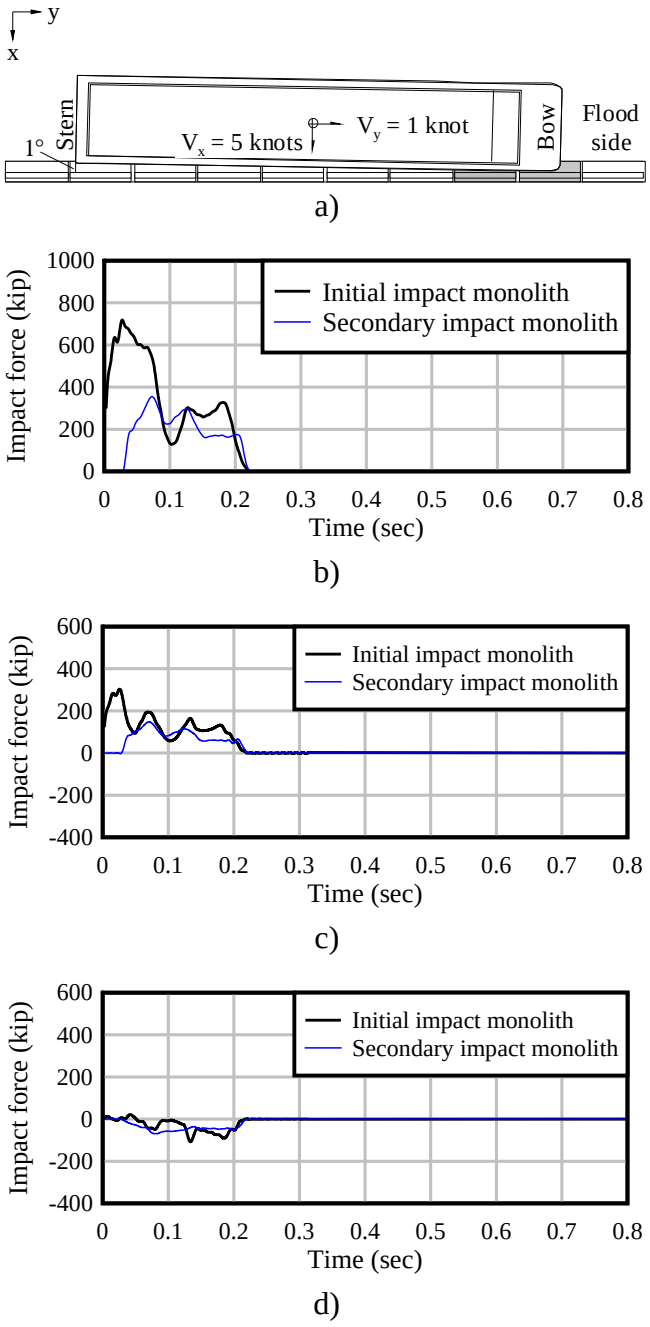

Figure B.2 Empty barge, bow impact, PRO wall, 1° angle, impact force-histories, initial impact monolith: a) Schematic; b) X-direction; c) Y-direction; d) Z-direction

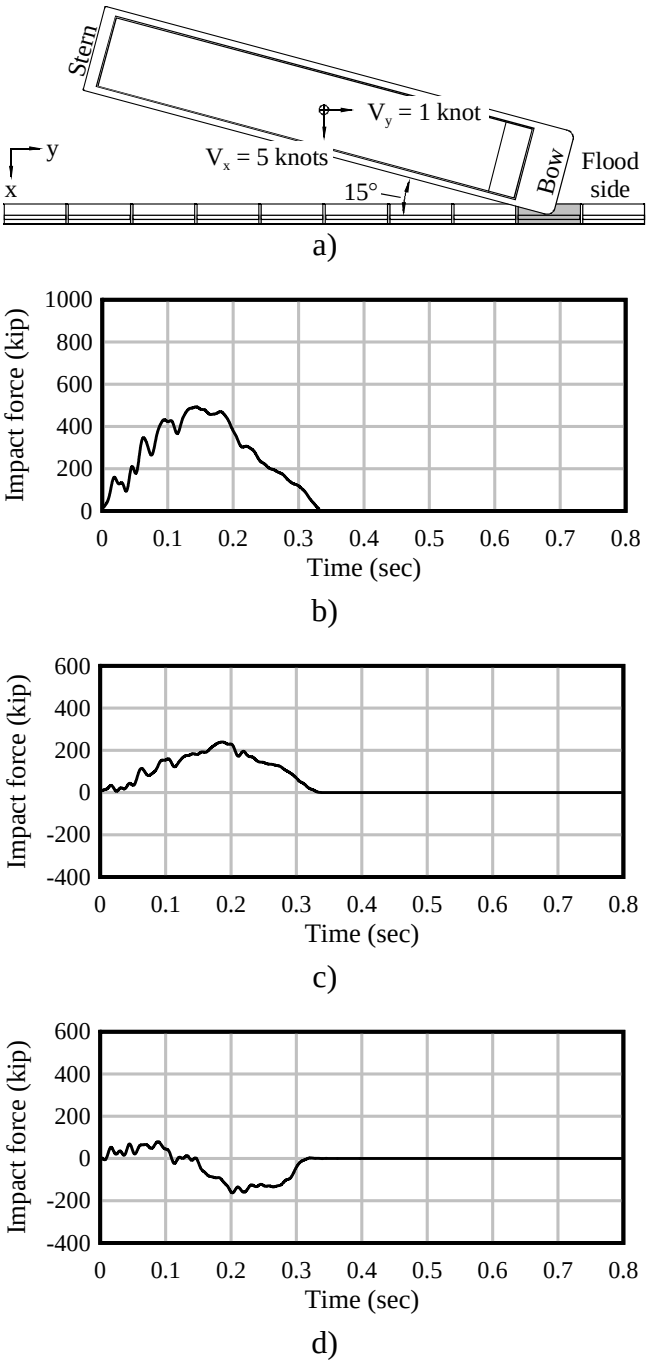

Figure B.3 Empty barge, bow impact, PRO wall, 15° angle impact force-histories: a) Schematic; b) X-direction; c) Y-direction; d) Z-direction

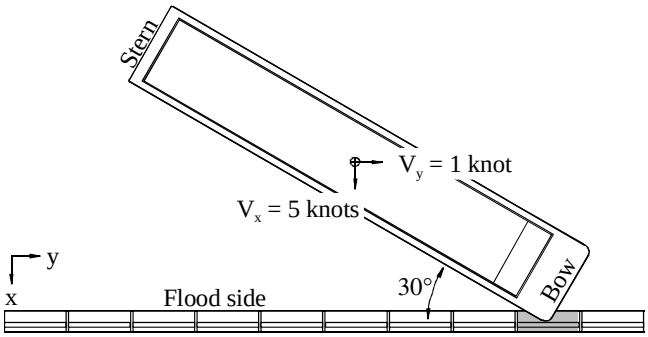

a)

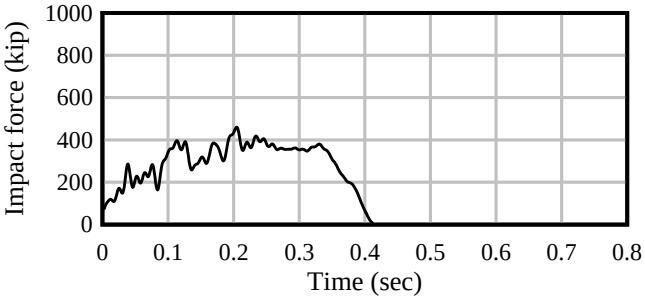

b)

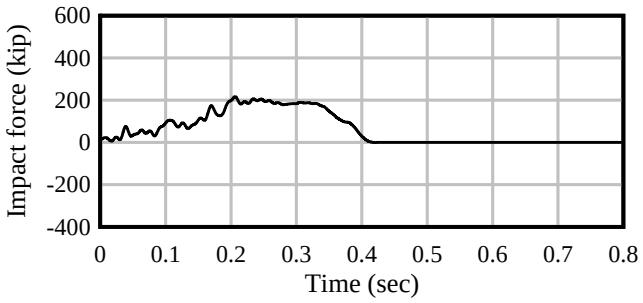

c)

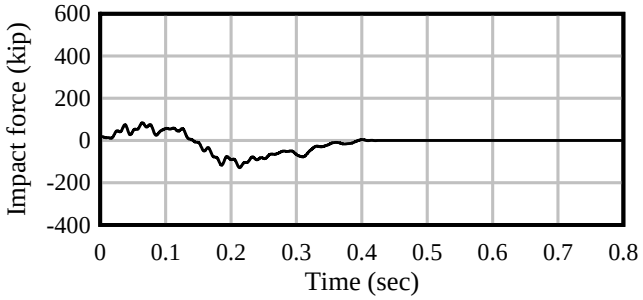

d)

Figure B.4 Empty barge, bow impact, PRO wall, 30° angle impact force-histories: a) Schematic; b) X-direction; c) Y-direction; d) Z-direction

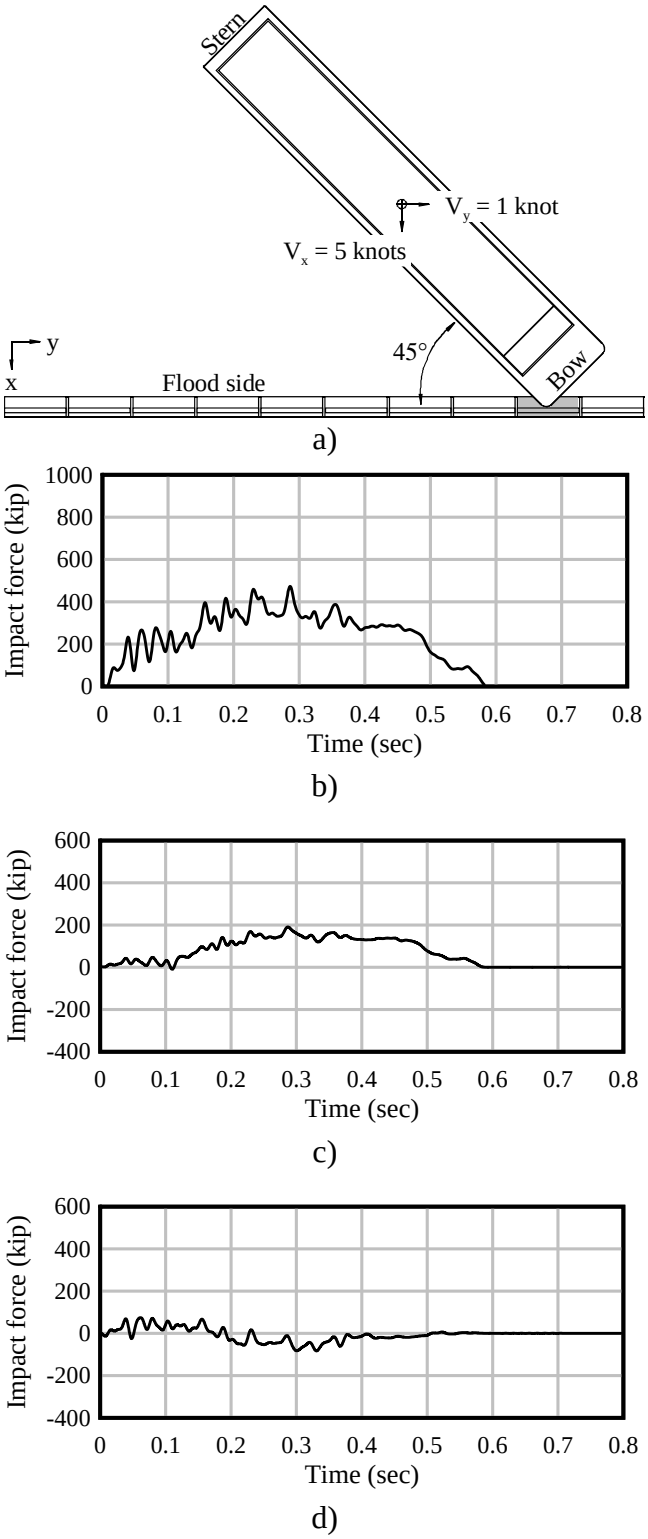

Figure B.5 Empty barge, bow impact, PRO wall, 45° angle impact force-histories: a) Schematic; b) X-direction; c) Y-direction; d) Z-direction

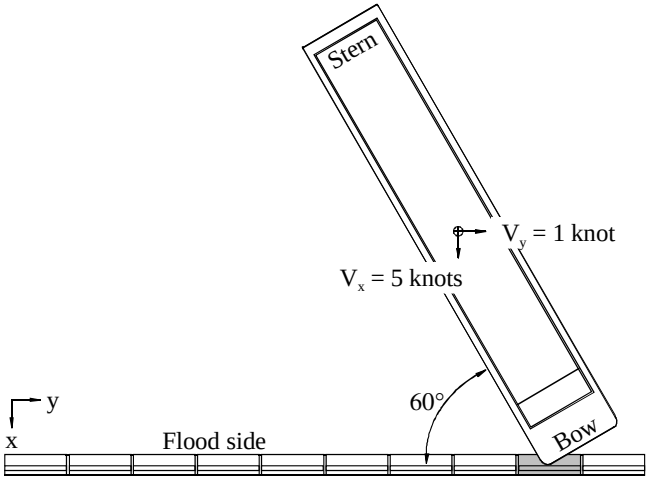

a)

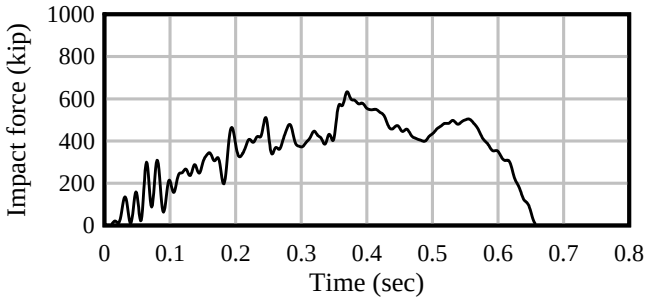

b)

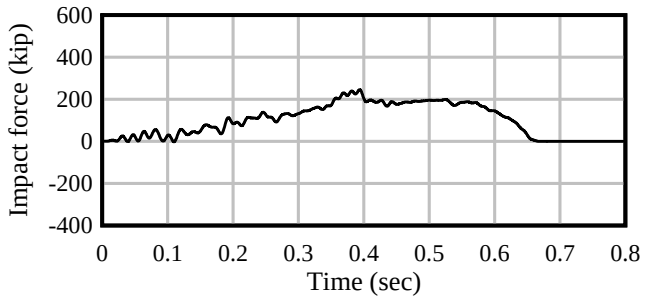

c)

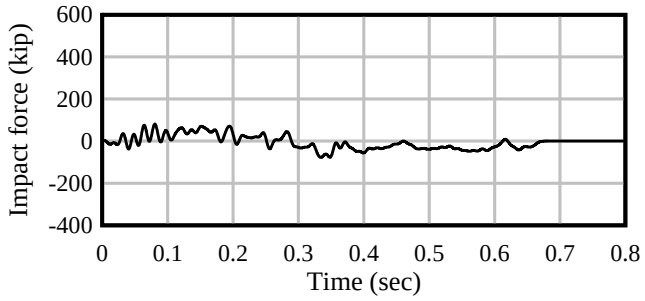

d)

Figure B.6 Empty barge, bow impact, PRO wall, 60° angle impact force-histories: a) Schematic; b) X-direction; c) Y-direction; d) Z-direction

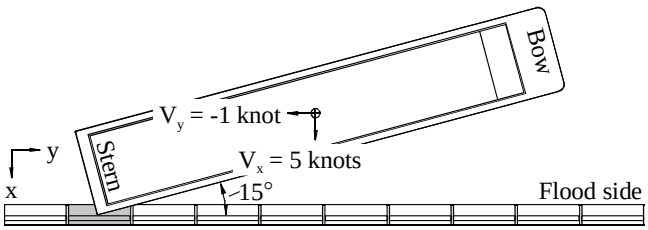

a)

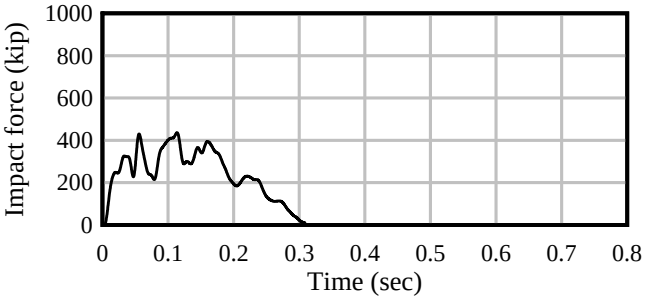

b)

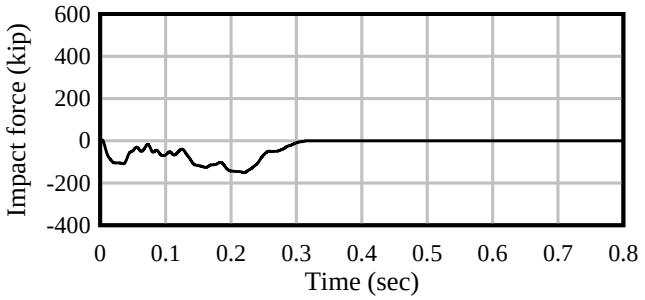

c)

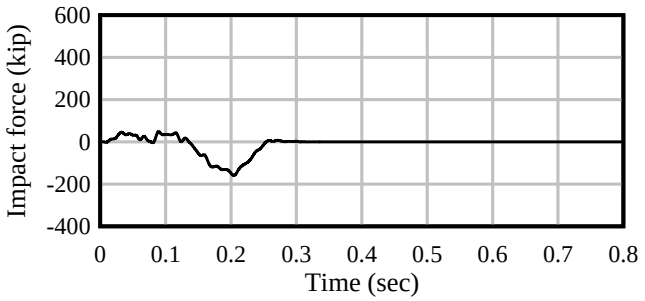

d)

Figure B.7 Empty barge, stern impact, PRO wall, 15° angle impact force-histories: a) Schematic; b) X-direction; c) Y-direction; d) Z-direction

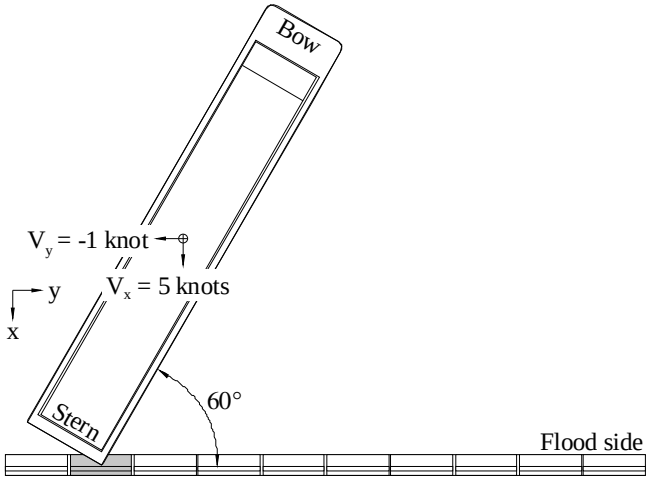

a)

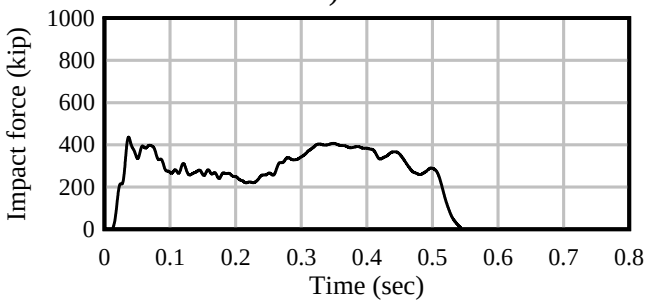

b)

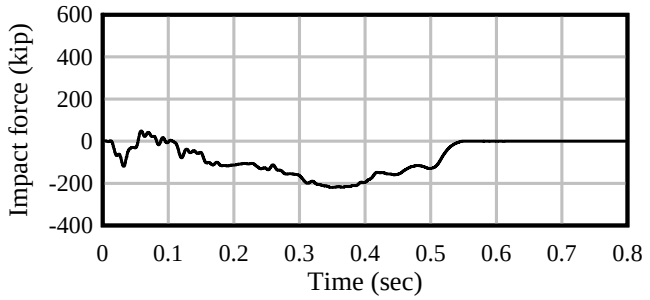

c)

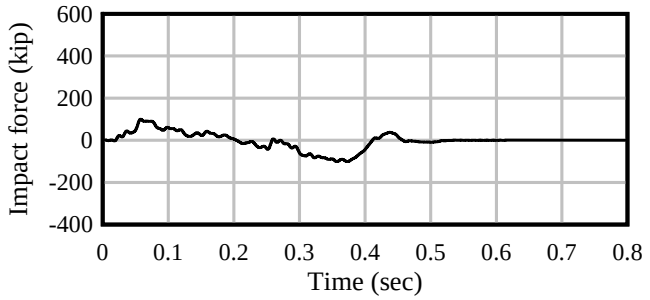

d)

Figure B.8 Empty barge, stern impact, PRO wall, 60° angle impact force-histories: a) Schematic; b) X-direction; c) Y-direction; d) Z-direction

APPENDIX C
PRO DOLPHIN PARALLEL (TO MONOLITH) AND VERTICAL LOAD-HISTORIES

Presented in Appendix C are the global (x, y, and z) force-histories obtained from eight baseline LS-DYNA collision simulations conducted between a jumbo hopper barge and Protection and Restoration Office (PRO) dolphin units. Since multiple PRO dolphin units are impacted during the simulations, the PRO dolphin unit with the greatest magnitude force is plotted with a solid black line. For example, in Figure C.1b, the greatest magnitude force is imparted to Dolphin 3, and hence, the force-history for dolphin 3 is plotted using a solid black line. For each case, a schematic is included where impact angles, impact velocities, and global coordinate systems are denoted. Furthermore, the orientation of the barge relative to the PRO dolphin is illustrated for each case. A summary of pertinent parameters for each analysis case is given in Table C.1.

Table C.1 Impact cases for PRO dolphin units

Impact condition	Impact angle (°)	Barge weight	Barge draft (ft)	Initial X-velocity (knot)	Initial Y-velocity (knot)
Barge side	0	Empty (362 tons)	2	5	1
Barge bow	1	Empty (362 tons)	2	5	1
Barge bow	15	Empty (362 tons)	2	5	1
Barge bow	30	Empty (362 tons)	2	5	1
Barge bow	45	Empty (362 tons)	2	5	1
Barge bow	60	Empty (362 tons)	2	5	1
Barge stern	15	Empty (362 tons)	2	5	1
Barge stern	60	Empty (362 tons)	2	5	1

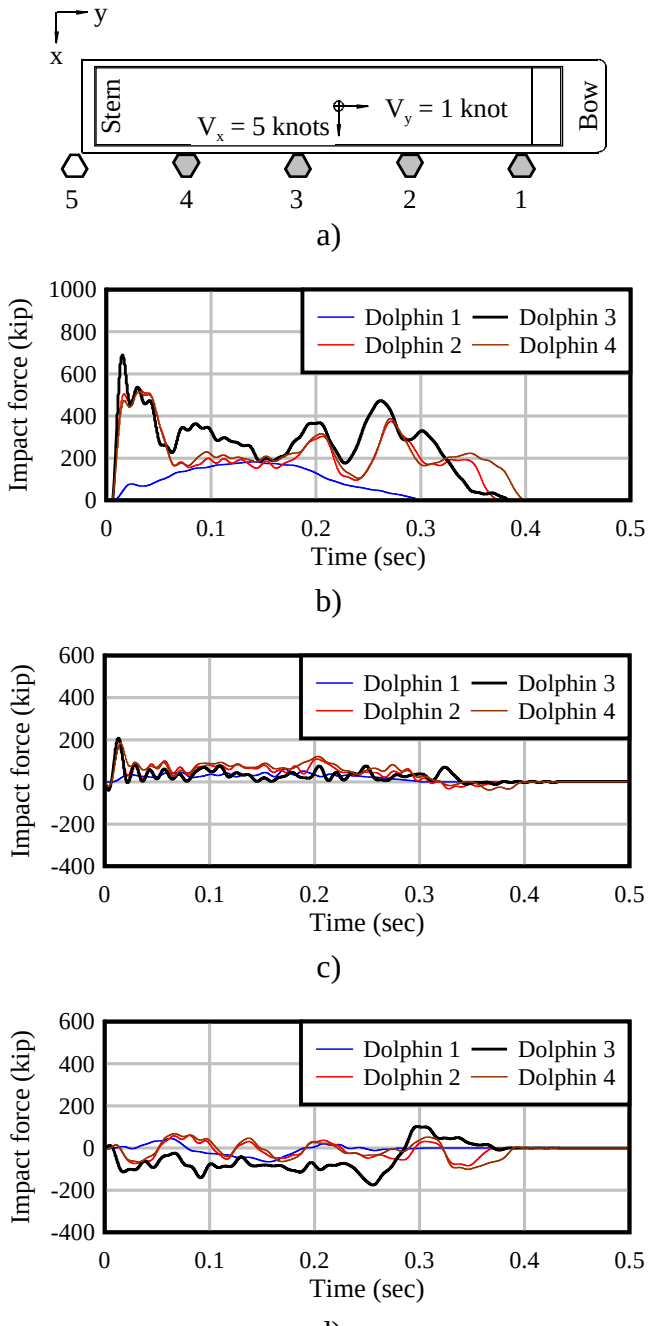

Figure C.1 Empty barge, bow impact, PRO dolphin, 0° angle impact force-histories: a) Schematic; b) X-direction; c) Y-direction; d) Z-direction

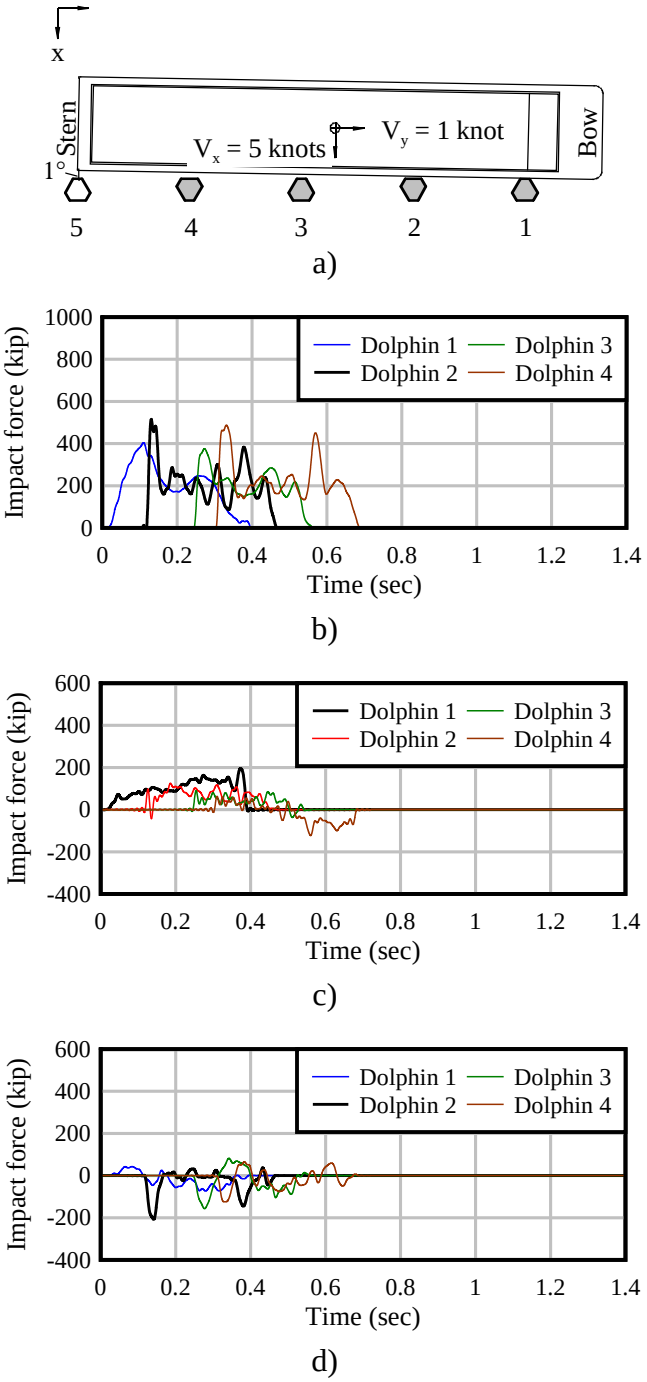

Figure C.2 Empty barge, bow impact, PRO dolphin, 1° angle impact force-histories: a) Schematic; b) X-direction; c) Y-direction; d) Z-direction

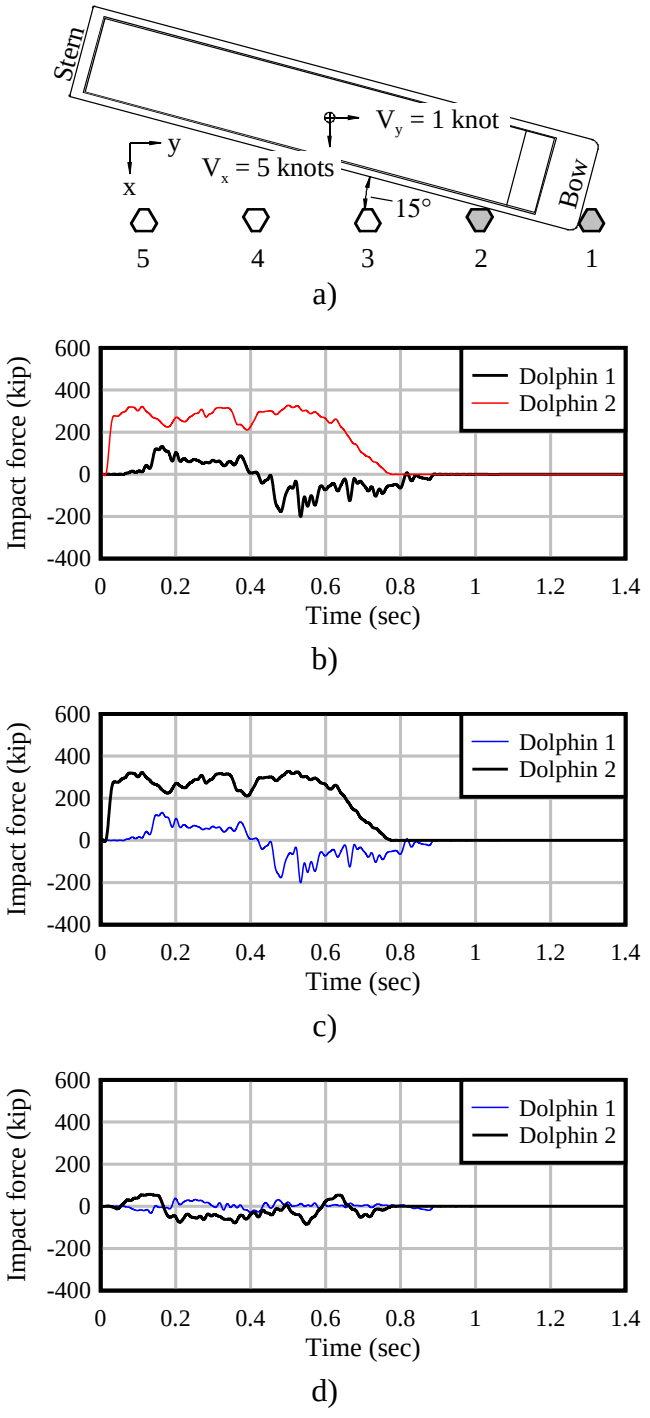

Figure C.3 Empty barge, bow impact, PRO dolphin, 15° angle impact force-histories: a) Schematic; b) X-direction; c) Y-direction; d) Z-direction

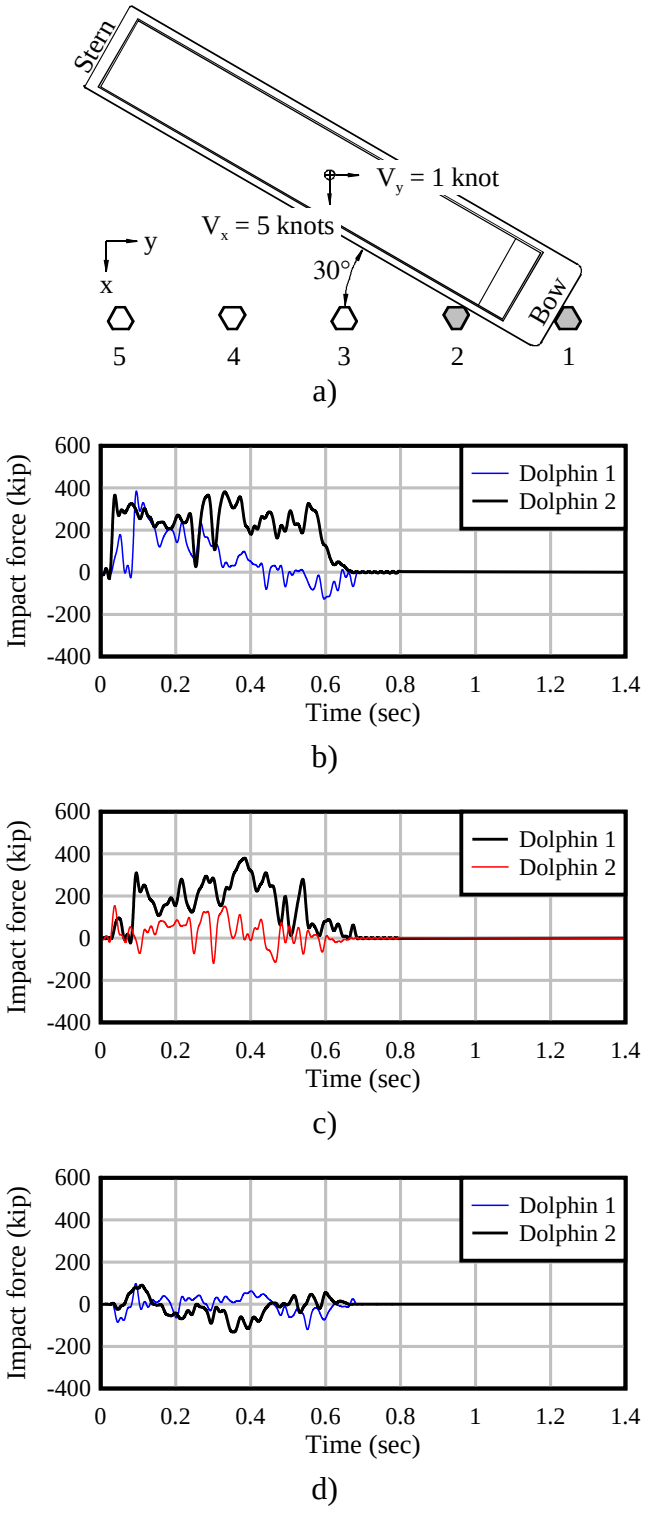

Figure C.4 Empty barge, bow impact, PRO dolphin, 30° angle impact force-histories: a) Schematic; b) X-direction; c) Y-direction; d) Z-direction

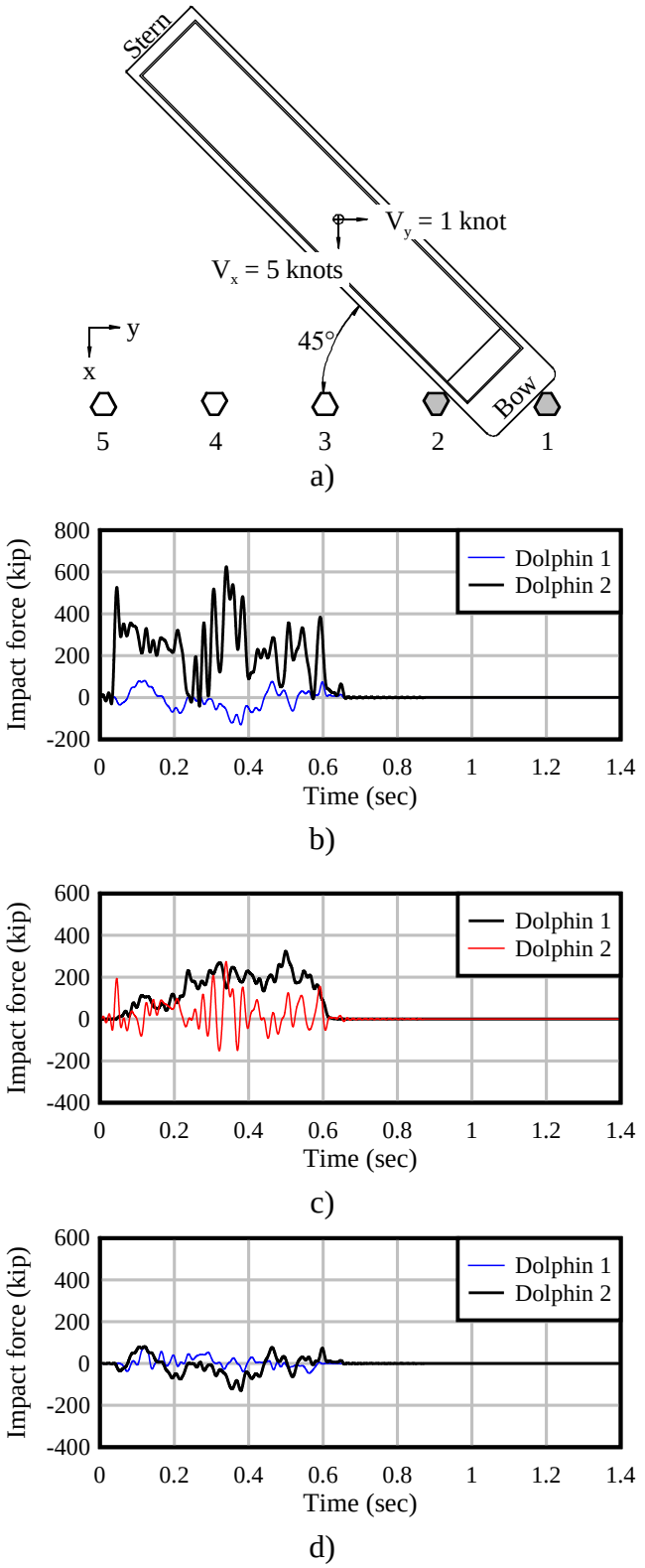

Figure C.5 Empty barge, bow impact, PRO dolphin, 45° angle impact force-histories: a) Schematic; b) X-direction; c) Y-direction; d) Z-direction

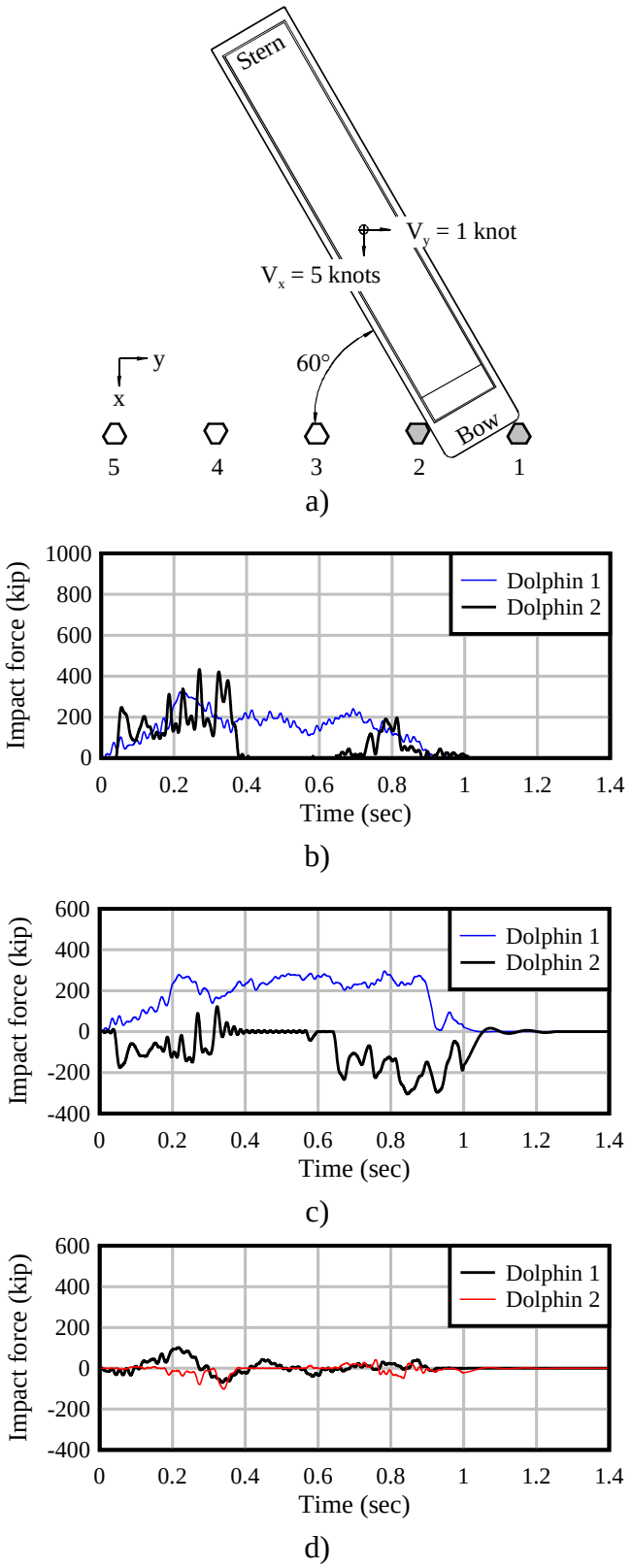

Figure C.6 Empty barge, bow impact, PRO dolphin, 60° angle impact force-histories: a) Schematic; b) X-direction; c) Y-direction; d) Z-direction

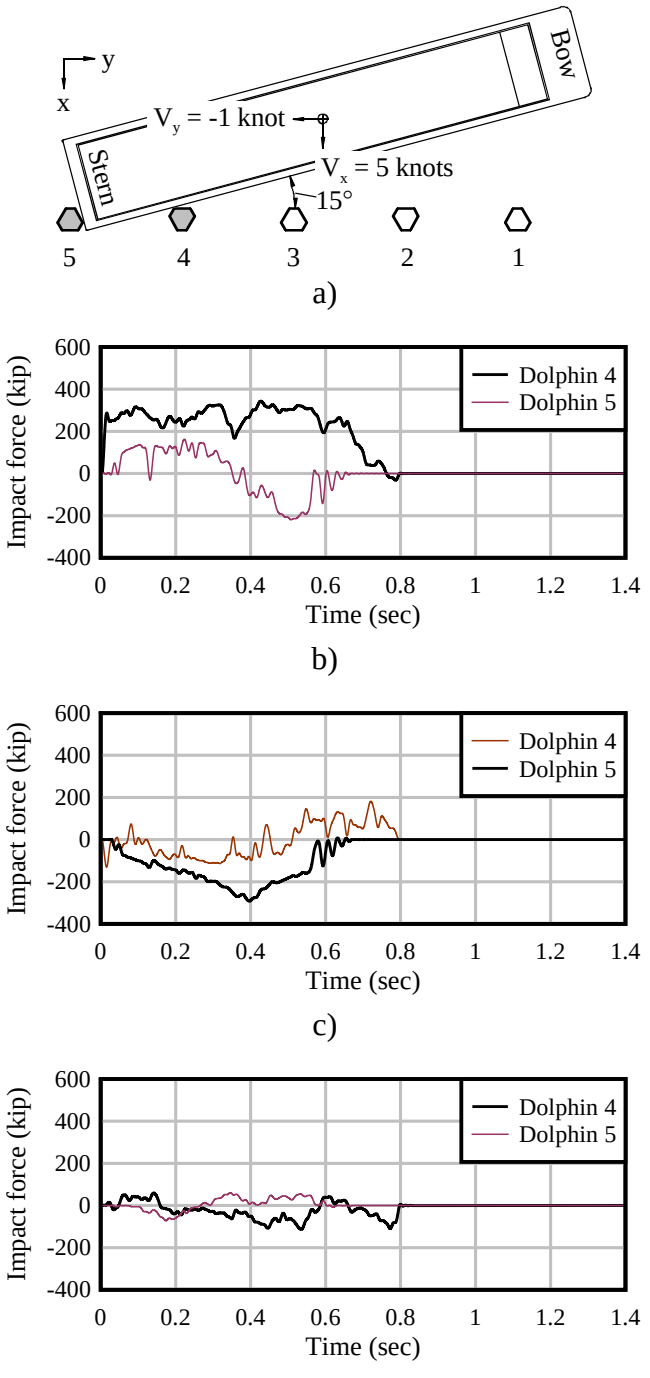

Figure C.7 Empty barge, stern impact, PRO dolphin, 15° angle impact force-histories: a) Schematic; b) X-direction; c) Y-direction; d) Z-direction

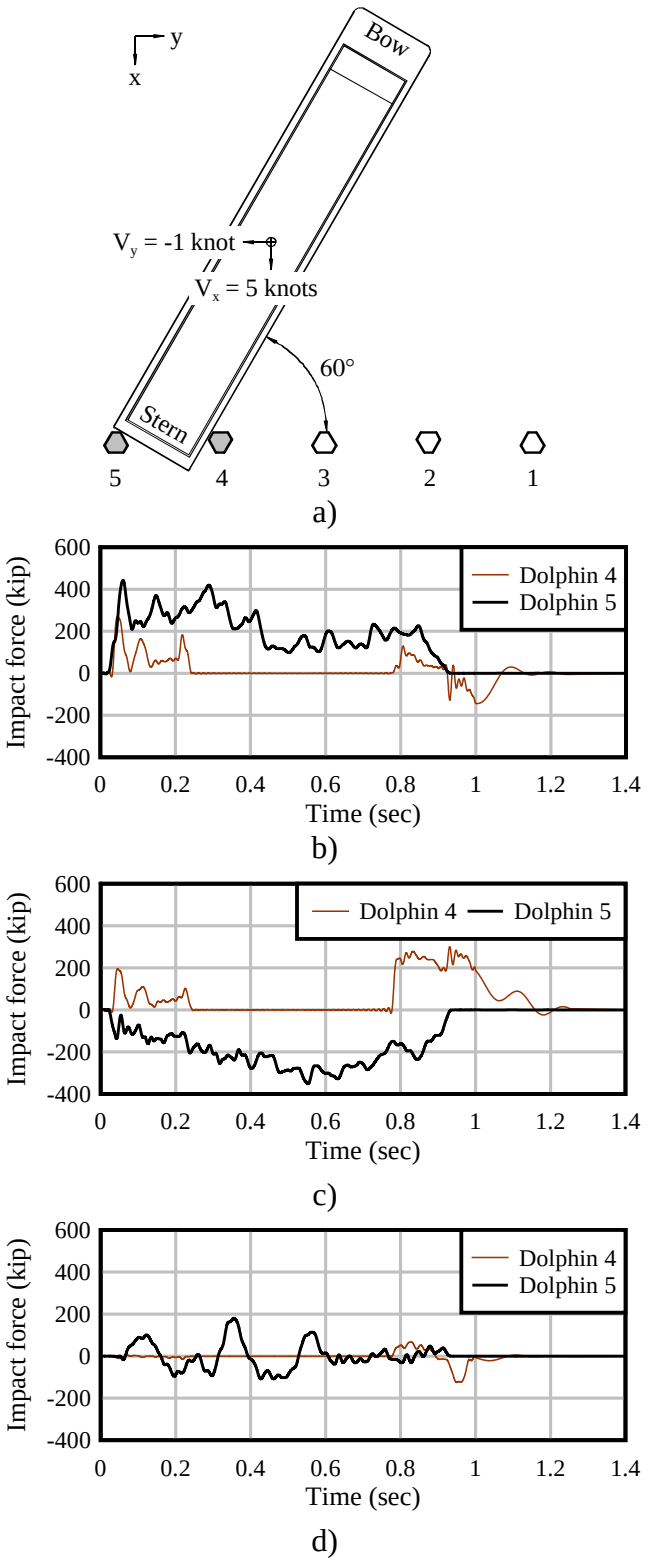

Figure C.8 Empty barge, stern impact, PRO dolphin, 60° angle impact force-histories: a) Schematic; b) X-direction; c) Y-direction; d) Z-direction